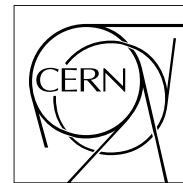


The Compact Muon Solenoid Experiment
Analysis Note

The content of this note is intended for CMS internal use and distribution only



23 July 2019 (v17, 23 June 2021)

Search for Neutral Long-lived Particles Decaying in the Muon System

Artur Apresyan, Matthew Citron, Daniel Diaz, Gabrielle Dituri, Javier Duarte, Zoltan Gecse, Gregor Kasieczka,
Cristian Pena, Joerg Schindler, James Sheplock, Nathan Suri, Maria Spiropulu, Christina Wang, Si Xie

Abstract

We search for neutral long-lived particles decaying in the Muon System with a signature of large multiplicity hits in the Cathode Strip Chambers. This search extends the current lifetime reach, achieving the best sensitivity for Higgs-mediated LLP production in beyond 100 m.

1 Contents

2	1	Introduction	3
3	2	Datasets	5
4	2.1	Data	5
5	2.2	Signal Simulations	5
6	2.3	Background simulation	8
7	3	Trigger	10
8	3.1	Trigger Efficiency Scale Factor	11
9	4	Object reconstruction and identification	13
10	4.1	CSC Rechit Clusters	13
11	4.2	Primary Vertex	16
12	4.3	Jets	16
13	4.4	Muons	17
14	4.5	Electrons	18
15	4.6	Missing Transverse Momentum	18
16	5	Event Selection	19
17	5.1	Cluster Selection	19
18	5.2	Cosmic Muon Shower Events	27
19	5.3	Signal Region Optimization	29
20	6	Background Estimation	39
21	6.1	Data-Driven Background Estimation Method	41
22	6.2	Validation of the Estimation Method	42
23	7	Signal CSC Cluster Simulation	49
24	7.1	Data and Monte Carlo samples	49
25	7.2	Selections	49
26	7.3	Cluster Efficiency	51
27	7.4	Cluster Identification Efficiency	53
28	7.5	Jet Veto Efficiency	53
29	7.6	Muon Veto Efficiency	54
30	7.7	Rechit and Segment Veto Efficiency	57
31	7.8	Cluster Time and Time Spread	59
32	7.9	Data Year Comparison	59
33	8	Uncertainties	63
34	8.1	Background Uncertainties	63
35	8.2	Signal Uncertainties	63
36	8.3	Impact Plots	66
37	9	Results	67
38	9.1	Signal Prediction	67
39	9.2	Signal Contamination	68
40	9.3	Observed Data	68
41	9.4	Expected and Observed Limits	69
42	10	Summary	73
43	A	CSC Rechit Studies	77

44	B	Era Comparison	79
45	B.1	Signal Efficiency Plots	79
46	B.2	Signal Cut Flow Table	79
47	B.3	Data Cut Flow Table for Individual Years	79
48	C	Issues in Run2 Data Taking	86
49	C.1	L1 EE Pre-firing	86
50	C.2	HEM15/16 Failure	86
51	D	Signal Cut Flow Table for 4 d and 4 τ Decay Modes	89
52	E	Cluster-Level BDT	95
53	E.1	BDT Validation	95
54	F	Supplementary Material	99
55	F.1	Cluster Efficiency	100
56	F.2	Cut-Based ID Efficiency	101

DRAFT

57 1 Introduction

- 58 Many well motivated BSM scenarios predict the production of long-lived particles (LLPs) at the
59 LHC [1]. These particles will typically decay into jets with a large branching fraction. Examples
60 of BSM models include split supersymmetry(SUSY) [2–7], SUSY with weak R -parity violation
61 (RPV) [8–11], SUSY with gauge-mediated supersymmetry breaking (GMSB) [12–14], “stealth
62 SUSY” [15, 16], “Hidden Valley” models [17–19], baryogenesis triggered by weakly interacting
63 massive particles (WIMPs) [20–22], and twin Higgs models [23–25].
- 64 In this note, we describe the first search for LLPs at CMS using the endcap muon system.
65 Instead of using the muon system to detect LLP decays to muons, we use the combination of
66 the Cathode Strip Chamber (CSC) stations and the iron material of the return yoke in between
67 the CSC stations as a sampling calorimeter to detect hadronic showers produced by hadronic
68 decays of long-lived particles (LLPs). We develop a novel technique of using geometrically
69 localized clusters of signals from the cathode-strip chambers to identify hadronic showers from
70 the decays of LLPs and distinguish it from backgrounds. The superior shielding of the CMS
71 detector (between 20 and 27 nuclear interaction lengths) provided by the hadronic calorimeter
72 and the iron return yoke eliminates the jet punch-through background that dominates for the
73 analogous muon spectrometer search from ATLAS.
- 74 Signal events are collected using the MET high level trigger and an offline skim requiring MET
75 > 200 GeV is required. Signals in the CSC system are reconstructed into hits and geometrically
76 near hits are clustered into localized objects using the DBSCAN algorithm. A cluster identifi-
77 cation criteria is applied which imposes varying η requirements depending on the number
78 of stations occupied and the station containing the bulk of the cluster hits, in order to further
79 enhance signal over background. Clusters with hits in certain locations are vetoed to suppress
80 punchthrough background and further enhance signal over background. Finally, the signal
81 events are extracted using an ABCD method with signal events enriched in the region with
82 low $\Delta\phi$ between the cluster location and the missing transverse momentum vector, and large
83 number of hits in the cluster.
- 84 The primary signal model benchmark that we will use to evaluate search sensitivity of this
85 analysis is Higgs boson mediated production of two long-lived scalars S with masses ranging
86 from a few GeV up to 55 GeV. This scalar is hypothesized to decay similar to a low mass Higgs
87 boson and therefore the decay modes are dominated by decays into a quark-antiquark pair or a
88 pair of tau-leptons. The proper lifetime of the LLP scalar S is a free parameter of the model and
89 will be scanned between about 1 cm and 100 m in this analysis. Due to the low mass scale of
90 the production mode, this benchmark model is among the most difficult to detect and trigger
91 on, and therefore provides a good point of comparison for the overall sensitivity of this search.
92 The sensitivity for most other alternative models mentioned above will be higher due to larger
93 production cross sections and presence of higher energy objects. This search focuses on events
94 without any leptons, and signal production modes from our benchmark model such as WH or
95 ZH, as well as alternative models that produce leptons are intended to be addressed by future
96 analyses specifically targetting final states that include leptons.
- 97 Previous searches providing competitive sensitivity to the benchmark model include the dis-
98 placed jet search from CMS [26], which yields competitive sensitivity for proper lifetimes below
99 0.2 m, and the muon spectrometer search from ATLAS [27, 28] based on a dataset with 36 fb^{-1} ,
100 which is the currently best published result for proper lifetimes above 1 m. We demonstrate
101 that our analysis yields unique sensitivity for LLP searches for large LLP lifetimes beyond
102 about 0.5 m. This search achieves better sensitivity than the displaced jet search using a tagger
103 based on secondary vertex information, for lifetimes larger than 0.1 to 0.5 m depending on the

104 mass of the LLP and its boost. The best sensitivity is achieved at LLP lifetimes between 1 and
105 5 m depending on the mass and boost of the LLP. For lifetimes larger than 100 m, we achieve
106 10 times better sensitivity than the previous best LHC result from ATLAS for the benchmark
107 model stated. Due to superior shielding and background suppression, our analysis requires the
108 detection of only one LLP decay, while the acceptance of the ATLAS search is more severely
109 suppressed at larger lifetimes due to the need to detect both LLP decays to suppress back-
110 grounds to sufficiently low levels.

DRAFT

2 Datasets

2.1 Data

The data used in this analysis is from the proton-proton collision data at $\sqrt{s} = 13$ TeV in 2016, 2017, and 2018, corresponding to 35.9, 41.5, and 59.7 fb^{-1} . The datasets used for this analysis is the MET-skim RECO dataset, listed in Table 1, which has a requirement that particle flow MET > 200 GeV. It is necessary to use the RECO data-tier, because the Rechits from the CSC system that are used to reconstruct clusters, the main object used to discriminate against background in this analysis, are only available in the RECO data-tier.

The global tags used to process the 2016, 2017, 2018 ABC, and 2018 D datasets are 80X_dataRun2_2016LegacyRepro_v4, 94X_dataRun2_v11, 102X_dataRun2_v12, and 102X_dataRun2_Prompt_v15, respectively. The JSON files used are Cert_271036-284044_13TeV_ReReco_07Aug2017_Collisions16_JSON.txt, Cert_294927-306462_13TeV_EOY2017ReReco_Collisions17_JSON.txt, and Cert_314472-325175_13TeV_17SeptEarlyReReco2018ABC_PromptEraD_Collisions18_JSON.txt.

The signal region defined in Section 5 will be blinded, and signal object and event selection optimization and background estimation validation are carried out in orthogonal control regions.

Table 1: RAW-RECO MET-skim datasets used in this analysis.

/MET/Run2016B-HighMET-07Aug17_ver1-v1/Raw-RECO
/MET/Run2016B-HighMET-07Aug17_ver2-v1/Raw-RECO
/MET/Run2016C-HighMET-07Aug17-v1/Raw-RECO
/MET/Run2016D-HighMET-07Aug17-v1/Raw-RECO
/MET/Run2016E-HighMET-07Aug17-v1/Raw-RECO
/MET/Run2016F-HighMET-07Aug17-v1/Raw-RECO
/MET/Run2016G-HighMET-07Aug17-v1/Raw-RECO
/MET/Run2016H-HighMET-07Aug17-v1/Raw-RECO
/MET/Run2017B-HighMET-17Nov2017-v1/Raw-RECO
/MET/Run2017C-HighMET-17Nov2017-v1/Raw-RECO
/MET/Run2017D-HighMET-17Nov2017-v1/Raw-RECO
/MET/Run2017E-HighMET-17Nov2017-v1/Raw-RECO
/MET/Run2017F-HighMET-17Nov2017-v1/Raw-RECO
/MET/Run2018A-HighMET-17Sep2018-v1/Raw-RECO
/MET/Run2018B-HighMET-17Sep2018-v1/Raw-RECO
/MET/Run2018C-HighMET-17Sep2018-v1/Raw-RECO
/MET/Run2018D-HighMET-PromptRECO-v1/Raw-RECO
/MET/Run2018D-HighMET-PromptRECO-v2/Raw-RECO

2.2 Signal Simulations

This analysis uses the Twin Higgs model as the benchmark model, in which two LLPs are pair produced from the Higgs boson, and each LLP decays to standard model particles. The Feynman diagram for this model is shown in Figure 2. The analysis is mainly sensitive to the gluon fusion production of the Higgs boson, but the other sub-dominant production mode, including the vector boson fusion (VBF), and associated production of a Higgs boson with a vector boson(VH) or a top quark pair (ttH) also have non-negligible contributions to the signal yield at high higgs p_T , as shown in the higgs p_T distributions in Fig. 1.

135 Due to the availability in the central production, we use the central production for gluon fusion
 136 and vector boson fusion, and privately produced signal samples for the other production
 137 modes.

138 Since the events in MC are simulated with a pileup distribution that is a best guess of the final
 139 distribution in data, so all simulated samples are reweighted to the actual pileup distribution
 140 measured in data. The latest central pileup files[29] are used for the pileup distribution in data.

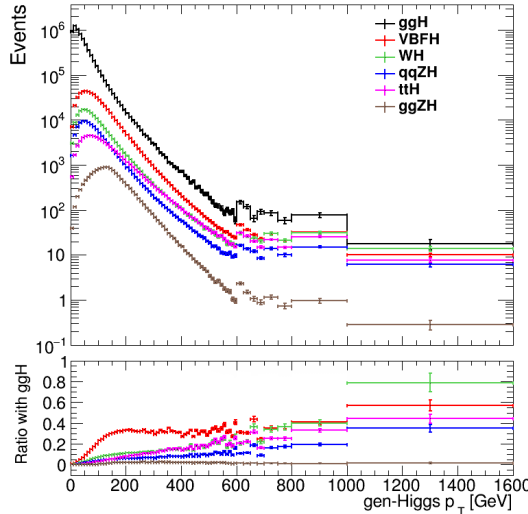


Figure 1: The gen-level higgs p_T distribution for the different production modes of the Higgs boson and the ratio with gluon fusion is shown. The sub-dominant production modes provide non-negligible contribution to the signal yield at high higgs p_T . The gluon fusion distribution is reweighted to the best known theoretical prediction (NNLOPS). The reweighting procedure is detailed in subsection 2.2.4.

141 2.2.1 Central Production for Gluon Fusion and Vector Boson Fusion

142 We used the centrally produced signal samples for 2016, 2017, and 2018 conditions. The centrally produced samples cover LLP masses of 7, 15, 40, and 55 GeV, as recommended by the LHC Higgs Cross-Section Working Group, and with proper lifetime $c\tau$ of 0.001, 0.01, 0.1, 1, 10, 100m. Furthermore, 3 different decay modes of the LLP are generated, with 4b, 4d and 4 τ final states respectively. Due to the heavier mass of bottom quark, only LLP masses of 15, 40, and 55 GeV are generated for the 4b final state. These samples include the gluon fusion production mode of the Higgs boson for all 3 decay modes, while the vector boson fusion (VBF) production mode of the Higgs boson is only produced for the 4b and 4 τ final states. The VBF production mode of the Higgs Boson with 4d final states are produced privately. The complete list of central signal simulation samples are shown in Table. 2. We use the NNNLO cross section of 48.58 pb for the gluon fusion Higgs signal sample and the NNLO cross section of 3.78 pb for the VBF Higgs production from the LHC Higgs Cross Section working group yellow report 4 [30].

154 2.2.2 Private Production for Associated Productions

155 We produced private signal samples in 2018 condition for additional production modes that the analysis is sensitive to, including VBF (4d final state only), WH, ZH, and ttH. The samples are generated using the same versions of POWHEG V2 used for the official Higgs samples using the same gridpacks. The privately produced samples cover the same LLP masses and proper

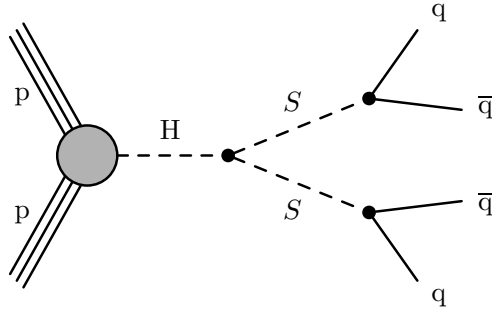


Figure 2: Feynman diagram for the Higgs to long-lived scalar particle model used as the benchmark model for this search.

Table 2: Signal Simulations for ggH and VBFH used in this analysis.

Samples	$\sigma(\text{pb})$
/ggH_HToSSTobb_MH-125_Tune*13TeV-powheg-pythia8/*GEN-SIM-RECO	48.58
/VBFH_HToSSTo4b_MH-125_Tune*13TeV-powheg-pythia8/*GEN-SIM-RECO	3.78
/ggH_HToSSTodd_MH-125_Tune*13TeV-powheg-pythia8/*GEN-SIM-RECO	48.58
/ggH_HToSSTo4Tau_MH-125_Tune*13TeV-powheg-pythia8/*GEN-SIM-RECO	48.58
/VBFH_HToSSTo4Tau_MH-125_Tune*13TeV-powheg-pythia8/*GEN-SIM-RECO	3.78

159 life time as the centrally produced samples. They cover LLP masses of 7, 15, 40, and 55 GeV,
 160 and with proper lifetime $c\tau$ of 0.1, 1, 10, 100m. Samples with proper life times shorter than
 161 0.1 m are not produced, due to the lack of sensitivity in this analysis. Similar to the centrally
 162 produced samples, 3 different decay modes of the LLP are generated, with 4b, 4d and 4 τ final
 163 states respectively. In addition, for completeness, we privately produced samples with VBF
 164 production modes for the 4d final states.

165 The complete list of private signal simulation samples and the corresponding NNLO cross
 166 sections are shown in Table. 3. The NNLO cross section are taken from the LHC Higgs Cross
 167 Section working group yellow report 4 [30]. Note that the ZH signal samples only include the
 168 quark-initiated ZH production. The predicted signal yield for gluon-initiated ZH production
 169 is obtained from reweighting the higgs p_T and η distribution from the qqZH samples. We use
 170 the NNLO cross section of 0.1227pb for the gluon-initiated ZH production mode from the LHC
 171 Higgs Cross Section working group yellow report 4 [30]. The reweighting procedure has been
 172 validated with a set of privately-generated ggZH samples. We propagate an additional 20%
 173 systematics on the reweighting procedure to obtain the ggZH signal yield.

Table 3: Signal Simulations for the associated production modes.

Samples	$\sigma(\text{pb})$
/VBFHToSS_STodd_ms*_pl*/*USER	3.782
/WminusHToSS_STo*_ms*_pl*/*USER	0.5328
/WplusHToSS_STo*_ms*_pl*/*USER	0.8400
/ZHToSS_STo*_ms*_pl*/*USER	0.7612
/ttH_HToSS_STo*_ms*_pl*/*USER	0.5071

174 2.2.3 LLP Lifetime Reweighting

175 Only a discrete number of LLP lifetimes are simulated. Therefore samples with intermediate
 176 lifetimes can be generated by reweighting from the available signal samples.

Since the decay position of the two LLPs in each event are independent, and each LLP decays with an exponential probability, the distribution of events is simply the product of the two LLP decay probabilities:

$$p(t_1, t_2 | \tau) = \frac{1}{\tau^2} \exp^{-t_1/\tau} \exp^{-t_2/\tau} \quad (1)$$

177 where t_1 and t_2 is the life-time of the first LLP and second LLP in their own rest frame respec-
 178 tively, given by $t_i = \frac{\text{LLP travel distance (lab frame)}}{\gamma_i \times \beta_i}$, where γ_i and β_i are the Lorentz factor and velocity
 179 of the i-th LLP respectively.

To obtain a sample with lifetime τ_{new} from a sample with lifetime τ_{old} , we assign a weight, which is the ratio of equation 1 with parameter τ_{new} and τ_{old} to the original sample:

$$w = \left(\frac{\tau_{old}}{\tau_{new}} \right)^2 \exp[(t_1 + t_2) \times \left(\frac{1}{\tau_{old}} - \frac{1}{\tau_{new}} \right)] \quad (2)$$

180 Practically, each intermediate life-time is reweighted using the two centrally-produced signal
 181 samples with life-times closest to the intermediate life-time. For events where the sum of the
 182 two LLP proper life-times is greater than half of the larger life-time, the weights from the sam-
 183 ple with the larger life-time is used, otherwise, the weight from the sample with shorter life-
 184 time is used. For example, to obtain a sample with life-time of 3 m, centrally-produced signal
 185 samples with life-time of 1 m and 10 m are used. For events where the sum of the two LLP life-
 186 times is greater than 5 m, weights from the 10 m sample is used, otherwise, weights from the
 187 1 m sample is used. This choice is made such that the weights are always small and minimizes
 188 the statistical uncertainty of the reweighted sample.

189 2.2.4 Higgs p_T spectrum correction.

190 The gen-level p_T of the higgs for ggH production mode is reweighted to the best known theo-
 191 retical prediction (NNLOPS) [31]. The distribution of the higgs p_T from the centrally produced
 192 signal sample and theoretical prediction is shown in Fig. 3. The binning is chosen such that the
 193 statistical uncertainty is less than 10% in each bin: [0, 10, 20, 30, 40, 50, 60, 70, 80, 90, 100, 110,
 194 120, 130, 140, 150, 160, 170, 180, 190, 200, 210, 220, 230, 240, 250, 260, 270, 280, 290, 300, 310, 320,
 195 330, 340, 350, 360, 370, 380, 390, 400, 410, 420, 430, 440, 450, 460, 470, 480, 490, 500, 510, 520, 530,
 196 540, 550, 560, 570, 580, 590, 600, 625, 650, 675, 700, 750, 800, 1000, 1600]. The Higgs p_T correction
 197 increases the signal yield by a few %, as shown in Table 4.

Table 4: Increase in signal yield in the signal region. There are no events selected in the signal region for the 55 GeV and $c\tau = 0.1$ m signal sample.

	$c\tau = 0.1\text{m}$	$c\tau = 1\text{m}$	$c\tau = 10\text{m}$	$c\tau = 100\text{m}$
15 GeV	5.11%	1.48%	2.47%	0.65 %
40 GeV	7.28%	0.84%	2.18%	4.28 %
55 GeV	\	4.22%	2.9%	3.13 %

198 2.3 Background simulation

199 Since the RECO dataset is used for this analysis, there are no centrally produced background
 200 MC simulation samples available.

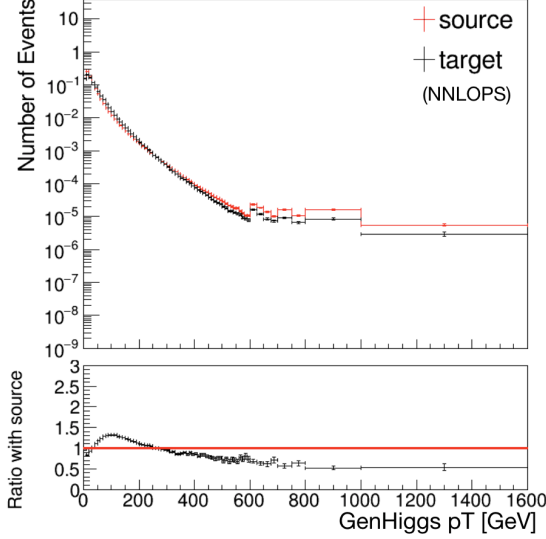


Figure 3: The generator level higgs p_T of the source (centrally produced signal sample) and target (NNLOPS) is shown. The bottom subplot is higgs p_T weight, the ratio between target and source. The binning is chosen such that the statistical uncertainty in each bin is less than 10%.

201 Background simulations in AOD format have been used to help with understanding specific
 202 details of CSC showers produced by the muon bremsstrahlung process, as detailed in Section 5.
 203 In those cases, clusters of CSC segments were used as only those are available in the AOD data-
 204 tier, and only MC samples from the Summer 16 campaign were used because the CSC segment
 205 reconstruction sequence was changed for the Fall17 and Autumn18 campaigns such that signal-
 206 like segments were no longer reconstructed. The list of samples used are listed in Table. 5.

Table 5: WJetsToLNu MC samples used in the analysis.

```
/WJetsToLNu_HT-100To200_TuneCUETP8M1_13TeV-madgraphMLM-pythia8/*/AODSIM
/WJetsToLNu_HT-200To400_TuneCUETP8M1_13TeV-madgraphMLM-pythia8/*/AODSIM
/WJetsToLNu_HT-400To600_TuneCUETP8M1_13TeV-madgraphMLM-pythia8/*/AODSIM
/WJetsToLNu_HT-600To800_TuneCUETP8M1_13TeV-madgraphMLM-pythia8/*/AODSIM
/WJetsToLNu_HT-800To1200_TuneCUETP8M1_13TeV-madgraphMLM-pythia8/*/AODSIM
/WJetsToLNu_HT-1200To2500_TuneCUETP8M1_13TeV-madgraphMLM-pythia8/*/AODSIM
/WJetsToLNu_HT-2500ToInf_TuneCUETP8M1_13TeV-madgraphMLM-pythia8/*/AODSIM
```

207 **3 Trigger**

208 For signal scenarios where the LLP lifetime is relatively long, such that one or more LLPs decay
 209 beyond the calorimeters, a significant amount of MET will be produced as the LLP momentum
 210 remains undetected. In the benchmark twin higgs signal model, for events where the Higgs
 211 boson is produced with significant recoil from initial state radiation (ISR), a large MET is pro-
 212 duced. This feature is illustrated in the cartoon in Fig. 4 and the correlation between higgs p_T
 213 and MET in Fig. 5. This analysis utilizes this feature by triggering on the MET-based triggers,
 214 summarized in Table 6.

Table 6: Trigger paths used in the analysis.

Year	Trigger paths
2016	HLT_PFMETNoMu120_PFMHTNoMu120_IDTight
2017	HLT_PFMETNoMu120_PFMHTNoMu120_IDTight OR HLT_PFMETNoMu140_PFMHTNoMu140_IDTight OR HLT_PFMETNoMu120_PFMHTNoMu120_IDTight_PFHT60
2018	HLT_PFMETNoMu120_PFMHTNoMu120_IDTight OR HLT_PFMETNoMu140_PFMHTNoMu140_IDTight OR HLT_PFMETNoMu120_PFMHTNoMu120_IDTight_PFHT60

215 The “NoMu” version of the MET trigger is used in order to facilitate the measurement of the
 216 trigger efficiency using events triggered on Single Muon triggers as the PFMETNoMu120 trig-
 217 ger is not biased by the presence of a muon in the trigger efficiency measurement sample. The
 218 performance of the PFMET120 and PFMETNoMu120 is the same for our event sample as we
 219 do not accept events containing muons.
 220 The efficiency of the trigger and offline MET cut of 200 GeV from the MET skim, calculated with
 221 respect to the geometric acceptance, ranges from 0.5% to 2% depending on the signal model.
 222 It’s summarized in the signal efficiency tables (Table 10, 11, and 12) in Section 5.

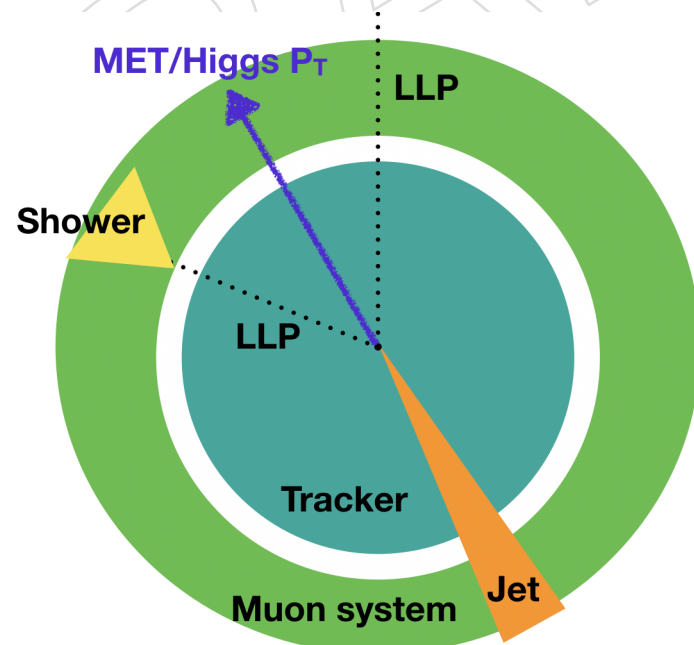


Figure 4: The MET from signal comes from the recoil of the Higgs against ISR.

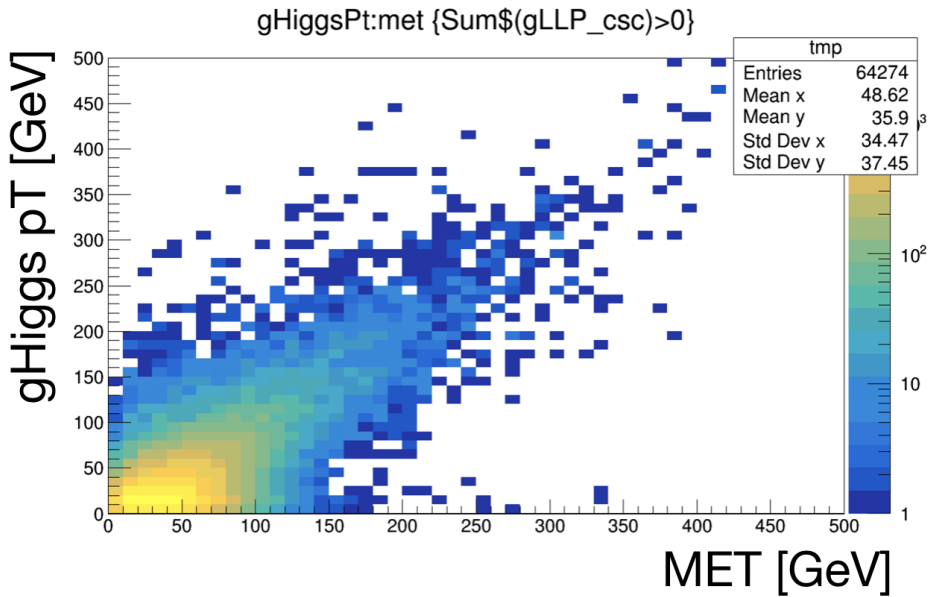


Figure 5: Strong correlation is observed between MET and the gen-level Higgs p_T for the twin Higgs benchmark model.

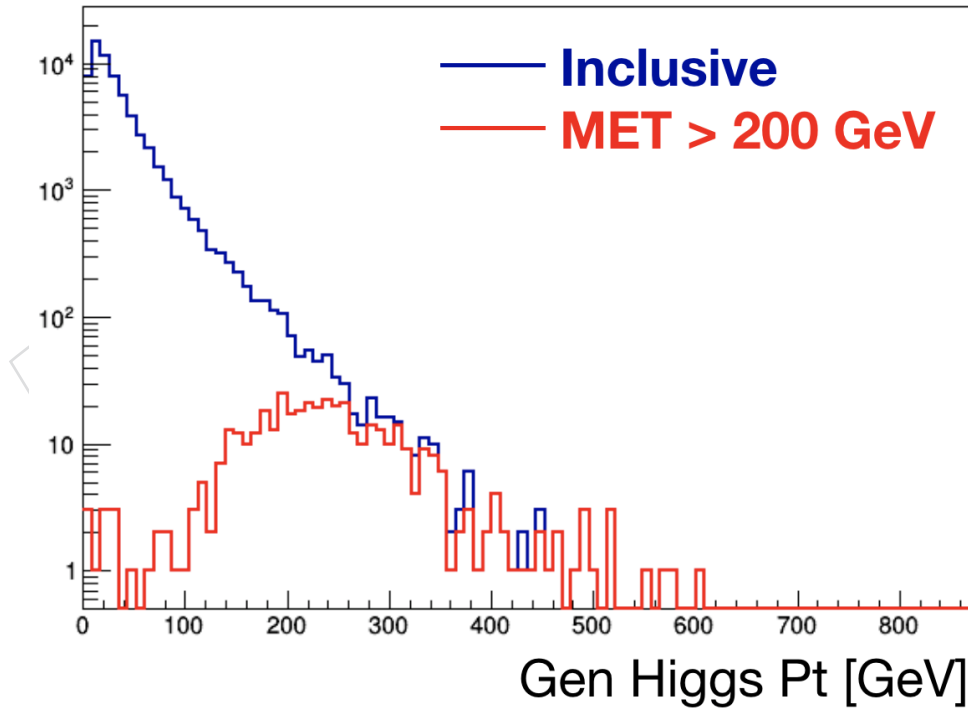


Figure 6: Generator level Higgs p_T before and after the MET cut in the signal sample. We have required at least 1 LLP to decay in the CSC system for this plot.

223 3.1 Trigger Efficiency Scale Factor

224 The trigger efficiency is measured in a control region for data and simulation to correct for any
225 mismodelling of trigger efficiency. The efficiency is measured using the SingleMuon dataset

and WJetsToLNu MC samples. The events are required to pass the HLT_IsoMu27 trigger and has exactly 1 reconstructed muon and the muon is required to have p_T between 30 and 100 GeV and passes the tight identification and isolation requirement [32]. The 100 GeV cut on muon p_T cleans the sample from events with high momentum muons that might be mismeasured. Furthermore, the events are required to pass all the MET filters, described in Section 4. The trigger efficiency is measured as a function of missing transverse momentum calculated ignoring the muon in the event. The measurement is performed separately for each year, as shown in Fig. 7.

The Data/MC ratio of the trigger efficiency is applied to the MC signal samples to correct for the mismodelling of the trigger efficiency. Inclusively, the application of the scale factor correction decreases the signal yield by 5% in all the signal models.

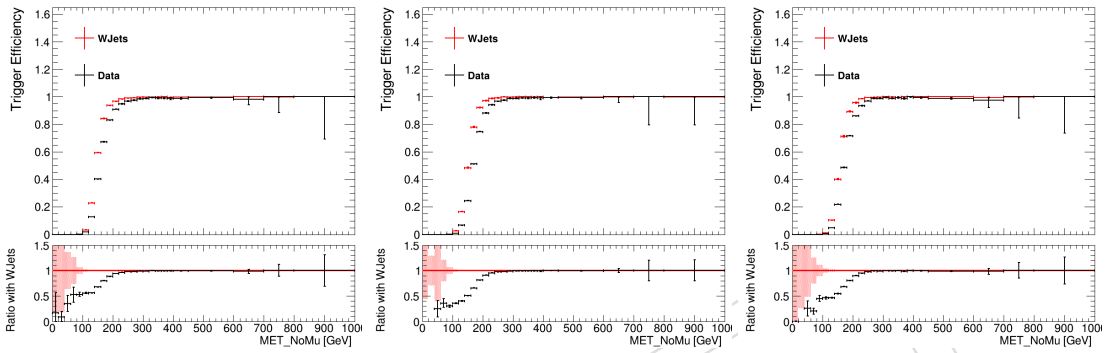


Figure 7: The trigger efficiency as a function of MET NoMu, for data and MC in 2016 (Left), 2017 (Middle), and 2018 (Right) condition.

4 Object reconstruction and identification

Reconstructed objects used in this analysis and identification criteria are discussed below. This analysis is primarily based on the reconstruction and identification of hit clusters in the CSC muon system resulting from hadronic showers originating in the layer of material just prior (closer to the interaction point) to each CSC muon station. We also use jets and muon objects to veto jet punchthrough and muon bremsstrahlung background. Finally, the MET is used to trigger the event and select events with large boost of the Higgs boson.

4.1 CSC Rechit Clusters

For LLPs that decay within or just prior to the CSC muon system, the material in the iron return yoke structure will induce a hadronic shower, creating a geometrically localized and isolated cluster of signal hits in the CSC system. The event display for an example signal event is shown in Fig. 8.

When charge particles traverse the CSC chambers, signal pulses are collected on the anode wires and the cathode strips. The signals from wire groups are combined with signals from the cathode strips to form a two-dimensional point on each chamber layer called a CSC rechit. Six layers make up each chamber. These rechits are then used to form straight-line segments comprising at least three layers in the chamber.

Reconstructed CSC segments were initially studied as they were readily available in AOD datasets, but the segment reconstruction algorithm results in saturation due to the excessively large number of hits in a small region of the detector. Only a limited number of segments was reconstructed and only a limited fraction of hits in the shower are recognized as making a line segment, while the majority of the hits are distributed randomly. Therefore, the large number of hits in the signal samples are not reflected in the number of segments. Furthermore, for the 2017 and 2018 datasets changes to the segment reconstruction suppressed signal efficiency to negligible levels. Based on these factors, we chose to use CSC Rechits to reconstruct and identify these hadronic showers. A detailed study on the validation of CSC Rechits for signal-like hadronic showers are presented in Appendix A.

One practical consequence of the choice to use CSC Rechits to reconstruct clusters is that we are forced to use the MET trigger and MET offline skim requirement of 200 GeV for the search. This is because the RECO datatier which contains the CSC Rechits are only available for the MET skim dataset. This choice limits the signal acceptance to below a few percent. A trigger path based on the CSC Rechit cluster alone is being developed for Run 3, which would allow the search to be performed without the need for the MET requirement, potentially increasing the signal acceptance by more than an order of magnitude.

CSC Rechit clusters are defined by clustering CSC Rechits by their η and ϕ position. We use the Density-based spatial clustering of applications with noise (DBSCAN) algorithm [33], using $\Delta R = 0.2$ as the distance parameter and require a minimum of 50 Rechits per cluster. Finally, we merge two clusters that are nearby if the ΔR between the two clusters are < 0.6 , until all clusters within an event are isolated. This merging procedure ensures that clusters coming from the same source are reconstructed as one object. The fraction of LLP decays occurring within the CSC geometric acceptance region in signal events that produce a successfully reconstructed cluster using this algorithm is defined as the "clustering efficiency" and is shown in Fig. 9 for several LLP masses. The efficiency is above 80% throughout the detector, except when the LLP decays near the outer edges of the CSC. This efficiency is independent of the detector condition, as demonstrated in Section B. While some amount of shielding absorber material is

281 required to induce the shower, too much shielding material will also stop shower secondaries
 282 and suppress the detector response. For example, when the decay occurs in the active gaseous
 283 region of ME4 there is no steel absorber material to induce a shower, thus suppressing the
 284 cluster reconstruction efficiency.

285 The minimum Rechit requirement is chosen such that its large enough to select a shower rather
 286 than a muon. A muon would create at most 24 Rechits in the CSC (6 Rechits per station, for the
 287 4 stations in CSC). Therefore, we require at least 50 Rechits per cluster, such that there would
 288 be about twice the number of Rechits in the cluster compared to a muon. This minimum Rechit
 289 parameter is only used to define a threshold and has little impact on the final signal efficiency,
 290 because a more stringent cut on the number of Rechits in clusters will be applied ($N_{rechits} \geq 130$)
 291 in the final signal extraction procedure, as described in Section 5. A test was implemented
 292 by decreasing the minimum Rechit to 30 Rechits. An increase of 5% in the inclusive cluster
 293 efficiency is observed, but the increase comes from CSC clusters that have a small number of
 294 Rechits. There is no increase in signal when a $N_{rechits}$ cut of 130 is applied, as shown in the
 295 $N_{rechits}$ distributions in Fig. 10.

296 The distance parameter used in the clustering algorithm is motivated by the ΔR spread of the
 297 clusters. The ΔR spread is defined as $\sqrt{\frac{\sum (\eta_i - \bar{\eta})^2 + (\phi_i - \bar{\phi})^2}{N}}$, where η_i and ϕ_i are the η and ϕ position
 298 of the i-th RecHit, $\bar{\eta}$ and $\bar{\phi}$ are the η and ϕ position of the center of the cluster, and N is the
 299 number of RecHits in the cluster. The ΔR spread distribution of CSC Rechit clusters clustered
 300 with several distance parameters is shown in the left plot in Fig. 11. For all 3 distributions in
 301 the plot, more than 90% of the clusters have a ΔR spread of below 0.2. Therefore, we choose
 302 a $\Delta R = 0.2$ as the distance parameter. However, the clustering efficiency is not very sensitive
 303 to the parameters. Decreasing the distance parameter from 0.2 to 0.1 results in a 3% decrease
 304 in inclusive clustering efficiency for the sum of all signal models and increasing the distance
 305 parameter from 0.2 to 0.3 results in a 1% increase in inclusive clustering efficiency for the sum
 306 of all signal models. Furthermore, modifying the ΔR also doesn't alter the shape of the $N_{Rechits}$
 307 distribution, as shown in the right plot of Fig. 11.

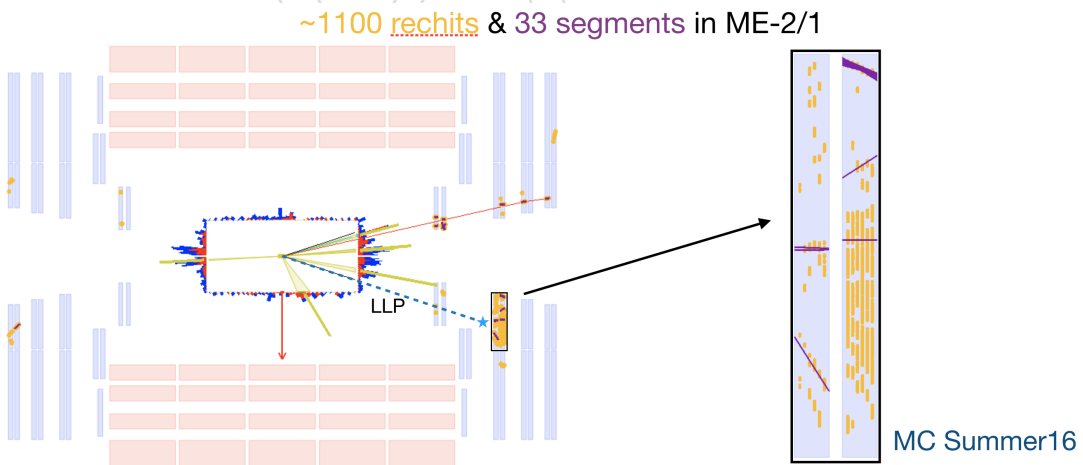


Figure 8: An event display of a signal event. There are 1100 rechits (yellow dots) but only 33 segments (purple line segments) reconstructed. Rechits provide much better discrimination between signal and background.

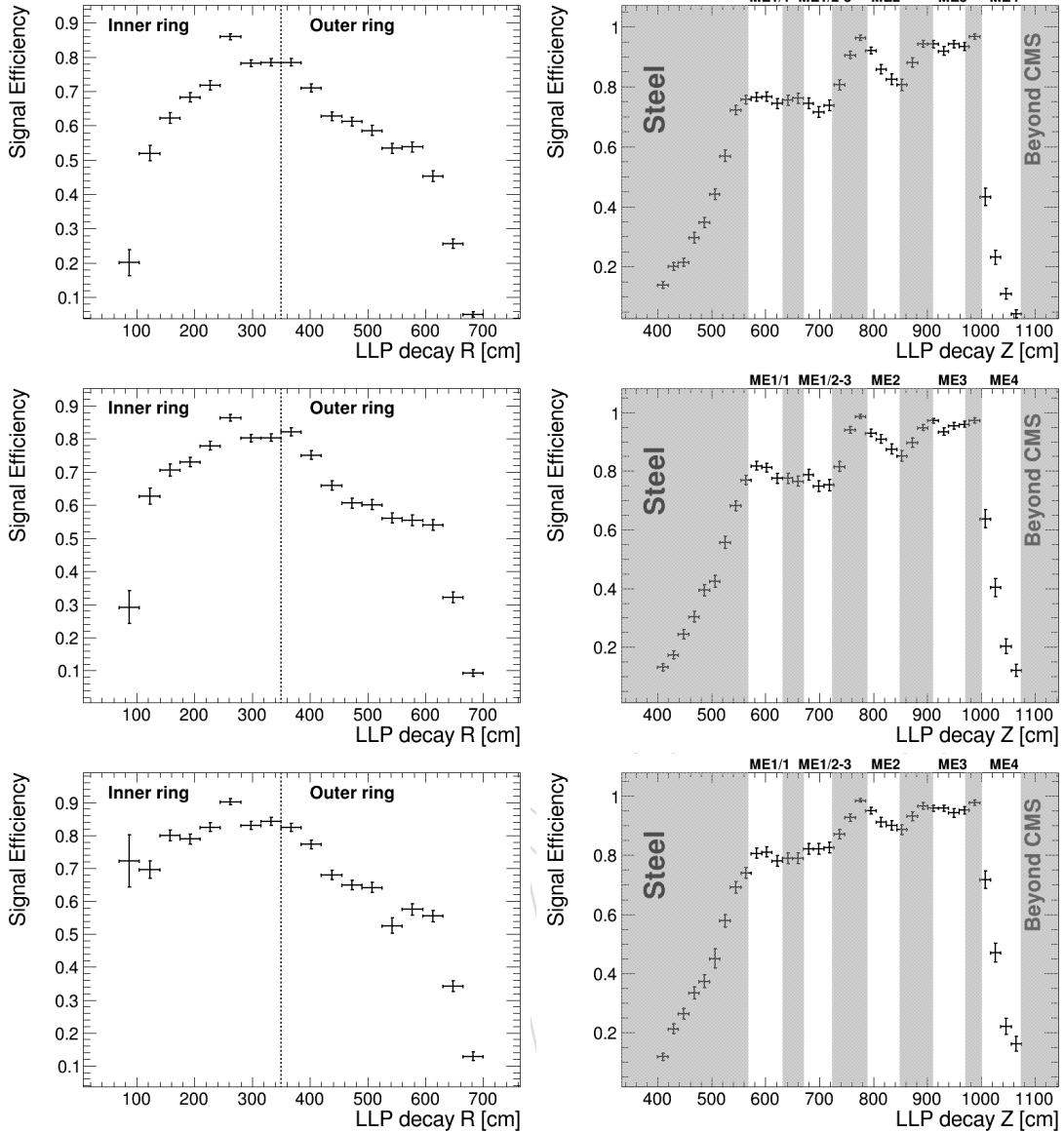


Figure 9: The “clustering efficiency”, defined as the fraction of LLPs in signal events that decay within the CSC geometric acceptance region and produce a successfully reconstructed cluster is shown as a function of the LLP decay position in the radial direction (left) and the Z direction (right). Scenarios with LLP mass of 15 (Top), 40 (Middle), and 55 GeV (Bottom) are shown separately. The signal sample for each LLP mass includes the sum of all available lifetimes. This efficiency is flat throughout the detector, except when the LLP decays near the outer edges of the CSC (in both r and z), where there is limited space for the detector to register all the RecHits from the shower. It is also observed that the fraction is the highest when the LLP decays in the steel right before the sensitive region, and the efficiency decreases as the LLP decays later in the station. The trend with respect to the decay radius corresponds to the geometry of the CSC system. The CSC is longer in the z-direction, with more shielding between station 1 and station 2 when $|r| < 2.5$ m, resulting in a smaller clustering efficiency in this region.

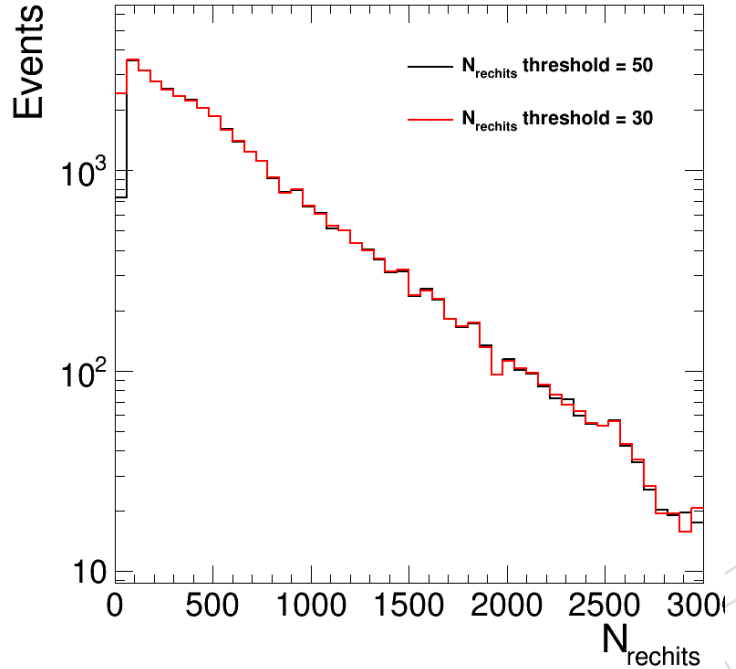


Figure 10: The N_{rechits} distribution scanning the Rechit threshold of the clustering algorithm.

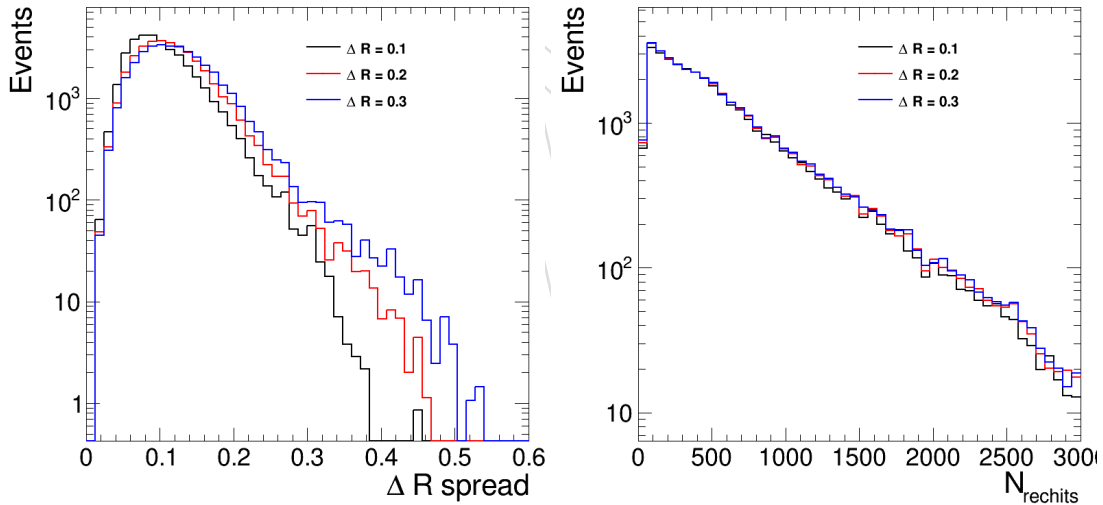


Figure 11: The ΔR spread (Left) and N_{rechits} (Right) distributions scanning the ΔR parameters of the clustering algorithm.

4.2 Primary Vertex

The standard primary vertex selection is used. The selected primary vertex is the one with the largest sum p_T^2 .

4.3 Jets

Jets are reconstructed by clustering PF candidates with the anti- k_T algorithm with distance parameter of 0.4. The charged particles from non-primary vertices (pileup) are removed before clustering, using the Charge Hadron Subtracted (CHS) algorithm. The jet energy corrections are applied to data and MC according to the latest recommendation from JETMET POG[34]. A

summary of the applied JEC versions is shown in Table 7. The jet energy scale uncertainty is propogated as a source of signal systematic in the final result, detailed in Section 8.

Table 7: Summary of JEC Global Tags Used for Data and MC

Data 2016 BCD	Summer16_07Aug2017BCD_V11_DATA
Data 2016 EF	Summer16_07Aug2017EF_V11_DATA
Data 2016 GH	Summer16_07Aug2017GH_V11_DATA
Data 2017 B	Fall17_17Nov2017B_V32_DATA
Data 2017 C	Fall17_17Nov2017C_V32_DATA
Data 2017 DE	Fall17_17Nov2017DE_V32_DATA
Data 2017 F	Fall17_17Nov2017F_V32_DATA
Data 2018 A	Autumn18_RunA_V19_DATA
Data 2018 B	Autumn18_RunB_V19_DATA
Data 2018 C	Autumn18_RunC_V19_DATA
Data 2018 D	Autumn18_RunD_V19_DATA
MC 2016	Summer16_07Aug2017_V11_MC
MC 2017	Fall17_17Nov2017_V32_94X_MC
MC 2018	Autumn18_V19_MC

In this analysis, PF jets with $p_T > 10$ GeV and $|\eta| < 2.4$ are used to veto CSC cluster caused by punchthrough jets if the CSC cluster centroid is within $\Delta R < 0.4$ of the PF jet. This suppresses clusters that are produced by either a jet punching through the shielding or by a K_L produced in the hadronization of the jet decaying within the CSC geometric acceptance region in the same way as a signal LLP. The inefficiency of this jet veto on signal is caused by random matching to pileup jets. We measure the signal efficiency for this jet veto to be about 92% by randomly selecting cluster positions in the signal cluster distribution and measuring how often a random match is made with pileup jets from ZToMuMu events in data and MC. This measurement agrees with simulation prediction to within 1.5%. The validation study of the jet veto efficiency is detailed in Section 7.

Events are also required to have at least one jet with $p_T > 50$ GeV passing the TightLepVeto ID[35], and with $\Delta R > 0.4$ to the CSC cluster because the large MET requirement implies that a high p_T ISR jet is recoiling against the Higgs boson in signal events. We apply the recommended TightLepVeto ID following the Run2 recommendations from the JETMET POG twiki [35].

4.4 Muons

Standard muon reconstruction is used to construct muon candidates [36].

Muon objects with $p_T > 20$ GeV and $|\eta| < 2.4$ are used to veto CSC clusters caused by muons producing a photon via bremsstrahlung if the CSC cluster centroid is within $\Delta R < 0.4$ of the muon. No muon ID requirements are applied to muons used for the veto. Therefore, the muons can be a TrackerMuon, StandAlone Muon, or a GlobalMuon. The efficiency of this muon veto is about 90%.

Events with isolated muons with $p_T > 25$ GeV, $|\eta| < 2.4$, and passing the Muon POG loose ID criteria [32], with 3D impact parameter significance less than 4, and relative isolation less than 0.25 are also vetoed in order to suppress W+jets and top quark backgrounds.

343 **4.5 Electrons**

344 Electrons are reconstructed with the Gaussian Sum Filter algorithm [37]. In the analysis, we
 345 veto events with isolated electrons with $p_T > 35 \text{ GeV}$, $|\eta| < 2.4$ and passing the EGamma POG
 346 loose electron ID criteria [38] to suppress W+jets and top quark backgrounds. The loose ID
 347 requirement for each data-taking period is applied by following the recommendations from
 348 EGamma POG [38].

349 **4.6 Missing Transverse Momentum**

350 The missing transverse momentum used in this analysis is the Type-I Corrected PFMET[39],
 351 which is the negative of the vector sum of all particle flow candidates in the event. The Type-
 352 I Corrected PFMET uses the AK4PF jet collections and propagates the jet energy corrections
 353 (JEC) to p_T^{miss} .

354 The xy-Shift correction is applied to reduce the MET ϕ modulation. The correction has a large
 355 effect on the MET ϕ shape when MET is small, but the MET requirement is $> 200 \text{ GeV}$ in our
 356 analysis. The correction has a small (1%) effect for both the signal and background yield, as
 357 expected.

358 For the 2017 data, the p_T^{miss} measurement is affected by an issue that causes the EE towers to
 359 be noisy. To mitigate this effect, we follow the recommended recipe[40] to fully drop jets with
 360 $2.65 < |\eta| < 3.139$ and $p_T(\text{raw}) < 50 \text{ GeV}$ in the p_T^{miss} calculation. We apply this recommended
 361 recipe for 2017 data and MC events (corresponding to 2017 data).

362 In many cases, large MET can be caused not only by physics process from collisions, such as
 363 the production of invisible particles, but also could come from unwanted noise, such as detec-
 364 tor noise, cosmic rays, and beam-halo particles. Therefore, to identify the "fake" MET induced
 365 by the non-collisional background, the MET filters are applied based on the recommendations
 366 from the JETMET group[41] for both data and MC, as shown in Table 8. The signal efficiency
 367 of the MET filters is above 98% for all signal models, as shown in Table 10, 11, and 12.

368
 Table 8: List of MET filters used in the analysis.

Filter	Years	Applied to Data	Applied to MC
primary vertex filter	2016, 2017, and 2018	Yes	Yes
beam halo filter	2016, 2017, and 2018	Yes	Yes
HBHE noise filter	2016, 2017, and 2018	Yes	Yes
HBHEiso noise filter	2016, 2017, and 2018	Yes	Yes
ECAL TP filter	2016, 2017, and 2018	Yes	Yes
Bad PF Muon Filter	2016, 2017, and 2018	Yes	Yes
ee badSC noise filter	2016, 2017, and 2018	Yes	No
ECAL bad calibration filter	2017 and 2018	Yes	Yes

369 5 Event Selection

370 This section details the list of event selections and CSC Rechit cluster identification applied
 371 that defines the signal region for this analysis. The event-level selections are only used to select
 372 for the high MET phase space, while a number of discriminating variables are used to tag a
 373 signal-like CSC Rechit cluster to reject background from showering muons and punch-through
 374 jets that may reach the CSC. For all plots in this section, the signal distributions consist of all
 375 available mass/ $c\tau$ points for the ggH production mode and 4b decay mode, and the total signal
 376 efficiency is used as a metric to evaluate the cuts. The signal efficiency of each model for all the
 377 selections are summarized in the signal cut flow tables in Table 10, 11, and 12.

378 The RECO skim being used has already a cut on MET > 200 GeV, so we keep the 200 GeV cut.
 379 As this analysis targets the gluon-fusion production mechanism, we veto any events that have
 380 electrons (muons) with $|\eta| < 2.5$ (2.4) and $p_T > 35$ (25) GeV and pass the POG-defined loose
 381 identification criteria. The signal efficiency of the lepton veto is more than 99% for all the signal
 382 models, summarized in Table 10, 11, and 12. This lepton veto suppresses W+jets and top-pair
 383 production background processes. The lepton veto is also motivated by the anticipation of a
 384 complementary search using leptonic final states triggered by single electron and single muon
 385 triggers. The different p_T thresholds used for the electron and muon veto are motivated by
 386 different trigger turn-on thresholds for the single electron and single muon triggers. This veto
 387 will ensure that the current analysis and the complementary analysis with leptonic final states
 388 remain mutually exclusive and can be easily statistically combined.

389 For signal events, the large MET requirement implies that a high p_T ISR jet is recoiling against
 390 the Higgs boson and therefore we require at least one jet with $p_T > 50$ GeV and $|\eta| < 2.4$,
 391 passing the TightLepVeto jet ID criteria defined by the JetMET POG. The signal efficiencies are
 392 94%-98% for the different signal models, summarized in Table 10, 11, and 12. The shape of the
 393 leading jet p_T distributions for signal and background are shown in Fig. 12.

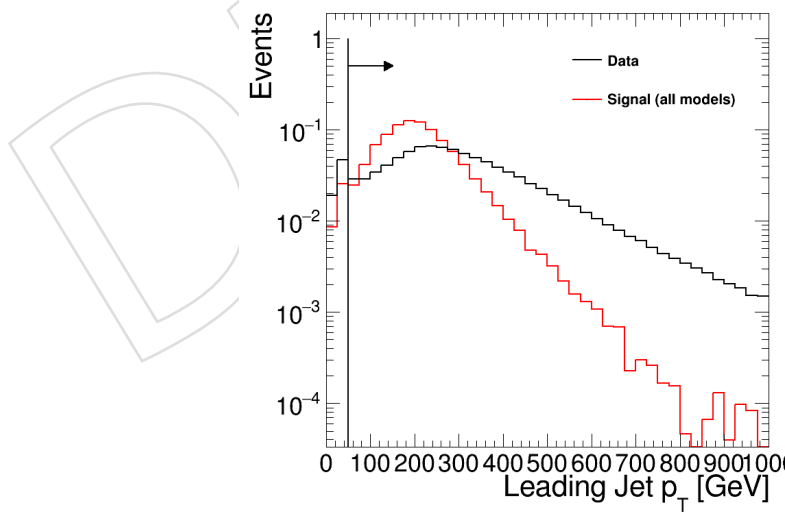


Figure 12: The distributions of the leading jet p_T for data signals from all available mass/ $c\tau$ points in acceptance that pass the other event level selections.

394 5.1 Cluster Selection

395 The dominant background processes producing signal-like clusters are jets that punch through
 396 the shielding and muons that undergo bremsstrahlung in the material within or near the muon

397 system. Such processes can produce a large number of localized CSC Rechits. Jet punchthrough
 398 and muon bremsstrahlung from highly boosted W boson decays produce backgrounds for
 399 which the cluster and the MET point in the same direction. For jet punchthrough, this is be-
 400 cause both the cluster and the MET are produced by the same punchthrough jet. For the muon
 401 bremsstrahlung background, it is because the W boson is highly boosted and the muon and
 402 neutrino momentum are very close in direction. Because the cluster and MET tend to point
 403 in the same direction, such backgrounds pose a problem for the ABCD background estimation
 404 method that will be described in Section 6. Therefore we must use very aggressive vetos in
 405 order to suppress such backgrounds to negligible levels.

406 To suppress CSC Rechit clusters from punch-through jets and muons that undergo bremsstrahlung
 407 in the muon system, clusters that are geometrically matched to any jets or muons are vetoed.
 408 A cluster is vetoed if it is matched to any PF jet with $p_T > 10$ GeV and $|\eta| < 2.4$ to within
 409 $\Delta R < 0.4$. No jet ID requirements are applied to jets used for this veto. A cluster is vetoed
 410 if it is matched to any muons with $p_T > 20$ GeV and $|\eta| < 2.4$, within $\Delta R < 0.4$. No muon
 411 ID requirements are applied to muons used for the veto. Therefore, the muons can be a Track-
 412 erMuon, StandAlone Muon, or a GlobalMuon. The p_T cut for both the jet and muon vetoes
 413 is determined from studying the segment clusters from 2016 signal samples and 2016 WJet-
 414 sToLNu samples, by keeping the signal efficiency to 90%. The distribution of the p_T of jets
 415 and muons that background and signal segment clusters are matched to is shown in Fig. 13.
 416 The signal efficiency for the vetos on RecHits clusters are both about 90% for different signal
 417 models, verified in the signal efficiency tables shown in subsection 5.3.

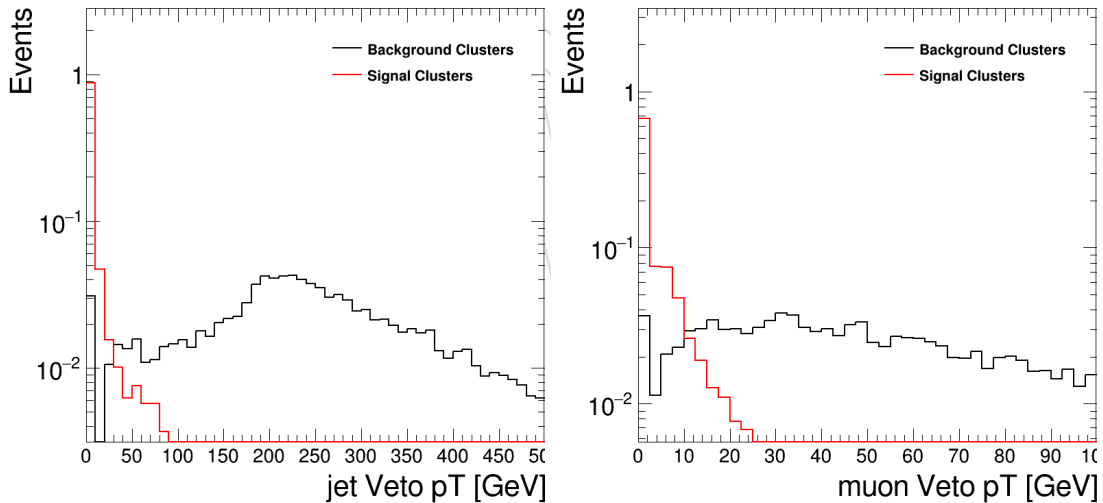


Figure 13: The distribution of p_T of jets(Left) and muons(Right) that the signal and background clusters are matched to. Signal consists of signal models of all available mass/ $c\tau$ points and background are clusters from WJets. Signal clusters pass the preselections, including the event-level cuts and the requirement that the matched LLP decays in CSC. Both signal and background clusters are required to be in-time: $-5 < t_{cluster} < 12.5$ ns. The exact definition of the timing cut is explained in the following paragraph. The background shape of the left plot has a peak at around 200 GeV because the background clusters are produced by punchthrough of the jets recoiling against the W boson that has p_T of around 200 GeV due to the 200 GeV MET requirement.

418 Out of time pileup contributes significantly to the background, and therefore the timestamp of
 419 the CSC cluster hits play an important role in distinguishing signal from background. The time

420 of the cluster, $t_{cluster}$, is defined as the average time of all recHits making up the cluster. The time
 421 for each recHit is calculated from the average of the wire digi and strip digi time that make up
 422 the recHits, where a positive tail pruning is applied to the wire digi time. This time definition
 423 is based on the CSC segment time definition, referenced in this code [42]. The distribution of
 424 the cluster time for is shown in Fig. 14, where we observe that the signal clusters are mostly
 425 in-time, but clusters from data show clear contribution of out-of-time pileup after all the vetos
 426 described above are applied. We define the signal region to be the region of $t_{cluster}$ between
 427 -5 and 12.5 ns. The signal does exhibit a longer right hand tail due to delays originating from
 428 slow moving LLPs. Therefore, we try to extend the time window on the right side as much as
 429 possible before allowing clusters from the next bunch crossing in.

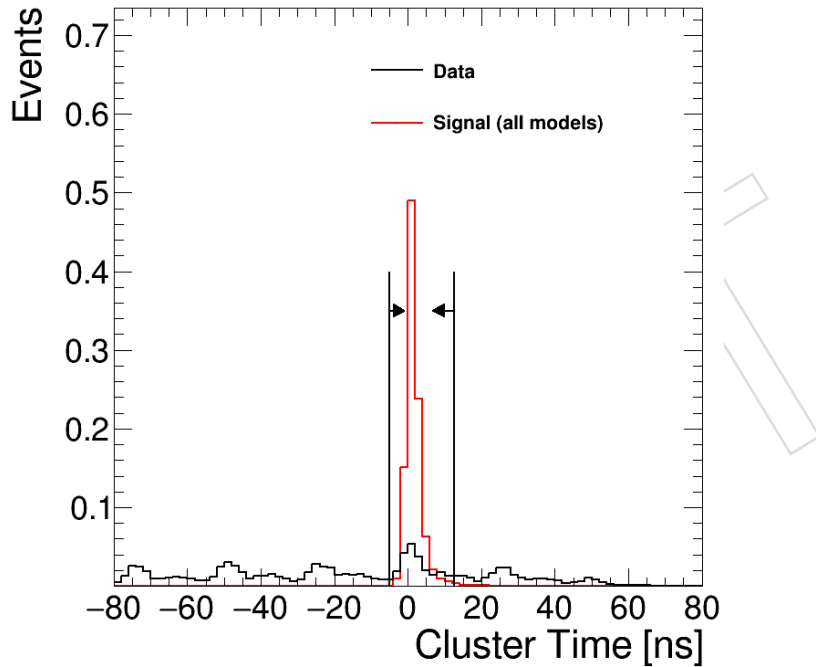


Figure 14: The signal and background distribution for cluster time is shown. Both signal and background clusters are required to pass the jet and muon veto.

430 To further suppress clusters from jet punchthrough and muon bremsstrahlung for muons that
 431 were not successfully reconstructed, we apply additional veto for high η cluster and several
 432 vetos to clusters that contain RecHits in several regions of the muon system that have minimal
 433 shielding in front, as shown in the colored, crossed-out regions in Fig. 15.

434 To optimize for these additional vetos, we define two background-enriched control regions: an
 435 in-time region, where clusters are required to be in-time ($-5 \text{ ns} < t_{cluster} < 12.5 \text{ ns}$), but with
 436 $N_{rechits} < 80$ and an early out of time region, where clusters are require to have time $< -12.5 \text{ ns}$.
 437

438 We first remove clusters that have any CSC RecHits in ME1/1 and ME1/2, the first two stations
 439 in the CSC system, as they have minimal shielding in front. The signal and background
 440 distributions of the number of Rechits in ME1/1 and ME1/2, after applying the jet and muon
 441 veto, is shown in Fig. 16, normalized in area. We observe that the veto has a signal efficiency of
 442 about 60% and a background efficiency of 5%, improving the signal to background ratio.

443 In addition, to account for the rare cases when ME1/2 is inefficient, clusters are also vetoed if

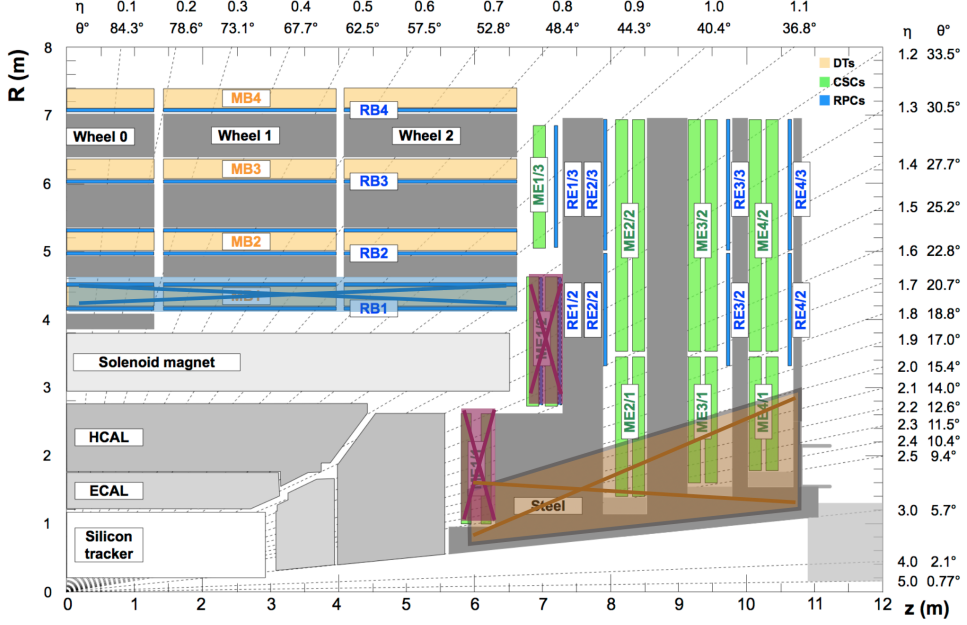


Figure 15: The detector geometry of the CMS muon system is shown. The colored crossed-out regions are the regions with minimal shieding that are being vetoed.

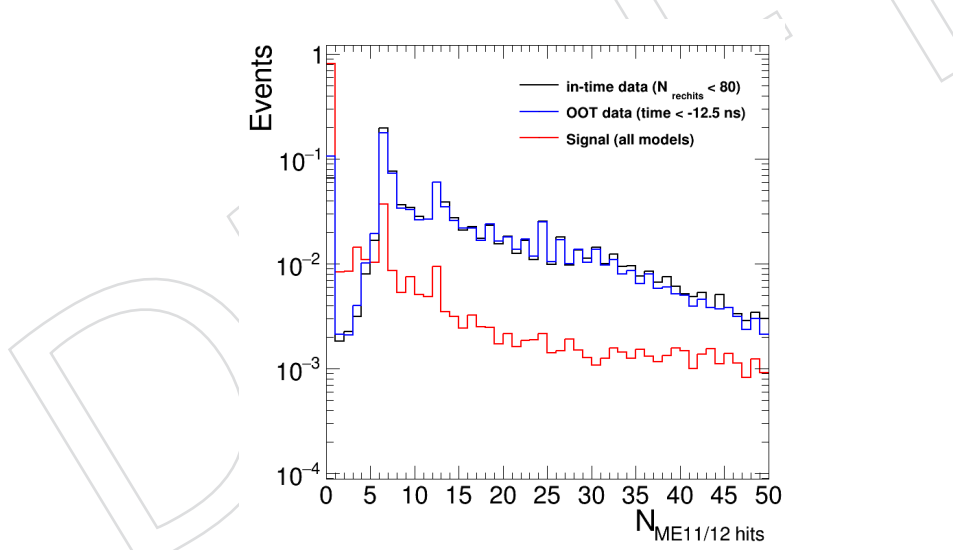


Figure 16: Distribution of the number of hits in chamber ME1/1 or ME1/2, for events that pass the jet/muon veto. Data in-time region is unblinded up to $N_{\text{rechits}} = 80$. Data OOT region has the same event and cluster selection as the in-time region, except the time requirement is changed to $t_{\text{cluster}} < -12.5 \text{ ns}$. Based on the distribution, we only select clusters with no hits in chamber ME1/1 or ME1/2.

they are matched to RPC hits in RE1/2, the RPC station right behind ME1/2. To suppress clusters caused by muon bremsstrahlung in the η region between 0.8 and 1.2, where the muons traverse the barrel DT stations and shower in ME1/3 or ME2/2, we veto clusters that are matched to DT segments in the first DT station, MB1, or clusters that are matched to the RPC hits in the first barrel RPC station, RB1. The signal distribution for the number of hits in RE1/2, RB1 and

449 segments in MB1 are shown in Fig. 17.

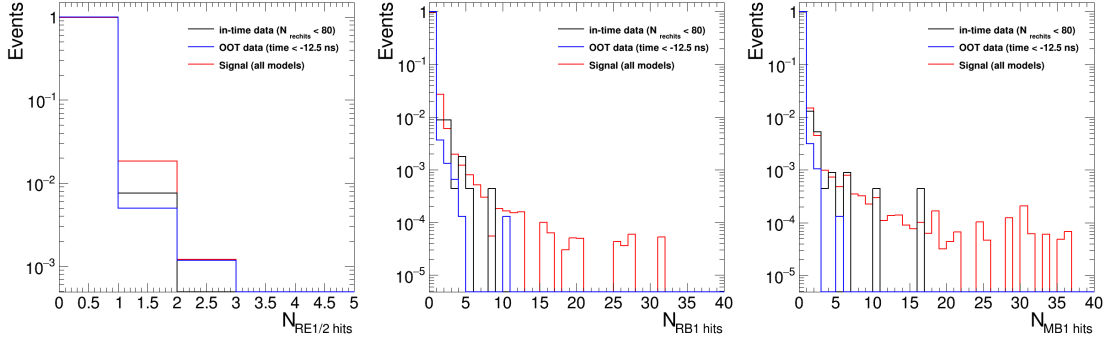


Figure 17: The signal and background distributions of the number of hits in RE1/2 (Left), the number of hits in RB1 (Middle), and the number of segments in MB1(Right) are shown. Clusters are required to pass the jet and muon veto and the ME11/12 vetos mentioned above.

450 Clusters with high η , ($|\eta| > 2$) are also removed explicitly, to account for cases when high
 451 η muons are not successfully reconstructed. The $|\eta|$ cut is determined by studying the muon
 452 bremsstrahlung that create cluster of CSC segments in 2016 W+Jets MC samples. To remove all
 453 the muon bremsstrahlung segment clusters, an η cut of 2.0 is applied. While this cut removes
 454 all the muon bremsstrahlung segment clusters, the signal efficiency is still high. The signal and
 455 background distribution of the cluster η distribution is shown in Fig. 18. All other cluster-level
 456 cuts and event selections are applied.
 457

458 Finally, to avoid pathological clusters that contain RecHits from multiple bunch crossings, clus-
 459 ter time spread is required to be less than 20 ns. The time spread is defined as $\sqrt{\frac{\sum(t_i - \bar{t})^2}{N}}$, where
 460 t_i is the strip digi time of the i-th RecHit, \bar{t} is the mean of strip digi time in the cluster, and N is
 461 the number of RecHits in the cluster. Only the strip digi time are used for time spread defini-
 462 tion, since the wire digi time are quantized in bins of 12.5 ns. This cut has a signal efficiency of
 463 96 – 99% on the signal samples. The shape of the signal time spread distribution is shown in
 464 Fig. 19, where all other cluster-level cuts and event selections are applied.

465 We select events with at least one reconstructed cluster ($N_{cluster} \geq 1$) passing all selections de-
 466 scribed above. Most signal events ($\geq 99\%$) contain only 1 cluster, while all background events
 467 contain exactly 1 cluster.

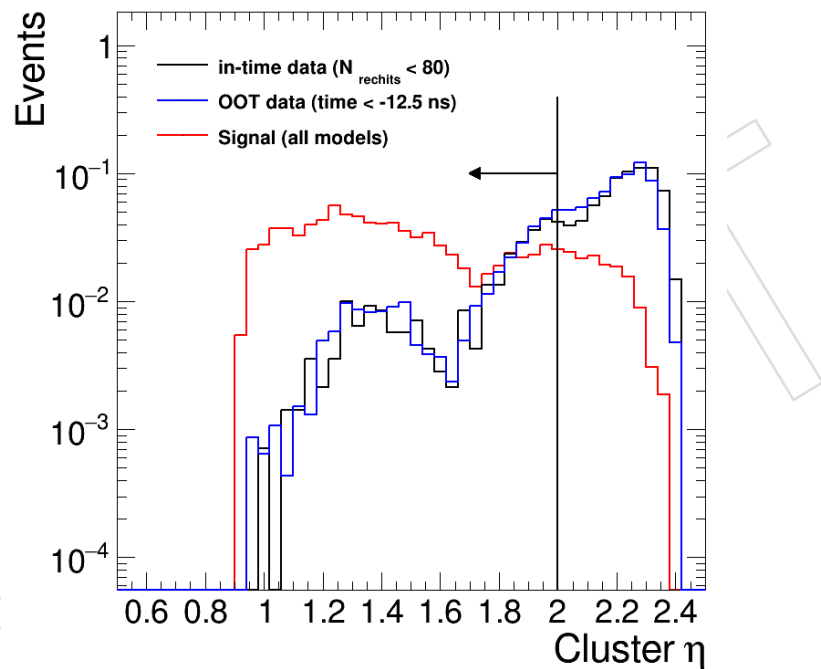


Figure 18: Distribution of the cluster η . Data in-time region is unblinded up to $N_{\text{rechits}} = 80$. Data OOT region has the same event and cluster selection as the in-time region, except the time requirement is changed to $t_{\text{cluster}} < -12.5 \text{ ns}$. Based on the distribution, we select clusters with $|\eta| < 2.0$.

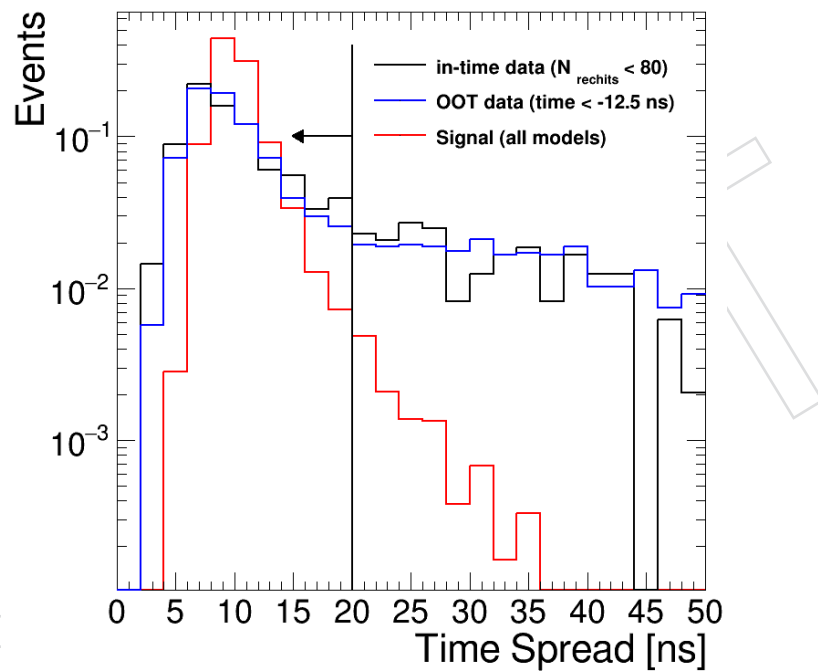


Figure 19: The signal and background distributions for cluster time spread is shown. Signal consists of clusters passing all other selections in the available mass/ τ points. Data in-time region is unblinded up to $N_{\text{rechits}} = 80$ with clusters passing all other selections. Data OOT region has the same event and cluster selection as the in-time region, except the time requirement is changed to $t_{\text{cluster}} < -12.5 \text{ ns}$.

468 5.1.1 Cluster Identification

469 A cluster-level identification selection is used to further discriminate the signal from back-
 470 ground using the difference in shape and location of the clusters. The set of cuts introduced
 471 in the previous sections mostly serve to kill background from the primary interaction, and the
 472 majority of the remaining background are due to pileup. The pileup background tends to oc-
 473 cur more often at larger values of η , tends to occur more often in stations closer to the primary
 474 interaction point, and tends to extend to less number of stations than the signal. Therefore we
 475 designed a cluster identification selection that makes use of those features to further enhance
 476 the signal to background ratio:

477

- 478 • **cluster η :** η position of the cluster, calculated by taking the average of the Rechit
 479 global positions in Cartesian coordinates and converting from Cartesian coordinates
 480 to the η position.
- 481 • **average station number:** This variable serves as a proxy for the Z position of the
 482 cluster. It is calculated by taking the average of the Rechits station number (if the
 483 station contains at least 10 Rechits), ranging from 1 to 4.
- 484 • **cluster $N_{station}$:** This variable characterizes the number of stations in which there
 485 are at least 10 Rechits from the cluster.

486 For the average station number and $N_{station}$ variables, a station is counted only if it contains
 487 at least 10 Rechits. This requirement ensures that we are counting stations with showers as
 488 opposed to single muon tracks, which would leave at most 6 Rechits per station, or noise.

489 As the dominant background remaining is particles from pileup, we use the early out-of-time
 490 (time < -12.5 ns) clusters in data as background to optimize the cluster identification criteria.
 491 Signal clusters are those that are matched to a gen-level LLP that decays in the CSC system from
 492 signal MC samples (all available mass/ $c\tau$ points). The clusters in both signal and background
 493 are also required to pass the list of vetos presented in previous sections. The distributions for
 494 signal and both in-time ($N_{rechits} < 80$) and OOT background of the 3 variables are shown in
 Fig. 20, although only the OOT data is used for optimization of the cut-based ID.

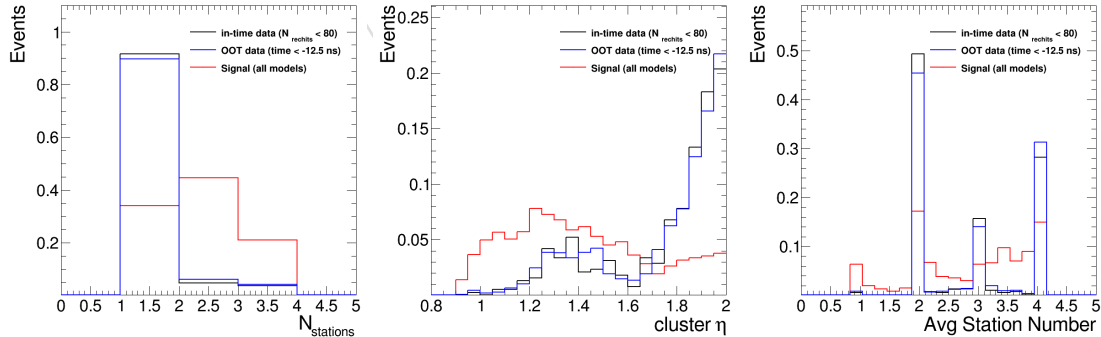


Figure 20: Signal and background distributions for the cluster-level variables used to construct the cut-based ID. As shown in the figures, data from the in-time and OOT region show similar shape as expected if both are due to pileup background clusters. The pileup background clusters generally occupy 1 station and have relatively high η , while the signal-like clusters are more likely to punchthrough the iron material in between stations and have smaller η positions.

495

496 This cut-based cluster ID selection can be viewed as a series of progressively tighter cuts on η as

497 the number of stations and average station is decreased. The requirements chosen is obtained
 498 from a rough optimization procedure where we tried to maximize the signal efficiency for each
 499 average station, while maintaining a negligible level of background from background processes
 500 that pose problems for the ABCD estimation method. Those problematic backgrounds tend to
 501 occur at larger η . The resulting ID selection is summarized below.

502 If the cluster is composed of more than one station, then the absolute value of η of the cluster is
 503 required to be smaller than 1.9. The signal and background η distributions for clusters of more
 504 than one station are shown in Fig. 21. If the cluster contains only one station, and the average
 505 station number is 4, then $|\eta| < 1.8$ is required. If the cluster contains only one station, and the
 506 average station number is 3 or 2, then $|\eta| < 1.6$ is required. And if the cluster contains only one
 507 station, and the average station number is 1, then no explicit η requirement is made, but there
 508 is an implicit η requirement (less than about 1.1) due to the fact that we veto hits in ME1/1
 509 and ME1/2. The 2D distributions of η and average station number for signal and background
 510 clusters with just one station are shown in Fig. 22. Table 9 summarizes these the cuts. The
 511 cut-based ID yields a signal efficiency of 82% and a background rejection of 3.

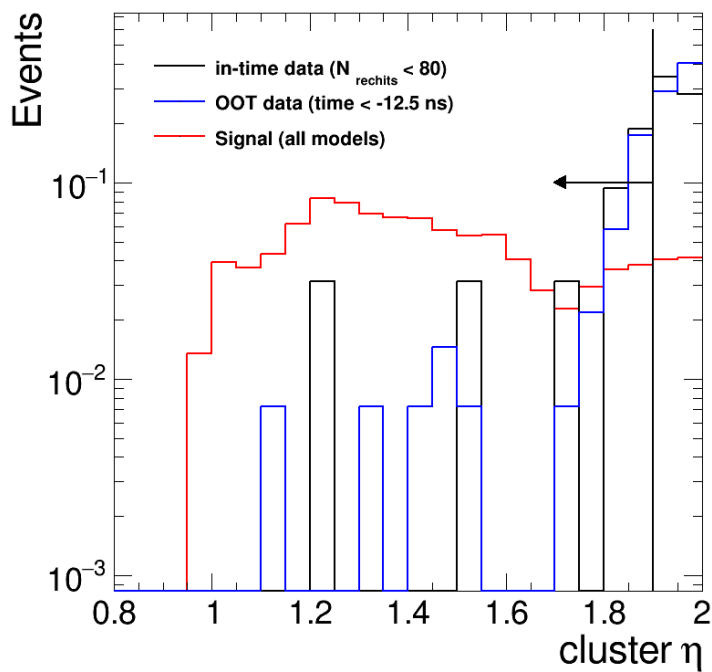


Figure 21: Signal and data distributions of cluster η when $N_{stations} > 1$. Data in-time region is unblinded up to $N_{rechits} = 80$. Data OOT region has the same event and cluster selection as the in-time region, except the time requirement is changed to $t_{cluster} < -12.5\text{ ns}$. Based on the distribution, we select clusters with $|\eta| < 1.9$.

512 An alternative BDT-based cluster ID was developed and the details are described in Appendix E.
 513 In the current analysis, we do not use the BDT-based cluster ID.

5.2 Cosmic Muon Shower Events

515 One specific type of background is the cosmic muon shower events, when multiple cosmic
 516 muons pass through the detector and create showers in the CSC and DT. An event display of
 517 a cosmic muon shower event is shown in Fig. 23. In this particular event, there are more than
 518 10,000 CSC Rechits, distributed across several bunch crossings. We select a control sample of

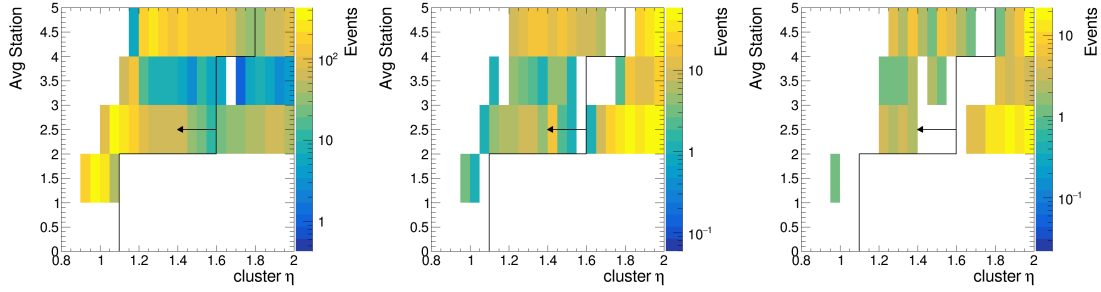


Figure 22: 2D distributions of cluster η and the average station number for signal of all models (Left), OOT data (Middle), in-time data(Right) when $N_{stations} = 1$. Similar to all the other data plots, data in-time region is unblinded up to $N_{rechits} = 80$ and data OOT region has the same event and cluster selection as the in-time region, except the time requirement is changed to $t_{cluster} < -12.5\text{ns}$. Based on the distribution, we select clusters with $|\eta| < 1.9$.

Table 9: Summary of the cut-based cluster ID selection. The implicit cut for the case with NStation = 1 and Avg Station = 1 is due to the ME1/1 and ME1/2 rechit veto.

NStation and Avg Station	$ \eta $ requirement
NStation > 1	$ \eta < 1.9$
NStation = 1 and Avg Station = 4	$ \eta < 1.8$
NStation = 1 and Avg Station = 3	$ \eta < 1.6$
NStation = 1 and Avg Station = 2	$ \eta < 1.6$
NStation = 1 and Avg Station = 1	implicit $ \eta < 1.1$

such events with more than 2000 early (time < -25 ns) CSC rechits in an early OOT cluster, as shown in Fig. 24. We observe that these events contain many rechits distributed over many different parts of the detector. To quantify this effect we define a quantity called “rings” as follows. The CSC detector is composed of four stations in each of the two endcaps : ME ± 1 , ME ± 2 , ME ± 3 , ME ± 4). Station ME ± 1 contains three rings (ME $\pm 1/1$, ME $\pm 1/2$, ME $\pm 1/3$), while the remaining three stations contain two rings each (ME $\pm 2/1$, ME $\pm 2/2$, ME $\pm 3/1$, ME $\pm 3/2$, ME $\pm 4/1$, ME $\pm 4/2$). There are a total of 18 CSC rings. The DT detector is composed of five wheels : MB0, MB ± 1 , MB ± 2 . Each wheel has four different layers. We define a DT ring to be a particular layer in a particular wheel. There are a total of 20 DT rings. We count how many CSC and DT rings with at least 50 rechits there are in an event. This is plotted in Fig. 25, for the control sample of cosmic muon shower events compared to simulated signal events. We observe that the cosmic muon shower events occupy a large number of DT and CSC rings, while signal events from LLP decays are localized in a few rings. Therefore, we veto events that have more than 10 rings with at least 50 Rechits from our signal region. This requirement has near 100% efficiency for the signal.

To validate the signal efficiency in data, we select events in the muon bremsstrahlung control region containing an isolated muon track has been matched to a cluster in the CSC detector. Such events are a close analogue to the signal events and are used to measure the efficiency of the cosmic muon shower veto. If high levels of electronic noise were present, we may observe a large number of rings with many rechits, resulting in signal efficiency loss. The distribution of the number of CSC and DT rings is shown in Fig. 25, and we confirm that the efficiency of the veto is 100%.

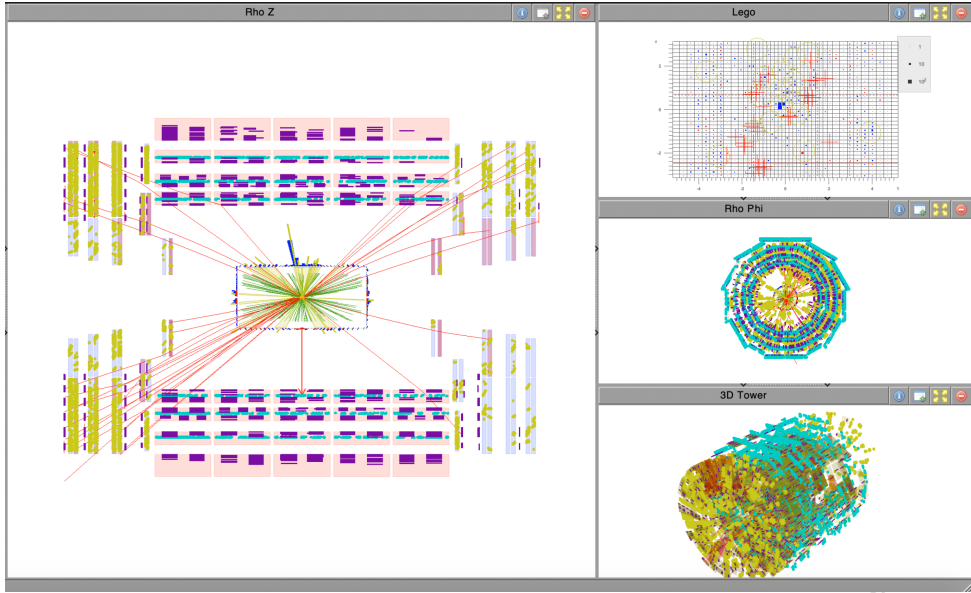


Figure 23: Event display of a cosmic muon shower event that creates showers with a large number of CSC, DT, and RPC Rechits. The red lines in the left figure are reconstructed muons. The yellow dots are CSC Rechits; purple lines are RPC Rechits; Cyan lines are DT Rechits.

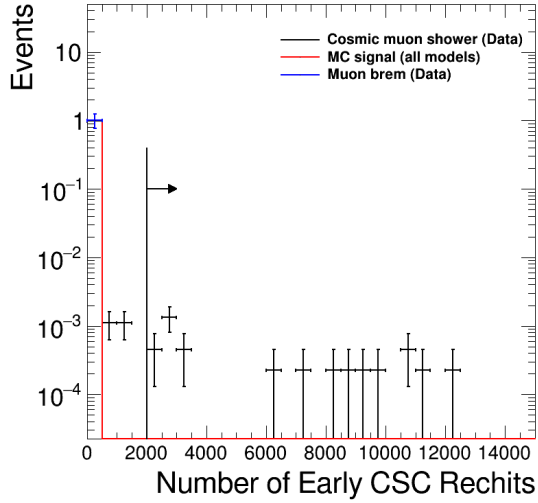


Figure 24: The number of early OOT CSC Rechits. This distribution is used to select a sample enriched in cosmic muon shower events.

541 5.3 Signal Region Optimization

542 In addition to the variables mentioned above, two more discriminators are used to define the
 543 signal region, namely $\Delta\phi(\text{cluster}, \text{MET})$ and N_{rechits} . These two variables are used to define
 544 the signal-enhanced regions used for the ABCD background estimation method that will be
 545 described in further detail in Section 6.1.

546 We will show some motivation for the nominal bin boundary choices for the ABCD method.
 547 The distributions for the $\Delta\phi(\text{cluster}, \text{MET})$ and N_{rechits} are shown in Figure 26 and 27 for signal
 548 and background control regions. The $\Delta\phi(\text{cluster}, \text{MET})$ is selected to have 90% signal

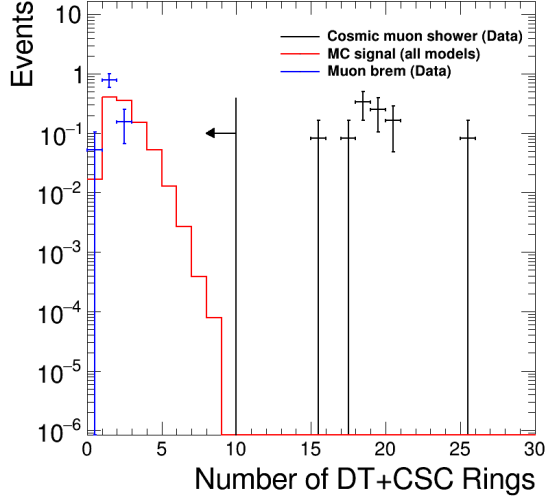


Figure 25: The number of DT and CSC rings that have at least 50 RecHits is shown for the cosmic muon shower control sample, the signal simulation sample, and the muon bremsstrahlung control sample. The histograms have been normalized to unit area. This variable is used to identify the cosmic muon shower background events.

efficiency, while the cut for N_{rechits} is chosen to maximize the expected limit.

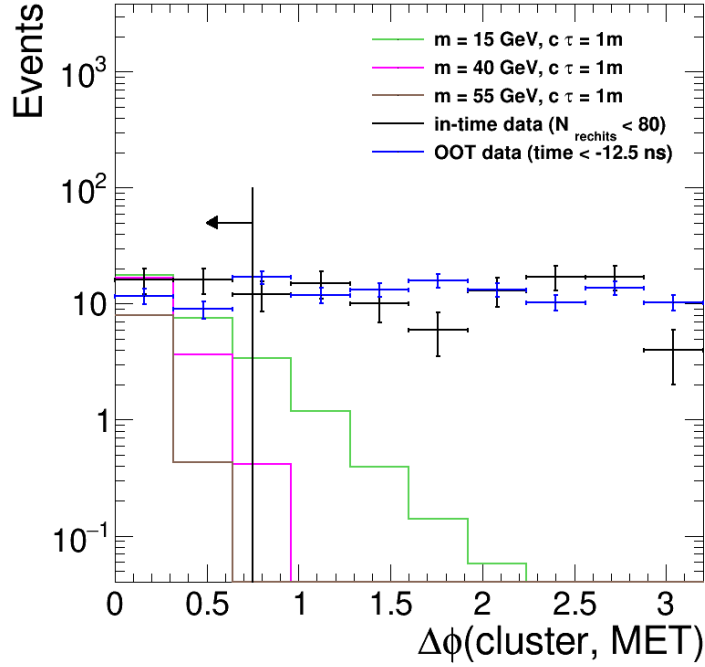


Figure 26: The distribution of $\Delta\phi(\text{cluster}, \text{MET})$ for signal and background is shown. The branching ratio for signal is 1%. Data in-time region is unblinded up to $N_{\text{rechits}} = 80$. Data OOT region has the same event and cluster selection as the in-time region, except the time requirement is changed to $t_{\text{cluster}} < -12.5\text{ ns}$ and is scaled to the number of events in in-time region.

We make a projection for the number of background events in the signal-enhanced bin (D)

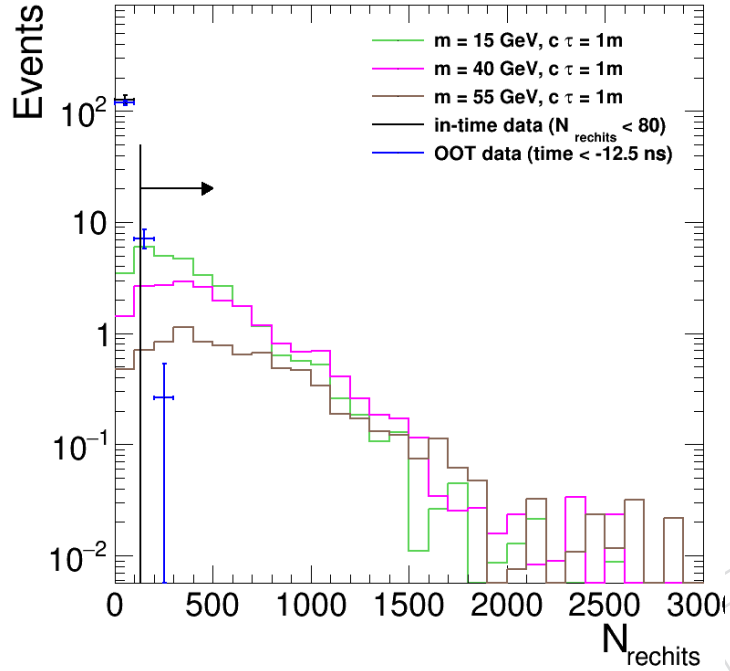


Figure 27: The distribution of N_{rechits} for signal and background is shown. The branching ratio for signal is 1%. Data in-time region is unblinded up to $N_{\text{rechits}} = 80$. Data OOT region has the same event and cluster selection as the in-time region, except the time requirement is changed to $t_{\text{cluster}} < -12.5 \text{ ns}$ and is scaled to the number of events in in-time region.

by extrapolating the background prediction from events in the out-of-time validation region that have clusters passing the cluster identification requirements. This extrapolation is done in order to (a) remain fully blinded in the signal region during the optimization step, and (b) to improve the statistical uncertainty of the background yield prediction as using the signal region ABCD method would be subject to large statistical fluctuations due to limited data sample size. The extrapolation is done using the ratio between in-time and OOT events derived from events failing the clusterID, using the following equations:

$$N_{\text{intimepass}} = \frac{N_{\text{OOTpass}} \times N_{\text{intimefail}}}{N_{\text{OOTfail}}} \quad (3)$$

where $N_{\text{intimepass}}$ is the number of background events estimated for the signal region, $N_{\text{intimefail}}$ is the number of background events in the in-time region passing the cluster ID, N_{OOTpass} and N_{OOTfail} are the number of background events in the OOT region passing and failing the cluster ID, respectively. Several different values of N_{rechits} cuts are used for signals with different lifetimes and the expected limit is calculated and shown in Fig. 28. We observe that the expected limit improves as the N_{rechits} cut is increased up to around 130. Beyond 130, the expected limit reaches a plateau for all signal lifetimes. Therefore we choose to place the cut boundary at $N_{\text{rechits}} > 130$ for all the signal models.

In summary, the signal efficiency of all the selections applied for the gluon-fusion production mode and 4 b decay mode, including samples from all 3 years, for LLP mass 15, 40, and 55 GeV are shown in Table 10, 11, and 12, respectively. The efficiencies for 4d and 4 τ decay mode are shown in Appendix D. We have also checked that the inclusive signal efficiency is similar for different run conditions on one representative signal model (ggH production mode for LLP

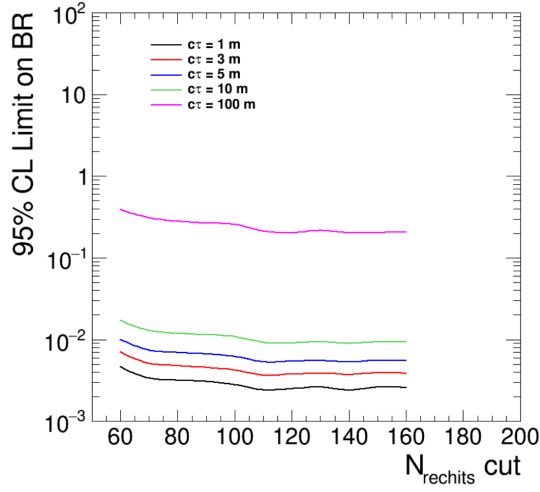


Figure 28: The expected limit at different N_{rechits} cut for signal with different LLP lifetimes.

- 563 with mass of 40 GeV and decaying to 2 b quarks), as shown in Appendix B.2. The efficiency of
 564 data for the full Run2 dataset is summarized in Table 13. The efficiency of the cuts are similar
 565 across different years, and the cut flow tables for individual years are shown in Appendix B.3.
 566 The signal efficiency of the clustering efficiency and all the cluster-level cuts, except for the two
 567 selections that define the boundary of the ABCD plane($\Delta\phi(\text{cluster}, \text{MET})$ and N_{rechits}), with
 568 respect to the LLP decay position in the radial and Z direction respectively is shown in Fig. 29.
 569 The 2D signal efficiency maps with respect to the LLP decay position are shown in Fig. 30. This
 570 efficiency is independent of the detector condition, as demonstrated in Fig. 65 in Section B.
 571 The signal efficiency of the cut $N_{\text{rechits}} \geq 130$ with respect to clusters passing all the other
 572 cluster-level cuts, except for $\Delta\phi(\text{cluster}, \text{MET}) < 0.75$ is shown in Fig. 31. This efficiency is
 573 independent of the detector condition, as demonstrated in Fig. 66 in Section B.

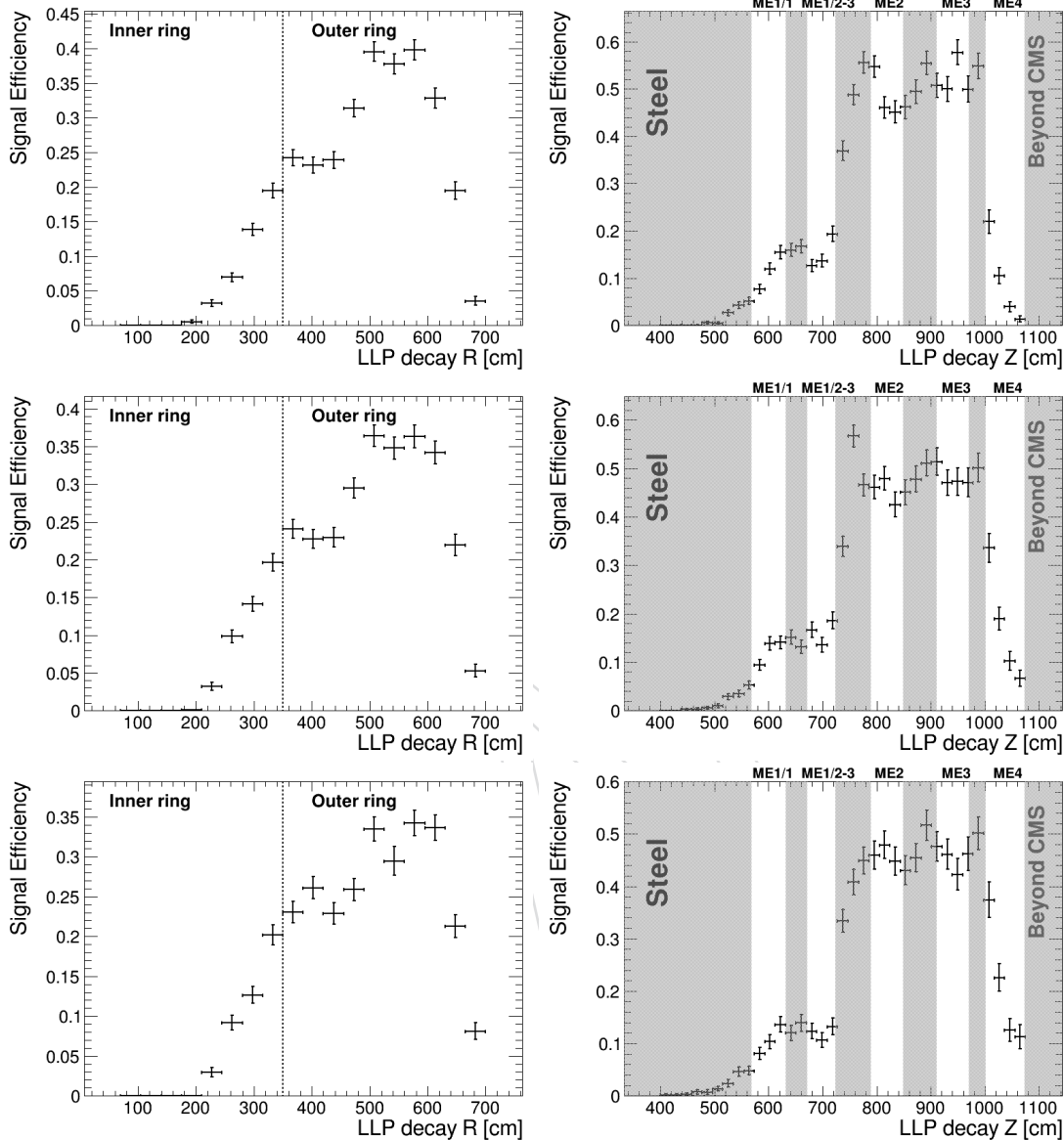


Figure 29: The signal efficiency of the selections with respect to the LLP decay position in the radial direction (Left) and the LLP decay position in the Z direction (Right) is shown. The nominator clusters are required to pass all cluster-level cuts, except for $\Delta\phi(\text{cluster}, \text{MET})$ and N_{rechits} , while the denominator consists of any LLP that decays in the CSC volume. Similar trend is seen in different LLP masses of 15 (Top), 40 (Middle), and 55 GeV (Bottom). The signal efficiency is the highest in the outer ring (low η region) and when the LLP decays between station 2 and station 4. The signal sample for each LLP mass includes the sum of all available lifetimes.

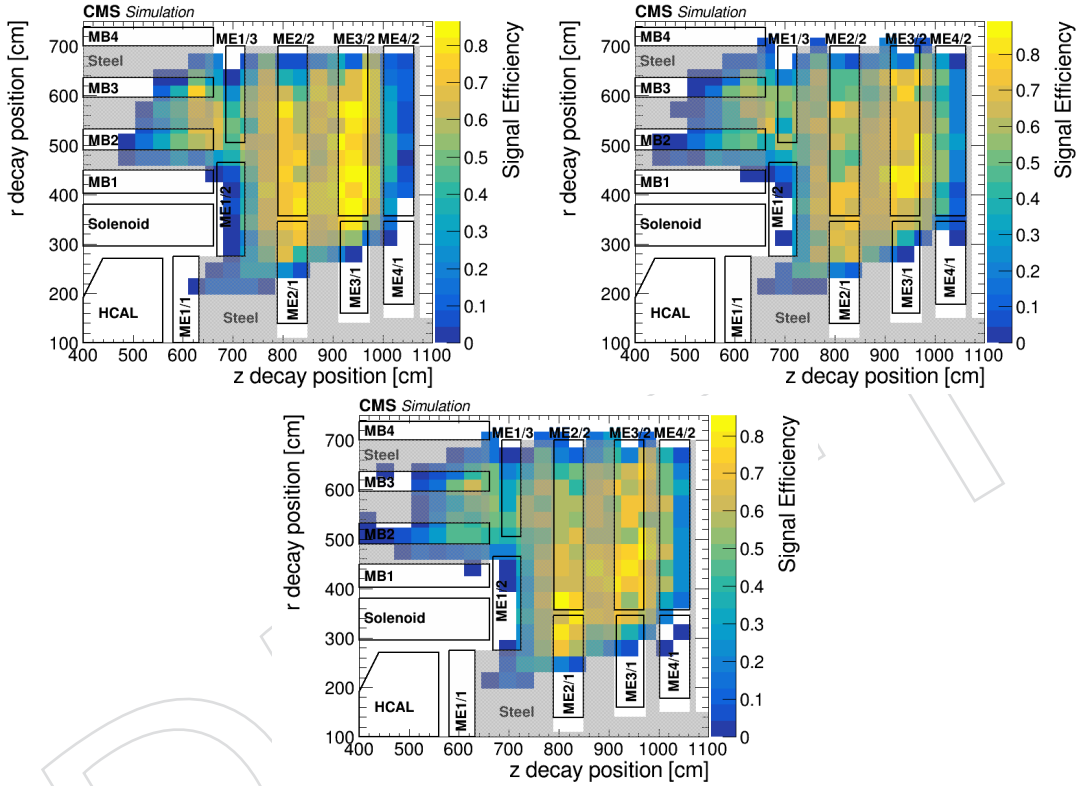


Figure 30: The 2D signal efficiency of the selections with respect to the LLP decay position in the radial direction and the Z direction is shown. The nominator clusters are required to pass all cluster-level cuts, except for $\Delta\phi(\text{cluster}, \text{MET})$ and N_{rechits} , while the denominator consists of any LLP that decays in the CSC volume. Similar trend is seen in different LLP masses of 15 (Top Left), 40 (Top Right), and 55 GeV (Bottom). The signal sample for each LLP mass includes the sum of all available lifetimes.

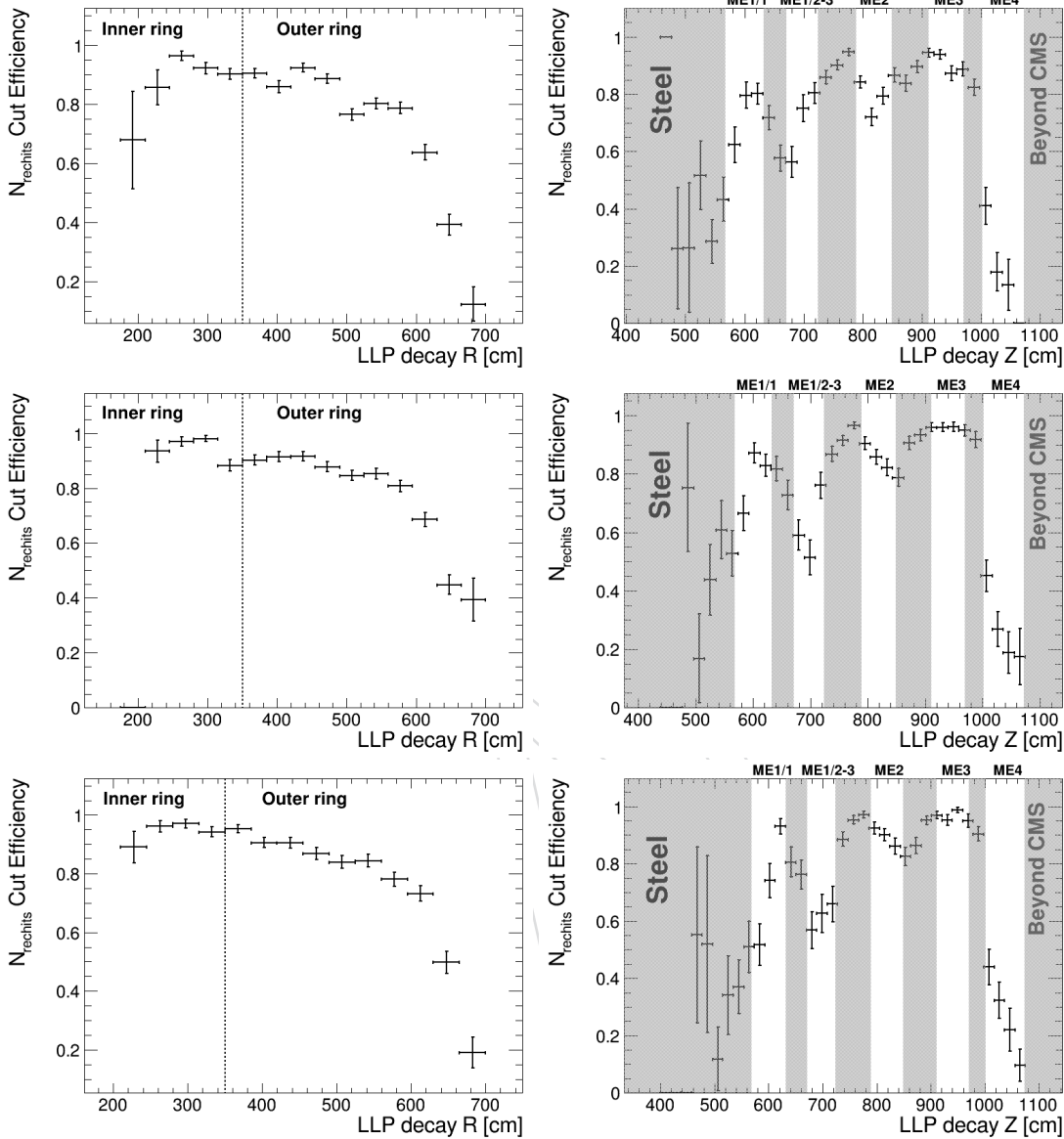


Figure 31: The signal efficiency of the cut $N_{\text{rechits}} \geq 130$ with respect to the LLP decay position in the radial direction (Left) and the LLP decay position in the Z direction (Right) is shown. The denominator clusters are required to pass all cluster-level cuts, except for $\Delta\phi(\text{cluster}, \text{MET})$ and N_{rechits} , satisfying the same set of requirements as the nominator clusters in Fig. 29. Nominator clusters are required to pass the $N_{\text{rechits}} \geq 130$ cut, in addition to the denominator requirements. Similar trend is seen in different LLP masses of 15 (Top), 40 (Middle), and 55 GeV (Bottom). The signal efficiency is low when the LLP decays near the edge of the detector, beyond 6 meters in radius or more than 10 meters in Z. The signal sample for each LLP mass includes the sum of all available lifetimes.

Table 10: Signal Efficiency(%) of each cut for LLP mass 15 GeV, decaying to 2 b quarks. (Cumulative Efficiency for all cuts applied after Trigger and MET cut are calculated with respect to events in acceptance and pass the MET and trigger cut and cut efficiency is calculated with respect to the previous cut. Acceptance is defined as when at least one LLP decays inside CSC.)

Selection	$c\tau = 0.1m$		$c\tau = 1m$		$c\tau = 10m$		$c\tau = 100m$	
	cut eff	cumulative eff	cut eff	cumulative eff	cut eff	cumulative eff	cut eff	cumulative eff
Acceptance	2.684	2.684	27.538	27.538	8.999	8.999	1.080	1.080
Trigger and MET cut	2.545	0.068	0.835	0.230	0.924	0.083	1.004	0.011
MET filters	97.13	97.13	98.28	98.28	99.31	99.31	99.26	99.26
$N_{lepton} = 0$	99.45	96.59	99.54	97.82	99.69	99.00	99.91	99.16
$N_{jet} \geq 1$	96.37	93.09	94.84	92.77	95.02	94.07	94.31	93.52
$N_{CSC+DT \text{ rings}} \leq 10$	100.00	93.09	100.00	92.77	100.00	94.07	100.00	93.52
$N_{cluster} \geq 1$	81.83	76.17	63.04	58.48	52.56	49.44	51.69	48.34
muon veto	92.66	70.58	93.56	54.71	94.22	46.58	95.52	46.17
jet veto	85.88	60.62	87.41	47.82	86.58	40.33	88.03	40.65
Time cut	99.79	60.49	99.76	47.71	97.78	39.44	95.85	38.96
ME1/1 veto	75.36	45.58	86.03	41.04	88.55	34.92	88.41	34.44
ME1/2 veto	62.91	28.68	72.18	29.63	73.41	25.64	72.29	24.90
RE1/2 veto	98.06	28.12	97.80	28.98	97.66	25.04	98.84	24.61
MB1 veto	95.36	26.81	95.67	27.72	96.61	24.19	98.37	24.21
RB1 veto	97.55	26.16	97.31	26.98	96.68	23.38	96.93	23.47
η cut	76.36	19.97	87.87	23.70	90.28	21.11	87.28	20.48
time spread cut	98.98	19.77	98.81	23.42	99.02	20.90	98.68	20.21
cut-based ID	84.46	16.70	91.87	21.52	89.94	18.80	91.86	18.57
$\Delta\phi(\text{cluster, MET})$	100.00	16.70	88.59	19.06	68.70	12.92	68.54	12.72
$N_{rechits}$ cut	93.06	15.54	81.99	15.63	79.46	10.26	71.09	9.05

Table 11: Signal Efficiency(%) of each cut for LLP mass 40 GeV, decaying to 2 b quarks. (Cumulative Efficiency for all cuts applied after Trigger and MET cut are calculated with respect to events in acceptance and pass the MET and trigger cut and cut efficiency is calculated with respect to the previous cut. Acceptance is defined as when at least one LLP decays inside CSC.)

Selection	$c\tau = 0.1m$		$c\tau = 1m$		$c\tau = 10m$		$c\tau = 100m$	
	cut eff	cumulative eff	cut eff	cumulative eff	cut eff	cumulative eff	cut eff	cumulative eff
Acceptance	0.088	0.088	17.101	17.101	20.328	20.328	3.322	3.322
Trigger and MET cut	8.249	0.007	1.011	0.173	0.716	0.146	0.646	0.021
MET filters	97.75	97.75	96.86	96.86	99.23	99.23	99.46	99.46
$N_{lepton} = 0$	99.75	97.50	99.52	96.40	99.77	99.00	99.64	99.10
$N_{jet} \geq 1$	97.51	95.08	95.58	92.13	94.66	93.71	94.19	93.34
$N_{CSC+DT \text{ rings}} \leq 10$	100.00	95.08	100.00	92.13	100.00	93.71	100.00	93.34
$N_{cluster} \geq 1$	91.16	86.67	73.55	67.76	61.90	58.01	57.75	53.91
muon veto	95.29	82.59	94.03	63.72	94.28	54.69	94.57	50.98
jet veto	59.23	48.92	82.75	52.73	88.17	48.23	87.86	44.79
Time cut	100.00	48.92	99.83	52.64	96.69	46.63	92.55	41.45
ME1/1 veto	46.65	22.82	81.72	43.01	87.90	40.99	85.73	35.54
ME1/2 veto	66.95	15.28	69.34	29.83	71.49	29.30	71.51	25.41
RE1/2 veto	100.00	15.28	97.16	28.98	98.20	28.78	98.96	25.15
MB1 veto	97.88	14.95	94.39	27.35	96.43	27.75	96.58	24.29
RB1 veto	100.00	14.95	96.21	26.32	97.15	26.96	96.45	23.43
η cut	41.11	6.15	83.13	21.88	89.84	24.22	90.76	21.26
time spread cut	96.32	5.92	99.00	21.66	99.11	24.00	97.29	20.69
cut-based ID	68.32	4.05	89.57	19.40	92.64	22.24	88.12	18.23
$\Delta\phi(\text{cluster, MET})$	100.00	4.05	99.40	19.28	96.25	21.40	95.88	17.48
$N_{rechits}$ cut	95.45	3.86	87.87	16.94	79.81	17.08	79.44	13.88

Table 12: Signal Efficiency(%) of each cut for LLP mass 55 GeV, decaying to 2 b quarks. $c\tau = 0.1$ m is not shown for 55 GeV, because the acceptance is on the order of 10^{-5} , so there are no events left after all selections are applied. (Cumulative Efficiency for all cuts applied after Trigger and MET cut are calculated with respect to events in acceptance and pass the MET and trigger cut and cut efficiency is calculated with respect to the previous cut. Acceptance is defined as when at least one LLP decays inside CSC.)

Selection	$c\tau = 1m$		$c\tau = 10m$		$c\tau = 100m$	
	cut eff	cumulative eff	cut eff	cumulative eff	cut eff	cumulative eff
Acceptance	8.383	8.383	23.910	23.910	5.288	5.288
Trigger and MET cut	1.472	0.123	0.649	0.155	0.444	0.023
MET filters	95.46	95.46	99.35	99.35	99.61	99.61
$N_{lepton} = 0$	99.46	94.94	99.71	99.06	99.82	99.44
$N_{jet} \geq 1$	96.13	91.27	94.61	93.72	93.45	92.93
$N_{CSC+DT \text{ rings}} \leq 10$	100.00	91.27	100.00	93.72	100.00	92.93
$N_{cluster} \geq 1$	78.23	71.40	66.64	62.45	65.26	60.64
muon veto	91.44	65.29	93.39	58.32	93.41	56.64
jet veto	67.93	44.35	87.22	50.87	89.35	50.61
Time cut	99.71	44.22	99.51	50.62	99.10	50.16
ME1/1 veto	73.19	32.37	87.74	44.41	90.29	45.29
ME1/2 veto	64.45	20.86	71.88	31.93	71.17	32.23
RE1/2 veto	98.07	20.46	98.26	31.37	98.34	31.69
MB1 veto	95.71	19.58	95.65	30.01	96.90	30.71
RB1 veto	97.63	19.12	97.31	29.20	97.81	30.04
η cut	68.27	13.05	91.24	26.64	92.02	27.64
time spread cut	98.63	12.87	98.89	26.34	98.95	27.35
cut-based ID	82.20	10.58	92.26	24.31	94.68	25.90
$\Delta\phi(\text{cluster}, \text{MET})$	99.84	10.56	100.00	24.31	100.00	25.90
$N_{rechits}$ cut	90.57	9.57	82.01	19.93	77.00	19.94

Table 13: Efficiency(%) of each cut for data.

Selection	cut eff	cumulative eff	Number of events
MET filters	92.62	92.62	13086543
$N_{lepton} = 0$	91.37	84.63	11957552
$N_{jet} \geq 1$	80.79	68.37	9660272
$N_{\text{CSC+DT rings}} \leq 10$	100.00	68.37	9660227
$N_{cluster} \geq 1$	8.01	5.48	773788
muon veto	61.68	3.38	477250
jet veto	47.26	1.60	225542
Time cut	26.57	0.42	59918
ME1/1 veto	12.02	0.051	7201
ME1/2 veto	45.69	0.023	3290
RE1/2 veto	99.24	0.023	3265
MB1 veto	98.13	0.023	3204
RB1 veto	99.69	0.023	3194
η cut	21.10	0.005	674
time spread cut	74.04	0.004	499
cut-based ID	29.86	0.001	149
$\Delta\phi(\text{cluster}, \text{MET})$	33.56	0.0004	50
$N_{rechits}$ cut	6.00	0.00002	3

574 6 Background Estimation

575 This section describes the data-driven background estimation and signal prediction method
 576 used in this analysis.

577 Using clusters composed of CSC segments reconstructed in the Summer 16 MC samples, we
 578 studied the dominant source of background processes that produce signal-like clusters. Signal-
 579 like clusters in the background simulation samples that passed the jet veto and muon veto
 580 requirements, were almost entirely not matched to any generator-level particles or partons. The
 581 only way that can happen is if the background cluster is produced by long-lived single particles
 582 from pileup such as K_L or neutrons. The time distribution of the clusters also supported this
 583 explanation as the number of clusters from the in-time bunch crossing matched the number of
 584 clusters from the out-of-time bunch crossings, which are a pure pileup sample.

585 Clusters produced by K_L or neutrons resulting from jet fragmentation are highly suppressed
 586 by the jet veto, and contributes negligibly to the signal region as shown by the shape of the
 587 $\Delta\phi(\text{cluster}, \text{MET})$ distribution. Events in the sample with $\text{MET} > 200 \text{ GeV}$ are predominantly
 588 from the W+Jets and top quark pair production, where jets recoil against the neutrino from a W
 589 boson decay which produces the MET. A cluster that results from long-lived particles produced
 590 by the fragmentation of the recoiling jet will either point to the MET, if the MET comes from
 591 the mis-reconstruction of the jet energy, or point opposite to the MET, if the MET comes from
 592 the neutrinos. The $\Delta\phi(\text{cluster}, \text{MET})$ distribution of clusters produced from punchthrough jets
 593 in data, selected by inverting the jet veto is shown in Fig. 32, where the distribution clearly
 594 peaks at 0 and π . In the signal region distribution of $\Delta\phi(\text{cluster}, \text{MET})$ in Figure 26, we see no
 595 evidence of such behavior, and instead we observe a flat distribution indicating that the MET
 596 direction and the cluster direction is independent.

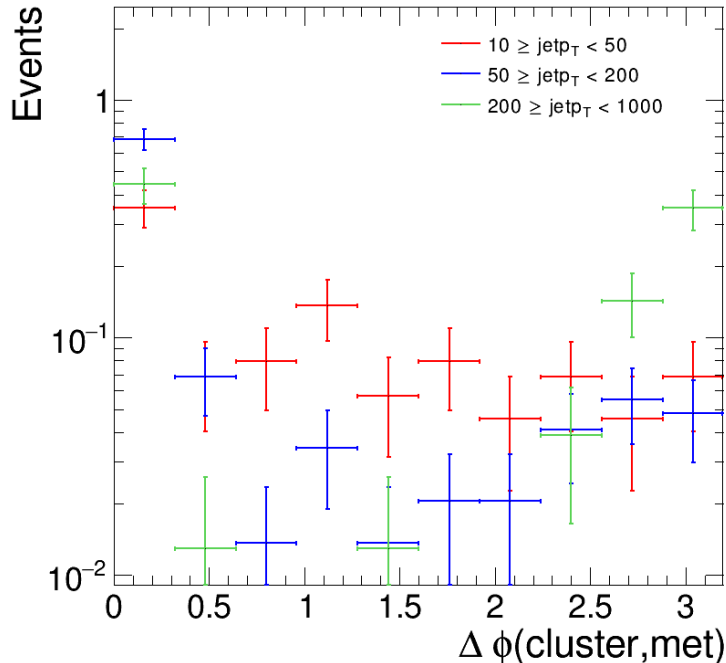


Figure 32: The normalized $\Delta\phi(\text{cluster}, \text{MET})$ distributions of events that fail the jet veto (cluster is matched to a jet with $p_T > 10 \text{ GeV}$). The event is required to pass all signal selection cuts, except for the two variables that are used in the ABCD plane: $\Delta\phi(\text{cluster}, \text{MET})$ and N_{rechits} .

597 Beam halo muons travelling through and shower in the CSC, could create CSC clusters. The
 598 beam halo-induced clusters are suppressed by the application of the beam halo filter. Futher-
 599 more, the beam halo muons are highly correlated with the MET direction. Beam halo particles
 600 travel through the detector approximately parallel to the beamline. They will produce recHits
 601 in the CSC system and also produce energy deposits in the calorimeter, creating additional
 602 activity in multiple subdetectors in the same ϕ direction. Therefore, the missing momentum
 603 would point to the opposite direction of the CSC cluster. A beam halo-enriched sample using
 604 data is obtained by inverting the beam halo filter. The cluster ϕ and $\Delta\phi(\text{cluster}, \text{MET})$ distribu-
 605 tion of events enriched in beam halo is shown in Fig. 33. The cluster ϕ of beam halo-induced
 606 clusters peak at 0 and $\pm\pi$. The distribution of $\Delta\phi(\text{cluster}, \text{MET})$ peaks at π , indicating that
 607 the MET and cluster are in opposite directions. These features in $\Delta\phi(\text{cluster}, \text{MET})$ are not ob-
 608 served in the signal region, as shown in Fig. 26, indicating that the beam halo background is
 609 negligible in the signal region.

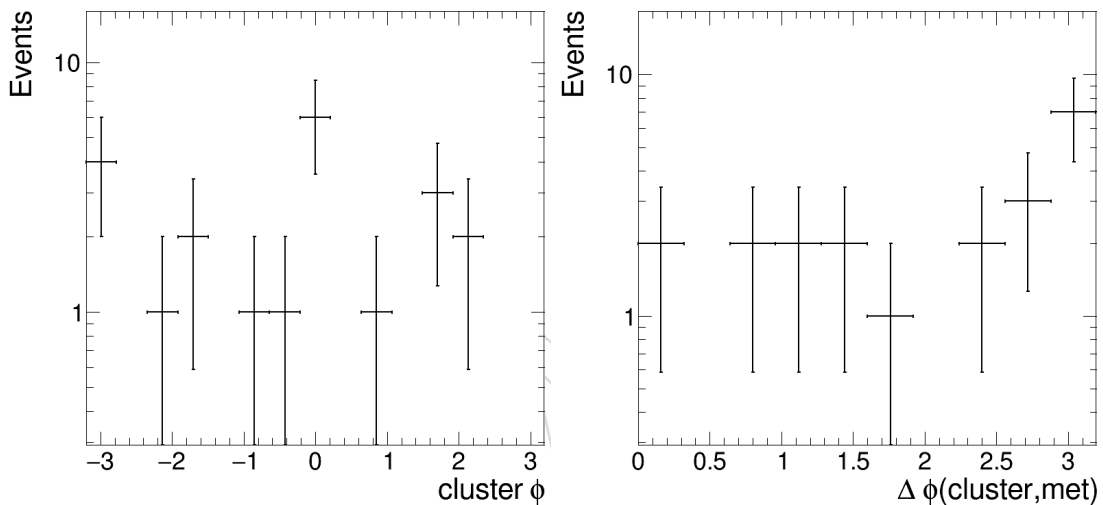


Figure 33: The cluster ϕ (Left) and $\Delta\phi(\text{cluster}, \text{MET})$ (Right) distributions of events failing the beam halo filter. In addition, the events are required to pass all signal selection cuts, except the two variables that are used in the ABCD plane: $\Delta\phi(\text{cluster}, \text{MET})$ and N_{rechits} .

610 For events passing the $\Delta\phi(\text{cluster}, \text{MET}) < 0.75$ requirement, a small fraction of background
 611 clusters are produced by muons undergoing bremsstrahlung in the material near or inside the
 612 CSC system. Such muons are produced by decays of W bosons which may fall within our signal
 613 region if the W boson has a large boost and results in a small angle between the neutrino that
 614 produces the MET and the CSC cluster resulting from the muon bremsstrahlung. These clusters
 615 are very efficiently rejected by the muon veto requirement but as $|\eta|$ increases above 2.0, the
 616 muon reconstruction and identification efficiency decreases and the rate for such backgrounds
 617 increase. After vetoing clusters with $|\eta|$ larger than 1.9, this background is suppressed to a
 618 negligible level, as demonstrated by the closure of the ABCD background prediction method
 619 applied to the validation regions defined in subsection 6.2.2 below. Furthermore, clusters pro-
 620 duced by muon bremsstrahlung is confined to one station only as the photon induced shower
 621 is unable to punch through into the second station. The cluster identification selection imposes
 622 tighter $|\eta|$ requirements for clusters with only one station as stated in Table 9, which even fur-
 623 ther suppresses this background.

624 After imposing the cluster identification criteria, based on the above observations, we expect
 625 the dominant background after the selections detailed in Section 5 to be clusters produced from

626 isolated K_L or neutrons from pileup interactions.

627 Cosmic muons that traverse the CSC detector would need to undergo a rare bremsstrahlung
 628 process in order to produce a cluster object passing the signal selection requirements. Further-
 629 more, the likelihood that such a cluster would produce sufficient MET to pass the MET trigger
 630 is highly suppressed as (1) the cosmic muon trajectory would need to be close to parallel to
 631 the beamline in order to traverse the calorimeters and the CSC detector, and (2) would need
 632 to undergo some additional bremsstrahlung to produce sufficient energy in the calorimeter for
 633 it to pass the $\text{MET} > 200 \text{ GeV}$ requirement. Therefore, any cosmic muon producing a cluster
 634 object would likely be uncorrelated with whatever collision process produced the MET. While
 635 we observe no evidence of cosmic muon events undergoing bremsstrahlung in the CSC detec-
 636 tor in the validation regions discussed in section 6.2, such background events will also exhibit
 637 a flat distribution in $\Delta\phi(\text{cluster}, \text{MET})$. Therefore, the background prediction from the ABCD
 638 background estimation method would include the contribution of such background processes.

639 6.1 Data-Driven Background Estimation Method

640 The ABCD method is used to estimate the number of background events in the signal region.
 641 The two variables used to construct the four ABCD bins are N_{rechits} and $\Delta\phi(\text{cluster}, \text{MET})$.

642 $\Delta\phi(\text{cluster}, \text{MET})$ is expected to peak at 0 for signal, since the both the cluster and the MET
 643 originate from the LLP. The cluster is produced from the LLP decay, while the MET is pro-
 644 duced by the LLP as it is undetected by the tracker and calorimeter systems. For background,
 645 $\Delta\phi(\text{cluster}, \text{MET})$ is expected to be flat because the cluster is expected to originate from pileup
 646 collisions, while the MET originates from the triggered primary interaction. The distributions
 647 of $\Delta\phi(\text{cluster}, \text{MET})$ for signal and background control regions are shown in Fig. 26.

648 The N_{rechits} is the main discriminant for the analysis, and is defined as the number of RecHits
 649 in the signal cluster. The distributions for signal and background control regions are shown in
 650 Fig. 27. The ABCD plane is illustrated in Fig. 34, where bin D is the signal enhanced region,
 651 with small values of $\Delta\phi(\text{cluster}, \text{MET})$ and large values of N_{rechits} . The independence of the two
 652 variables in background are validated using several background-enriched validation regions,
 653 detailed in Section 6.2. The estimation of the number of events in each bin is expressed by Eq. 4
 654 below:

$$\begin{aligned} N_A &= c_1 \times c_2 \times Bkg_C + \mu \times SigA \\ N_B &= c_1 \times Bkg_C + \mu \times SigB \\ N_C &= Bkg_C + \mu \times SigC \\ N_D &= c_2 \times Bkg_C + \mu \times SigD \end{aligned} \tag{4}$$

655 Where:

- 656 • $SigA, SigB, SigC, SigD$ are the number of signal events expected in bin A, B, C, and
 657 D, taken from the signal MC prediction.
- 658 • μ is the signal strength (the model parameter of interest)
- 659 • c_1 is the ratio between background in B and C; c_2 is the ratio between background in
 660 D and C; Both c_1 and c_2 are essentially interpreted as nuisance parameters that are
 661 unconstrained in the fit.
- 662 • Bkg_C is the number of background events in bin C.

The four unknown variables (Bkg_C, c_1, c_2, μ) are extracted from a maximum likelihood fit with the following likelihood expression:

$$L = \prod_i^{ABCD} Pois(obs_i|N_i) \times \prod_i^{nuisance} Constraints(\sigma_j|\hat{\sigma}_j) \quad (5)$$

- 663 Where obs_i is the number of observed events in each bin and σ_j are the nuisance parameters.
 664 All the nuisance parameters are implemented with a log-normal distribution, such that the
 665 logarithm of the distribution is a Gaussian constraint.

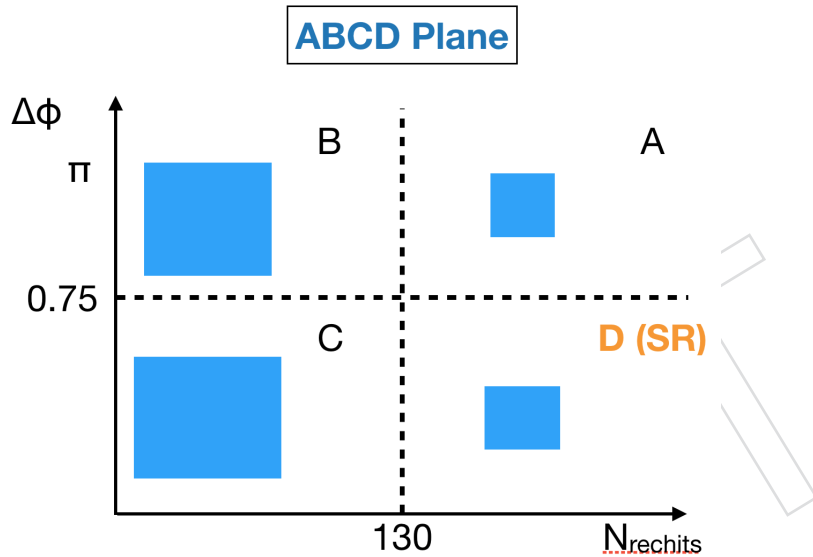


Figure 34: The diagram of the ABCD plane is shown.

6.2 Validation of the Estimation Method

666 Two validation regions are defined in order to assess the independence of the two discriminating variables used for the ABCD method ($\Delta\phi$ (cluster, MET) and $N_{rechits}$) and to test for the accuracy of the ABCD background estimation method. The two validation regions are the in-time validation region discussed in subsection 6.2.2 and the early out-of-time (OOT) validation region, discussed in subsection 6.2.1.

672 The in-time validation region is defined by inverting the cluster identification requirement in
 673 the signal region event selection. Inverting the cluster identification requirements suppresses
 674 the signal and yields a background-only validation region that is most similar in composition
 675 to the signal region. As discussed earlier, based on simulation studies, we understand
 676 the background to be predominantly from isolated long-lived particle (K_L and neutron) production
 677 from pileup interactions, but include small contributions from muon bremsstrahlung.
 678 Therefore, this validation region allows us to test the accuracy of the ABCD background esti-
 679 mation method for a background composition that includes the small contribution from muon
 680 bremsstrahlung process which is also present in the signal region.

681 The early OOT validation region selects background clusters purely from pileup interactions.
 682 As signal can only occupy the in-time bunch crossing, this validation region does not require us
 683 to invert the cluster identification requirements to suppress signal contamination. Therefore,
 684 the early OOT validation region allows us to check the accuracy of the ABCD background

estimation method for clusters resulting from the pileup background which passes the cluster identification requirements.

6.2.1 Early Out-of-time Validation Region

The early OOT validation region is defined by the set of signal selections described in Section 5, except the cut-based cluster ID is not applied and the time cut is modified to select clusters with time < -12.5 ns. The cut-based cluster ID requirement is not applied in order to allow us to validate the ABCD method independently for clusters that pass and fail the cut-based cluster ID requirement. The positive time windows is excluded because it may be contaminated by signals with LLPs that travel with slower velocity, creating showers that are delayed in time. This early OOT validation region is dominated by clusters produced by isolated LLPs from OOT pileup interactions.

The Pearson correlation coefficient between the $\Delta\phi(\text{cluster}, \text{MET})$ and N_{rechits} variables is 0.02 in this region which indicates that these two variables used for the ABCD method are independent. The early OOT validation region is separated into two categories: events with clusters that pass cluster ID, and events with clusters that fail cluster ID. We validate the ABCD background prediction method in both categories to demonstrate that the accuracy of the ABCD method is not impacted by the cluster ID requirements.

The distribution of $\Delta\phi(\text{cluster}, \text{MET})$ and N_{rechits} in the out-of-time validation region is shown in Fig. 35 for events that pass and fail the cluster ID respectively.

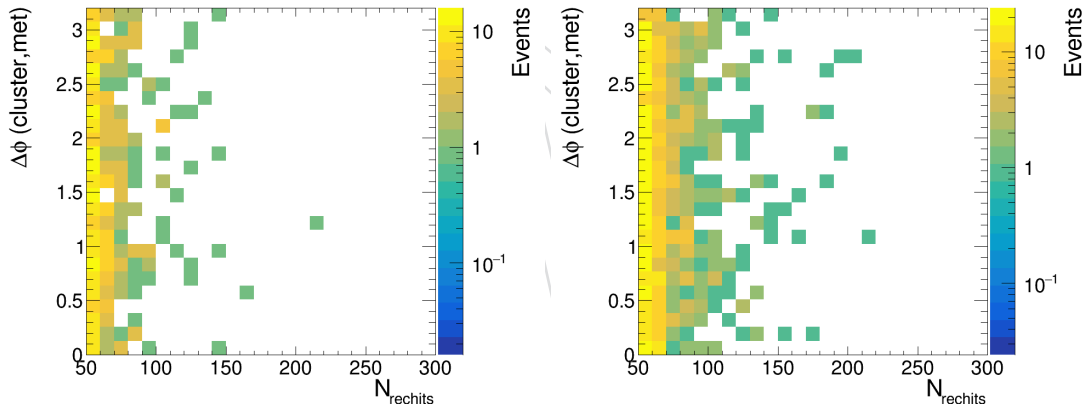


Figure 35: The distribution of $\Delta\phi(\text{cluster}, \text{MET})$ and N_{rechits} for clusters that pass(Left) and fail(Right) cluster ID in the early OOT validation region.

In Table 14 we show the comparison between the ABCD method prediction and the observation in the signal-enriched bin B for the nominal cut values of $N_{\text{rechits}} = 130$ and $\Delta\phi(\text{cluster}, \text{MET}) = 0.75$. The prediction agrees well with the observation for both cases, within the statistical uncertainty of the validation region.

The validation test is also performed for several different values of the cuts in N_{rechits} and $\Delta\phi(\text{cluster}, \text{MET})$. In Table 15 and Table 16, we show the validation test results for N_{rechits} cut boundary values ranging from 100 to 160, while keeping $\Delta\phi(\text{cluster}, \text{MET})$ cut boundary fixed at 0.75, for the passing and failing clusterID region, respectively. In Table 17 and Table 18 we show the validation test result when scanning the $\Delta\phi(\text{cluster}, \text{MET})$ cut boundary from 0.6 to 0.9, while keeping N_{rechits} cut boundary fixed at 130, for the passing and failing clusterID region, respectively. The observed yields in the signal-enriched region D agrees well with the prediction in most cases. We also observe no significant trends as the boundaries are varied.

Table 14: Validation of the ABCD method in early OOT validation region at the nominal cut values. The uncertainty of the prediction is the statistical uncertainty propagated from bin A, B, and C.

Cluster ID	A	B	C	D	Prediction ($\frac{A \times C}{B}$)
Pass Cluster ID	5	373	97	2	1.30 ± 0.60
Fail Cluster ID	26	732	222	6	7.89 ± 1.66

Table 15: Validation of the ABCD method in early OOT, pass ID validation region, scanning $N_{rechits}$. The uncertainty of the prediction is the statistical uncertainty propagated from bin A, B, and C.

$N_{rechits}$	A	B	C	D	Prediction ($\frac{A \times C}{B}$)
100	25	353	96	3	6.80 ± 1.57
110	14	364	96	3	3.69 ± 1.07
120	10	368	96	3	2.61 ± 0.88
130	5	373	97	2	1.30 ± 0.60
140	4	374	97	2	1.04 ± 0.53
150	1	377	98	1	0.26 ± 0.26
160	1	377	98	1	0.26 ± 0.26

Table 16: Validation of the ABCD method in early OOT, fail ID validation region, scanning $N_{rechits}$. The uncertainty of the prediction is the statistical uncertainty propagated from bin A, B, and C.

$N_{rechits}$	A	B	C	D	Prediction ($\frac{A \times C}{B}$)
100	72	686	208	20	21.83 ± 3.10
110	46	712	215	13	13.89 ± 2.32
120	36	722	218	10	10.87 ± 2.00
130	26	732	222	6	7.89 ± 1.66
140	19	739	226	2	5.81 ± 1.40
150	14	744	226	2	4.25 ± 1.18
160	12	746	227	1	3.65 ± 1.09

Table 17: Validation of the ABCD method in early OOT, pass ID validation region, scanning $\Delta\phi(\text{cluster, MET})$. The uncertainty of the prediction is the statistical uncertainty propagated from bin A, B, and C.

$\Delta\phi(\text{cluster, MET})$	A	B	C	D	Prediction ($\frac{A \times C}{B}$)
0.60	5	397	73	2	0.92 ± 0.43
0.65	5	392	78	2	0.99 ± 0.46
0.70	5	379	91	2	1.2 ± 0.55
0.75	5	373	97	2	1.3 ± 0.6
0.80	5	365	105	2	1.44 ± 0.66
0.85	5	354	116	2	1.64 ± 0.75
0.90	5	343	127	2	1.85 ± 0.85

Table 18: Validation of the ABCD method in early OOT, fail ID validation region, scanning $\Delta\phi(\text{cluster}, \text{MET})$. The uncertainty of the prediction is the statistical uncertainty propagated from bin A, B, and C.

$\Delta\phi(\text{cluster}, \text{MET})$	A	B	C	D	Prediction ($\frac{A \times C}{B}$)
0.60	26	783	171	6	5.68 ± 1.21
0.65	26	768	186	6	6.3 ± 1.34
0.70	26	752	202	6	6.98 ± 1.48
0.75	26	732	222	6	7.89 ± 1.66
0.80	25	715	239	7	8.36 ± 1.78
0.85	25	696	258	7	9.27 ± 1.97
0.90	25	685	269	7	9.82 ± 2.09

716 **6.2.2 In-time Validation Region**

717 The in-time validation region is defined by the same set of selections summarized in Section
 718 5, except the cluster identification requirement is inverted. Unlike the OOT validation region
 719 introduced in the previous section, the cluster time cut is kept the same as the signal region
 720 selection. Therefore, the background composition of this in-time validation region more closely
 721 resembles the signal region. As stated previously the background is predominantly from pileup
 722 interactions with some small contribution from muon bremsstrahlung in W+Jets events. The
 723 Pearson correlation coefficient between $\Delta\phi(\text{cluster}, \text{MET})$ and N_{rechits} is 0.04 in this region, and
 724 again indicates that the two variables used in the ABCD method are independent.

725 The distribution of $\Delta\phi(\text{cluster}, \text{MET})$ and N_{rechits} in the in-time validation region is shown in
 726 Fig. 36.

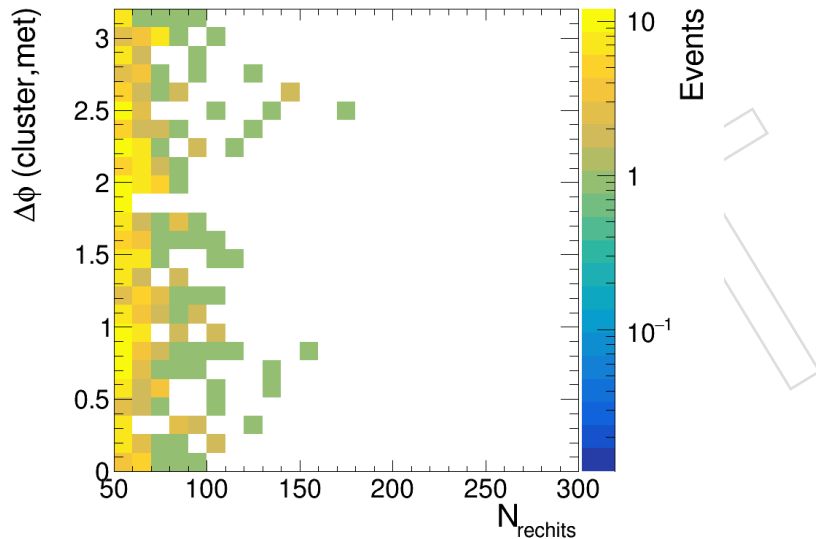


Figure 36: The distribution of $\Delta\phi(\text{cluster}, \text{MET})$ and N_{rechits} in the in-time validation region.

727 In Table 19, we compare the observed event yield in the signal-enriched bin D with the ABCD
 728 method prediction and observe agreement.
 729 Since good agreement is observed in both validation regions, we assign no systematic uncer-
 730 tainty to the background prediction.
 731 Similar to the OOT validation region, we also perform the validation test for a range of cut
 732 boundary values on the N_{rechits} and $\Delta\phi(\text{cluster}, \text{MET})$ variable. Table 20 shows the valida-
 733 tion test results for N_{rechits} cut boundary values ranging from 100 to 160, while keeping the
 734 $\Delta\phi(\text{cluster}, \text{MET})$ boundary fixed at 0.75. Table 21 shows the validation test result for $\Delta\phi(\text{cluster}, \text{MET})$
 735 boundary values ranging from 0.6 to 0, while keeping N_{rechits} boundary fixed at 130.

Table 19: Validation of the ABCD method in in-time validation region. The uncertainty of the prediction is the statistical uncertainty propagated from bin A, B, and C.

Cluster ID	A	B	C	D	Prediction ($\frac{A \times C}{B}$)
Fail Cluster ID	5	269	74	2	1.38 ± 0.64

Table 20: Validation of the ABCD method in in-time validation region, scanning $N_{rechits}$. The uncertainty of the prediction is the statistical uncertainty propagated from bin A, B, and C.

$N_{rechits}$	A	B	C	D	Prediction ($\frac{A \times C}{B}$)
100	18	256	69	7	4.85 ± 1.32
110	10	264	73	3	2.77 ± 0.95
120	7	267	73	3	1.91 ± 0.77
130	5	269	74	2	1.38 ± 0.64
140	4	270	76	0	1.13 ± 0.58
150	2	272	76	0	0.56 ± 0.4
160	1	273	76	0	0.28 ± 0.28

Table 21: Validation of the ABCD method in in-time validation region, scanning $\Delta\phi(\text{cluster}, \text{MET})$. The uncertainty of the prediction is the statistical uncertainty propagated from bin A, B, and C.

$\Delta\phi(\text{cluster}, \text{MET})$	A	B	C	D	Prediction ($\frac{A \times C}{B}$)
0.60	6	287	56	1	1.17 ± 0.51
0.65	6	282	61	1	1.3 ± 0.56
0.70	5	275	68	2	1.24 ± 0.58
0.75	5	269	74	2	1.38 ± 0.64
0.80	5	262	81	2	1.55 ± 0.72
0.85	4	262	81	3	1.24 ± 0.64
0.90	4	244	99	3	1.62 ± 0.83

736 Prior to unblinding, we make a projection of the yields in the A, B, C, and D bins in the sig-
737 nal region by extrapolating the yields from the out-of-time validation region that have clus-
738 terers passing the cluster identification requirements, as described in Section 5.3. The projected
739 yields are summarized in Table 35. Therefore we predict roughly half of an event in the signal-
740 enriched bin D. Note that the projections in Table 35 are not used in the final result in any way,
741 they were just preliminary projections for the background prior to unblinding.

Table 22: Number of background events predicted in the signal region.

A	B	C	D
1.77	132.40	34.43	0.46 ± 0.56

DRAFT

7 Signal CSC Cluster Simulation

The main objects used for this analysis are the CSC Rechit clusters. In this section, we study the accuracy of the simulation in modeling the detector response, cluster reconstruction, and cluster identification.

The LLP signal cluster is produced by a neutral invisible particle that travels through the bulk of the calorimeter and iron return yoke material without interacting, and subsequently decays into hadronic particles in the material near the CSC muon chambers. There are almost no standard model background processes which interact in exactly this way, and it is impossible to cleanly isolate such processes. Instead, we use the muon bremsstrahlung process as a proxy to study signal-like clusters. High p_T muons have some non-zero probability to undergo bremsstrahlung in the material near the CSC muon chambers and produce photons that undergo an electromagnetic shower in the material near the CSC muon chambers very analogous to our signal processes. As we have collected a very large dataset Z boson to dimuon decays, we end up with a sufficiently large sample to allow us to study these rare bremsstrahlung processes.

The muon bremsstrahlung control region is defined by selecting CSC clusters that are geometrically matched to muons passing standard muon identification and isolation requirements. The exact selection definition is shown in Section 7.2. A tag-and-probe type selection is made to select a pure sample of muons from Z boson decays. We compare the simulation prediction of the CSC clusters geometrically matched to isolated muons to the data as well as important features of these CSC clusters. We show that the simulation prediction yields a reasonably accurate description of the data. We measure the residual difference between data and simulation and propagate that difference as a systematic uncertainty on our prediction of the signal yield for our search.

7.1 Data and Monte Carlo samples

The study is performed using the Zmumu skim of the SingleMuon dataset, as shown in Table 23. The simulated Monte Carlo (MC) background samples are generated for collisions at $\sqrt{s} = 13$ TeV using 2017 conditions. The samples used are collected in Table 24. These were the only available samples containing the correct data-tier needed to reconstruct CSC rechit clusters and to perform the study.

The simulation modelling study is performed using the MC samples and data from 2017. Data from 2016 and 2018 are only used to compare with 2017 data to ensure that the condition change doesn't change the modelling significantly.

7.2 Selections

7.2.1 Tag and Probe Method

A tag-and-probe method is used to select for $Z \rightarrow \mu\mu$ events. We select events with two muons with opposite charges, with one muon passing the tight identification and isolation requirements (tag muon) and the other muon passing the loose identification and isolation requirements (probe muon). For MC samples, an additional requirement is added for the pair of reconstructed muons to be matched to two generator-level muons. The selections are summarized in Table 25 and the identification and isolation requirements are implemented based on the recommendations from the Muon Physics Object Group[32]. This tag-and-probe method is used in order to reduce any potential biases on the cluster characteristics that may result from the use of tight muon identification criteria.

Table 23: RAW-RECO Zmumu skim of SingleMuon datasets used for the simulation modelling study.

/SingleMuon/Run2016B-ZMu-07Aug17_ver1-v1/Raw-Reco
/SingleMuon/Run2016B-ZMu-07Aug17_ver2-v1/Raw-Reco
/SingleMuon/Run2016C-ZMu-07Aug17-v1/Raw-Reco
/SingleMuon/Run2016D-ZMu-07Aug17-v1/Raw-Reco
/SingleMuon/Run2016E-ZMu-07Aug17-v1/Raw-Reco
/SingleMuon/Run2016F-ZMu-07Aug17-v1/Raw-Reco
/SingleMuon/Run2016G-ZMu-07Aug17-v1/Raw-Reco
/SingleMuon/Run2016H-ZMu-07Aug17-v1/Raw-Reco
/SingleMuon/Run2017H-ZMu-17Nov2017-v2/Raw-Reco
/SingleMuon/Run2017G-ZMu-17Nov2017-v1/Raw-Reco
/SingleMuon/Run2017F-ZMu-17Nov2017-v1/Raw-Reco
/SingleMuon/Run2017E-ZMu-17Nov2017-v1/Raw-Reco
/SingleMuon/Run2017D-ZMu-17Nov2017-v1/Raw-Reco
/SingleMuon/Run2017C-ZMu-17Nov2017-v1/Raw-Reco
/SingleMuon/Run2017B-ZMu-17Nov2017-v1/Raw-Reco
/SingleMuon/Run2018A-ZMu-17Sep2018-v2/Raw-Reco
/SingleMuon/Run2018B-ZMu-17Sep2018-v1/Raw-Reco
/SingleMuon/Run2018C-ZMu-17Sep2018-v1/Raw-Reco
/SingleMuon/Run2018D-ZMu-PromptReco-v2/Raw-Reco

Table 24: 2017 Monte Carlo samples used for the simulation modelling study.

MC samples	σ (pb)
ZToMuMu_NNPDF31_13TeV-powheg_M_50_120	2112.9
ZToMuMu_NNPDF31_13TeV-powheg_M_120_200	20.55
ZToMuMu_NNPDF31_13TeV-powheg_M_200_400	2.889
ZToMuMu_NNPDF31_13TeV-powheg_M_400_800	0.251

<u>Tag muon selection</u>	<u>Probe muon selection</u>
<ul style="list-style-type: none"> • $p_T > 50$ GeV • $\eta < 2.4$ • Particle-Flow isolation < 0.15 • Tight muon identification • for MC samples, $\Delta R(\text{genmuon}, \text{probemuon}) < 0.4$ 	<ul style="list-style-type: none"> • $p_T > 50$ GeV • $\eta < 2.4$ • Particle-Flow isolation < 0.25 • Loose muon identification • for MC samples, $\Delta R(\text{genmuon}, \text{probemuon}) < 0.4$
<u>Tag and probe pair selection</u>	
<ul style="list-style-type: none"> • Opposite charge • Tag and probe pair invariant mass > 120 GeV 	

Table 25: Tag and Probe selection

786 MC samples are normalized to the cross sections in Table 24 and then a k-factor is derived for
 787 each mass bin individually, such that the normalizations of MC samples are the same as that
 788 of data. The derived k-factors are 1.07, 1.11, 1.39, and 1.42 for the mass bins 50-120, 120-200,
 789 200-400, and 400-800 GeV, respectively. The dimuon mass distributions of data and simulations
 790 after the normalization procedure is shown in Fig. 37.

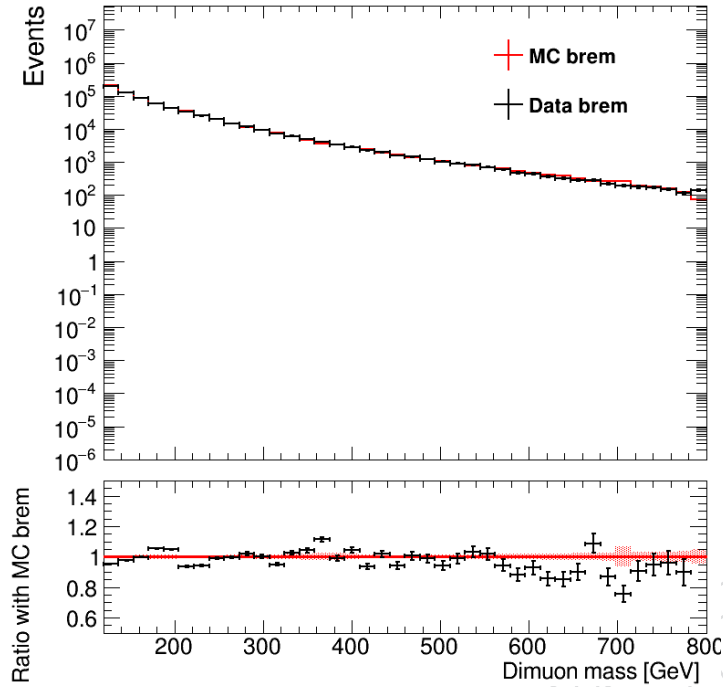


Figure 37: The dimuon mass distributions of data and mc for events that pass the Tag and Probe selections. No CSC cluster requirements are implemented yet.

7.2.2 Cluster-level Selections

In addition to the Tag and Probe selections that select for $Z \rightarrow \mu\mu$ events, a CSC cluster matched to the probe muon is required to identify the muon bremsstrahlung events. The CSC clusters are selected with a few baseline selections in line with the cuts used in the analysis, as outlined in Table 26.

Cluster selection	
<ul style="list-style-type: none"> • $\text{abs}(\text{cluster time}) < 12.5 \text{ ns}$ • $\text{timeSpread}(\text{cluster}) < 20 \text{ ns}$ • Cluster max chamber is not ME1/1 or ME1/2 • Cluster $\eta < 2.0$ • $\Delta R(\text{cluster}, \text{probemuon}) < 0.4$ 	

Table 26: Cluster selection

The dimuon mass distributions of data and simulation after requiring a CSC cluster matched to the probe muon is shown in Fig. 38. The data/MC agreement observed in the dimuon mass distributions show preliminary indication that the cluster efficiency is well modelled.

7.3 Cluster Efficiency

The cluster efficiency probes the product of bremsstrahlung probability and cluster reconstruction efficiency. It is measured by calculating the ratio between the number of events with a cluster matched to probe muon and the number of events passing the tag and probe selection.

Any differences in the cluster efficiency that is observed can be attributed to either simulation mismodeling of the bremsstrahlung rate or to mismodeling of the cluster reconstruction efficiency. Although bremsstrahlung rate mismodeling is more likely as that requires accurate

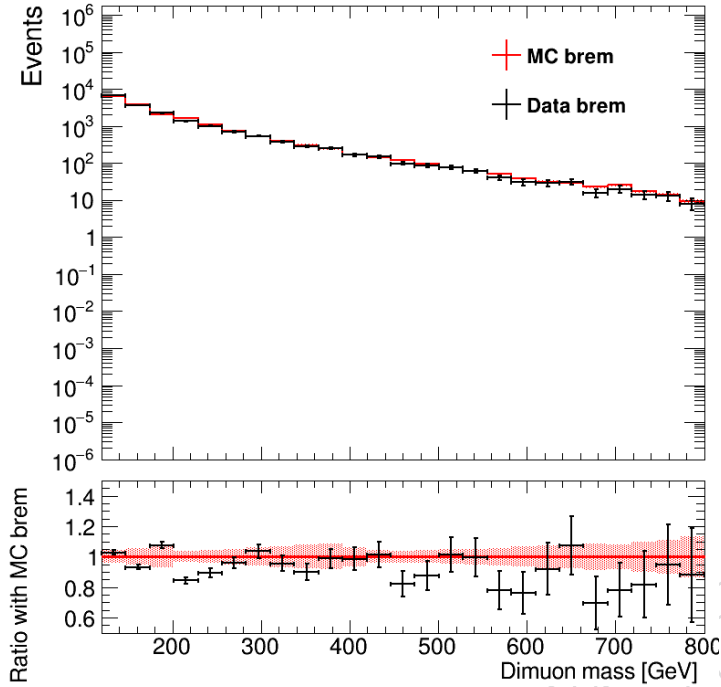


Figure 38: The dimuon mass distributions of data and mc for events that pass the Tag and Probe selections and has a CSC cluster matched to the probe muon.

modeling of material budget and tuning of simulation parameters, we will propagate the full difference as a systematic uncertainty on the cluster reconstruction efficiency as an attempt to be very conservative on the accuracy of the signal prediction.

The cluster reconstruction efficiency is implicitly testing two aspects: (a) the hit multiplicity response of the CSC detectors to a particle shower caused by the LLP decay, and (b) the efficiency of the DBSCAN clustering algorithm. Given a large hit multiplicity detector response, the efficiency of the clustering algorithm is extremely high and will be near fully efficient. Therefore, the main effect we measure with the muon brem control region is the CSC hit multiplicity response. In Fig. 39, we show the $N_{rechits}$ distributions for data and MC for the probe clusters selected using the tag and probe method described above. We observe reasonably good agreement between data and simulation prediction, indicating that the simulation is reasonably accurate in predicting the hit multiplicity response.

Using the ZToMuMu control region, we measure what fraction of muon probes produce clusters with $N_{rechits} \geq 130$ in data and MC simulation. We find that $0.58\% \pm 0.04\%$ of muon probes produce such clusters in MC simulation and $0.51\% \pm 0.01\%$ of muon probes produce such clusters in data. The small residual difference indicates that the MC simulation predicts a slightly larger hit-multiplicity response than the data. A 5% reduction to the hit-multiplicity response in the MC simulation would yield the same fraction (0.51%) of clusters with $N_{rechits} \geq 130$ observed in the ZToMuMu control region data. Implementing the 5% reduction in the hit-multiplicity response would reduce the signal yield in the signal region by a few percent for various signal models. To cover the maximum variation, we use the maximum measured, which is 3.5% as the systematic uncertainty.

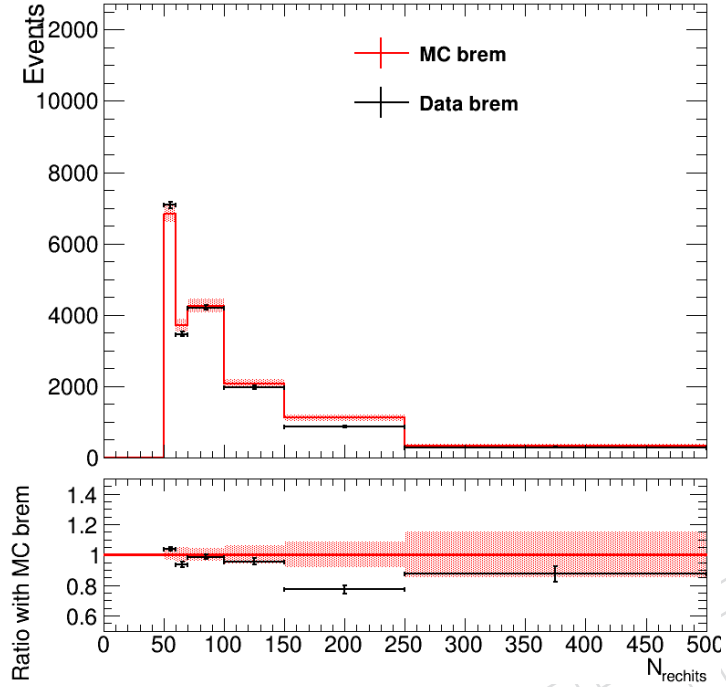


Figure 39: The N_{rechits} distributions for data and MC are shown.

827 7.4 Cluster Identification Efficiency

828 In this section, we study the simulation modelling of the efficiency of the cluster ID, as defined
 829 in Section 5.1.1. Recall that the cluster ID requirement is essentially an $|\eta|$ selection requirement
 830 with varying degree of strictness depending on the cluster N_{station} and the average station num-
 831 ber. The cluster η distribution is only impacted by the production mechanism of the signal and
 832 is therefore perfectly simulated. Potential cluster ID efficiency mismodeling may result from
 833 simulation mismodeling of the shape of the N_{station} and the average station number distribu-
 834 tion.

835 Therefore, we measure the accuracy of the simulation prediction for the cluster N_{station} and
 836 average station number distribution using the $Z \rightarrow \mu\mu$ bremsstrahlung sample. The comparison
 837 of the shapes of the cluster N_{station} and the average station number distribution predicted by
 838 simulation and observed in data are shown in Fig. 40. We only show two bins for the N_{station}
 839 distribution because the cluster ID requirement only distinguishes between $N_{\text{station}} = 1$ and
 840 $N_{\text{station}} \geq 2$. The average station number distribution is shown only for clusters that have
 841 $N_{\text{station}} = 1$, because for clusters with $N_{\text{station}} \geq 2$, there is no additional requirement on $|\eta|$
 842 beyond the pre-selection.

843 Using the Data/MC ratios measured in this muon bremsstrahlung control region, we check
 844 the impact of applying these simulation-to-data correction factors that corrects the simulation
 845 shapes to the data shapes. We observe that applying such corrections would result in a 1-
 846 5% correction to the signal yield in the signal region depending on the signal model parameter
 847 points. Therefore, we propagate a systematic uncertainty of 5% to cover for this potential effect.

848 7.5 Jet Veto Efficiency

849 The jet veto is applied to suppress punchthrough jets, as described in Section 5.1. The jet veto
 850 inefficiency for signal events come from the accidental matching of the signal cluster to either

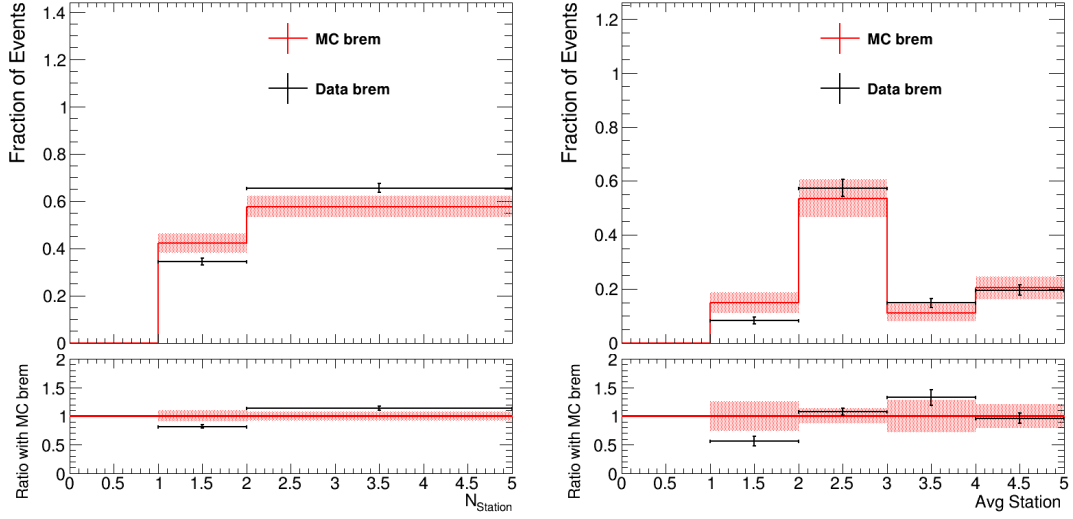


Figure 40: The N_{station} (Left) and average station number (Right) distributions with N_{rechits} cut of 130. The average station number distributions have an additional $N_{\text{station}} = 1$ requirement.

851 pileup jets or jets from the decay of the other LLP that decays close to the interaction point.
 852 The composition of the two components depend on the mass and $c\tau$ of the signal model, which
 853 determines how likely that the other LLP decays close to the interaction point and the topology
 854 of the two LLPs. The accidental matching to the other LLP only dominates for $c\tau = 100$ mm.
 855 For all the other signal models, the pileup jet matching dominates the jet veto inefficiency.

856 To validate that the jet veto efficiency is well-modelled in simulation, in case of the mismod-
 857 elling of the pileup jet distributions, we measure the jet veto efficiency in simulation and data
 858 in the ZToMuMu control region, where the events are required to pass the tag and probe se-
 859 lections described in Section 7.2, but no CSC clusters are required. To simulate the accidental
 860 matching of the clusters to pileup jets, for each event, we randomly select a (η, ϕ) position from
 861 the signal cluster distribution that pass all selections but the jet veto, and check if there exists a
 862 geometrically matched jet ($p_T > 10$ GeV) within a ΔR cone of 0.4. The measured probability that
 863 the randomly selected position is not matched to a jet is the jet veto efficiency. The measured jet
 864 veto efficiency is $91.98\% \pm 0.02\%$ and $93.42\% \pm 0.06\%$ for data and MC respectively. The mea-
 865 sured difference between data and MC, 1.54%, is applied as a correction to signal simulation.
 866 The statistical uncertainty of the method 0.07% is propagated as a source of signal systematic
 867 uncertainty. Furthermore, the jet veto efficiency is measured to be $95.01\% \pm 0.33\%$ for signals,
 868 where we require the other LLP to decay outside the calorimeters ($R > 300$ cm OR $Z > 600$ cm).
 869 The jet veto efficiency with respect to the number of primary vertices is measured in the 3 re-
 870 gions, as shown in Fig. 41, where the measurements in all three regions show good agreement.
 871 An expected decrease in jet veto efficiency as N_{PV} increases is observed, since a random match
 872 is more likely with increasing amount of pileup.

873 7.6 Muon Veto Efficiency

874 The signal inefficiency for the muon veto is about 10%. 3% comes from random matching to
 875 pileup muons. The remaining 7% is due to track segments produced by decay products of the
 876 signal LLP particle which are reconstructed as standalone muons.

877 The simulation of the random matching to pileup muons is validated using the same method as
 878 the jet veto efficiency described above. We measure the muon veto efficiency in simulation and

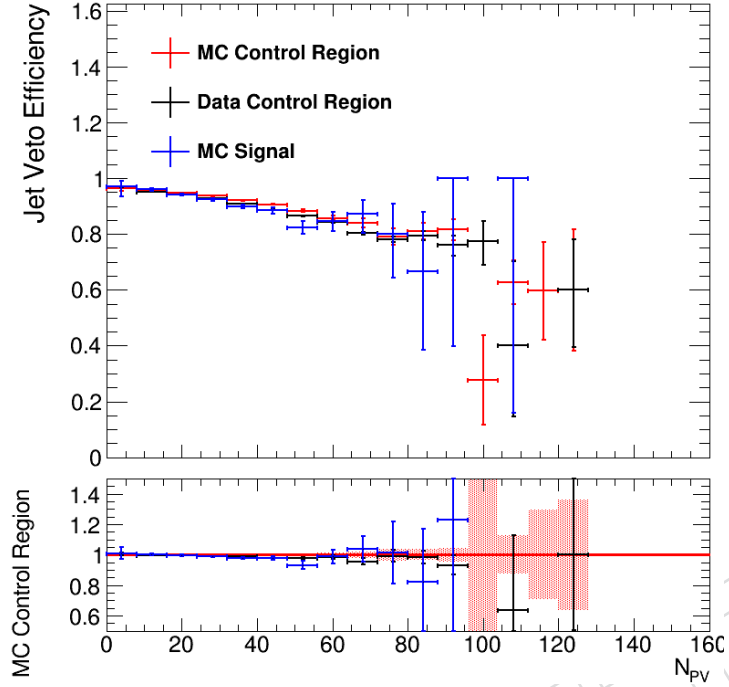


Figure 41: The jet veto efficiency measured in data/MC control region and the signal region.

879 data in the ZToMuMu control region, where the events are required to pass the tag and probe
 880 selections described in Section 7.2, but no CSC clusters are required. To simulate the accidental
 881 matching of the clusters to muons, for each event, we randomly select a (η, ϕ) position from
 882 the distribution of signal clusters passing all selections except the muon veto, but the selected
 883 position is required to be far away ($\Delta R > 0.4$) from any muons identified as resulting from the Z
 884 boson decay. Then we check if there exists a geomterically matched muon ($p_T > 20$ GeV) within
 885 a ΔR cone of 0.4. The measured probability that the randomly selected position is not matched
 886 to a muon is the muon veto efficiency. The measured muon veto efficiency is $96.83\% \pm 0.01\%$
 887 and $96.86\% \pm 0.04\%$ for data and MC respectively. The measured difference between data and
 888 MC is very small and negligible compared to other signal efficiency systematic uncertainties.
 889 The muon veto efficiency is shown in Fig. 42 as a function of the number of primary vertices.

890 The simulation of the signal inefficiency due to track segments from LLP decays that are recon-
 891 structed from standalone muons is validated in a QCD-dominated control region. The QCD
 892 MC samples and the MET-skim dataset summarized in Tables 28 and 1 respectively are used
 893 to perform the study. To select signal-like clusters, we require that clusters are matched to
 894 trackless jets, by requiring high neutral energy fraction and a small amount of charged energy
 895 fraction ($> 1\%$) to remove calorimeter noise, in addition to a few baseline selections consis-
 896 tent with the requirements for the signal region selection used in the analysis. Such objects are
 897 representative of the detector response to a signal LLP decay. The cluster-level selections are
 898 summarized in Table 27. The cluster η distribution for signal is more central compared to the
 899 distribution in the QCD control region, as shown in Fig. 43. To compensate for the difference
 900 in η distribution, the muon veto efficiency is measured as a function of cluster η in the QCD
 901 control region for data and MC, as shown in Fig. 44, with different neutral energy fraction cuts.

902 We compute the inclusive efficiency by using the cluster η distribution from signal and the
 903 scale factor measurement in Fig. 44. For the first two η bins we use the scale factors measured
 904 from $NEF > 0.8$ to gain more statistics, while for all the other η bins we use the scale factors

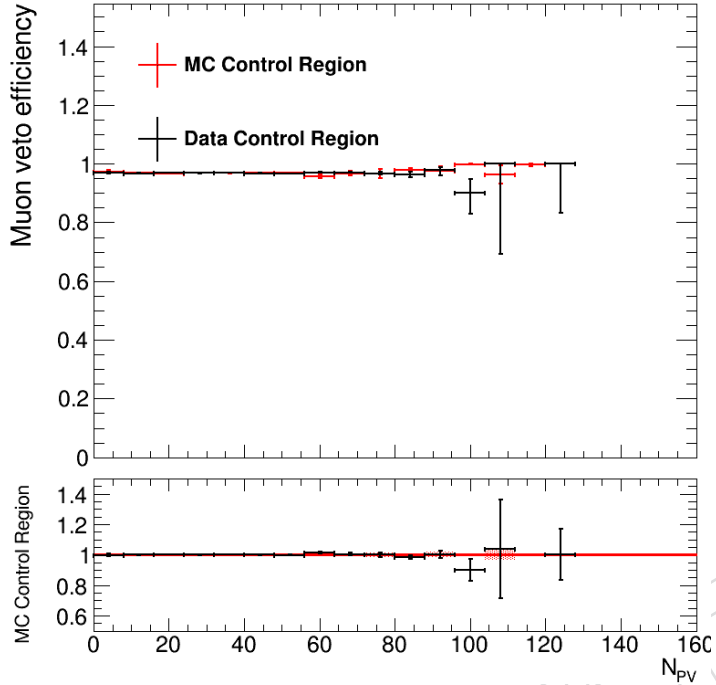


Figure 42: The muon veto efficiency measured using the random direction method is shown as a function of the number of primary vertices.

measured with cut $\text{NEF} > 0.95$, as the trackless jets with higher NEF are more signal-like.
The measured inclusive muon veto efficiency are 82.4% and 75.4% for MC and data respectively. The measured difference between data and MC is $8.5\% \pm 0.5\%$. Since this difference makes up 70% of the total signal inefficiency(10%), we apply a 6.0% correction to the signal simulation and propagate the statistical uncertainty of 4.5% as a source of signal systematic.

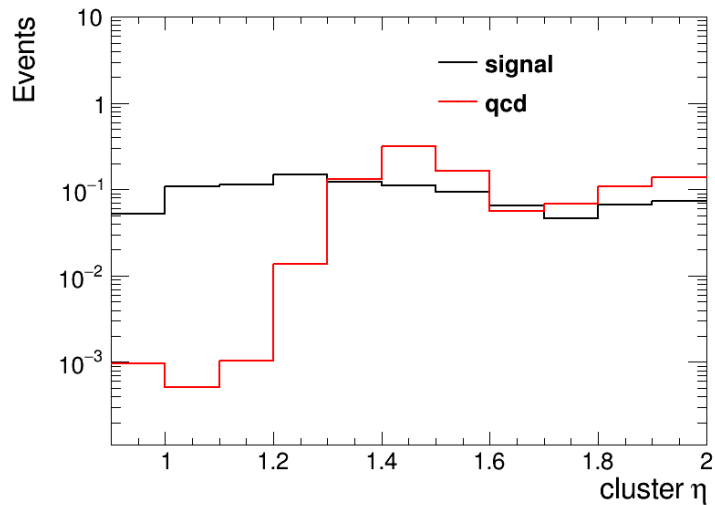


Figure 43: The cluster η distributions for signal and QCD are shown.

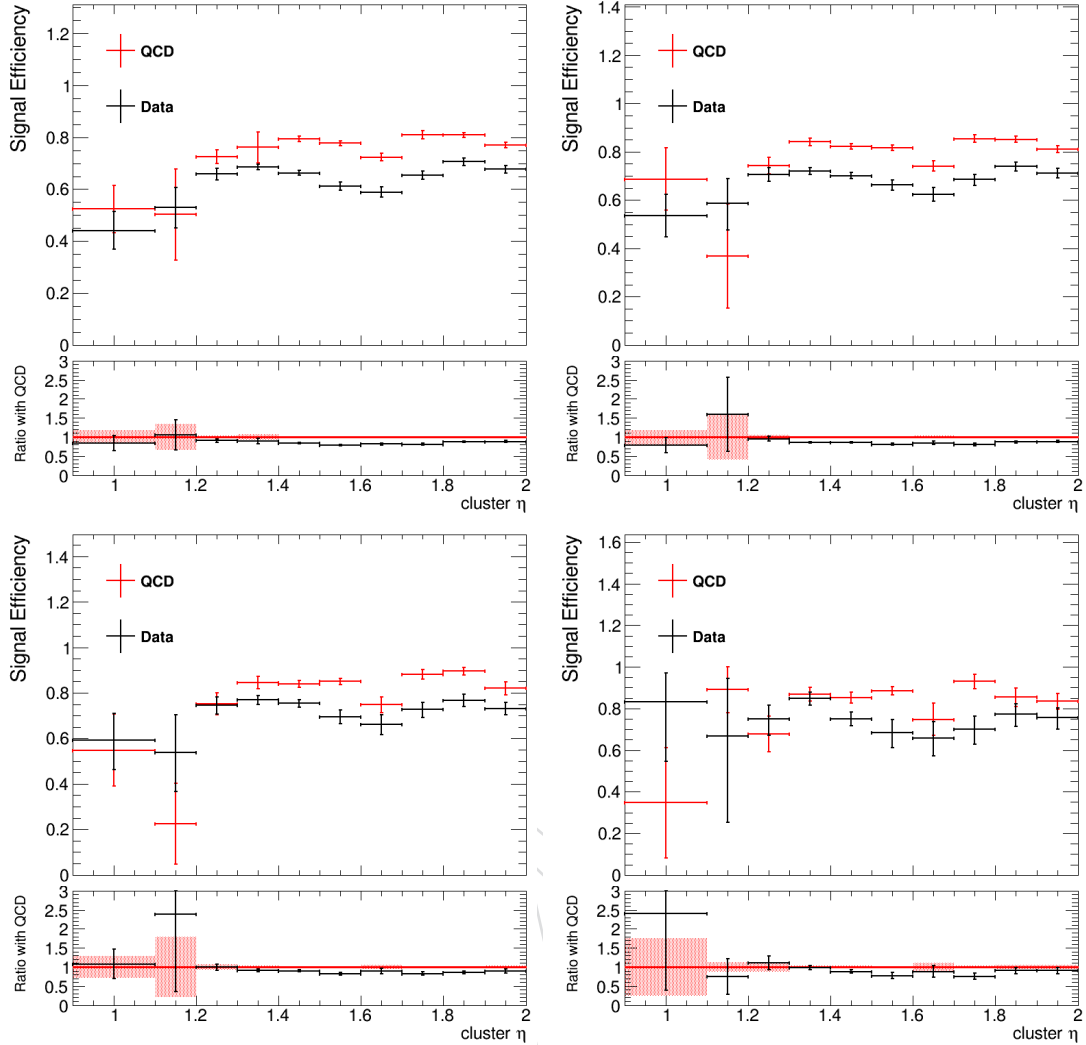


Figure 44: The muon veto efficiency as a function of cluster η for trackless jets requiring $0.8 < \text{NEF} < 0.99$ (Top Left), $0.85 < \text{NEF} < 0.99$ (Top Right), $0.9 < \text{NEF} < 0.99$ (Bottom Left), and $0.95 < \text{NEF} < 0.99$ (Bottom Right) for both data and MC are shown.

Cluster selection

- $\text{abs}(\text{cluster time}) < 12.5 \text{ ns}$
- $\text{timeSpread}(\text{cluster}) < 20 \text{ ns}$
- Cluster $|\eta| < 2.0$
- $\Delta R(\text{cluster, gen - levelmuon}) > 0.4$
- $\Delta R(\text{cluster, jet}) < 0.4$
- jet $p_T > 20 \text{ GeV}$ and jet neutral energy fraction > 0.95

Table 27: Cluster selection

910 7.7 Rechit and Segment Veto Efficiency

911 A number of vetos that reject clusters that are matched to CSC RecHits in ME1/1, ME1/2, RPC
 912 RecHits in RE1/2 and RB1, and DT segments in MB1 are applied to veto jet punchthrough and
 913 muon bremsstrahlung, as described in subsection 5.1.

Table 28: Monte Carlo samples used for the simulation modelling study.

MC samples
QCD_HT700to1000_TuneCP5_13TeV-madgraphMLM-pythia8/* /USER
QCD_HT1000to1500_TuneCP5_13TeV-madgraphMLM-pythia8/* /USER

914 To ensure that the signal veto efficiencies are well simulated, we measured the veto efficiency
 915 of the 5 vetos together in the ZToMuMu control region, where the events are required to pass
 916 the tag and probe selections described in Section 7.2, but not cluster requirements are imple-
 917 mented. The same method used to measure the jet veto efficiency is applied. We randomly
 918 select a (η, ϕ) position from the signal cluster distribution that pass all selections but the Re-
 919 chit/Segment vetos, but the position is required to be far away ($\Delta R \gtrsim 0.4$) from any muons
 920 identified as resulting from the Z boson decay. Then we check if there exists a geometrically
 921 matched Rechit/Segment(corresponding to the vetos) within a ΔR cone of 0.4. The measured
 922 probability that the randomly selected position is not matched to a Rechit/Segment is the veto
 923 efficiency. The measured inclusive efficiency is $80.97\% \pm 0.03\%$ and $83.74\% \pm 0.08\%$ for data
 924 and MC respectively. Therefore, an correction of 3.3% is applied to the signal simulation and
 925 the statistical uncertainty of 0.1% is assigned as a source of signal systematic uncertainty for
 926 the correction. The veto efficiency with respect to the number of primary vertices is measured
 927 in data and MC, as shown in Fig. 45, where good agreement is observed. Similar to the jet
 928 veto efficiency, an expected decrease in efficiency is also observed as N_{PV} increases, since it's
 929 expected that the number of hits increases as the the number of pileup jet increases and are
 930 more likely to deposit hits in the first stations of the Muon System.

931 The discrepancy measured between MC and data should account for all aspects that are not
 932 well simulated, including higher rate of noise hits in data and any readout configurations that
 933 are not well simulated.

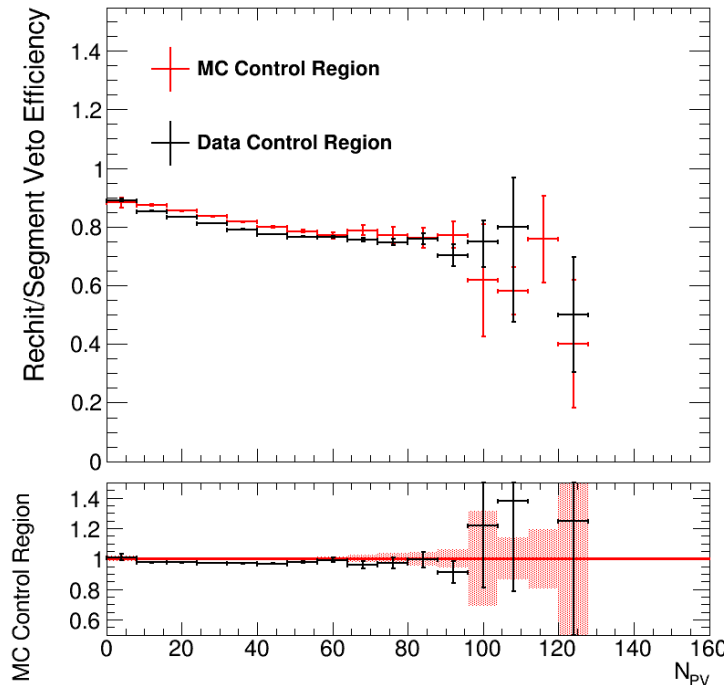


Figure 45: The Rechit/Segment veto efficiency measured in data/MC control region.

934 7.8 Cluster Time and Time Spread

935 As described in subsection 5.1, the clusters in the signal region are required to be in-time and
 936 the time spread of the cluster is required to be less than 20 ns. In this section, we will validate
 937 that the time and time spread of the clusters are well-modelled in simulation and propagate
 938 any mis-modelling as a source of systematic uncertainty.

939 Similar to the previous subsections, we perform the measurement on events that pass the tag
 940 and probe selections and has a CSC cluster matched to the probe muon, as described in Sec-
 941 tion 7.2. The requirement on cluster time or time spread is removed, when we perform the
 942 measurement on the corresponding variable.

943 The distributions of the cluster time for data and MC are shown in the left plot in Fig. 46, where
 944 the requirement on cluster time is removed. Good agreement is observed between data and
 945 MC and a gaussian fit to the data distribution results in an RMS of 1.6 ns. The efficiency of the
 946 in-time cut ($-5 \text{ ns} < t_{\text{cluster}} < 12.5 \text{ ns}$) is $98.94\% \pm 0.31\%$ and $99.84\% \pm 0.11\%$ for data and MC
 947 respectively. Therefore, an uncertainty of 0.9% is assigned as the time cut uncertainty.

948 The distributions of the cluster time spread for data and MC are shown in the right plot in
 949 Fig. 46. The distribution is relatively well-modelled and similarly, we measure the efficiency of
 950 the time spread requirement of less than 20 ns. The measured efficiency of the cut is $93.05\% \pm$
 951 0.65% and $95.74\% \pm 1.3\%$ for data and MC respectively. Therefore, an uncertainty of 2.8% is
 952 assigned as the time spread cut uncertainty.

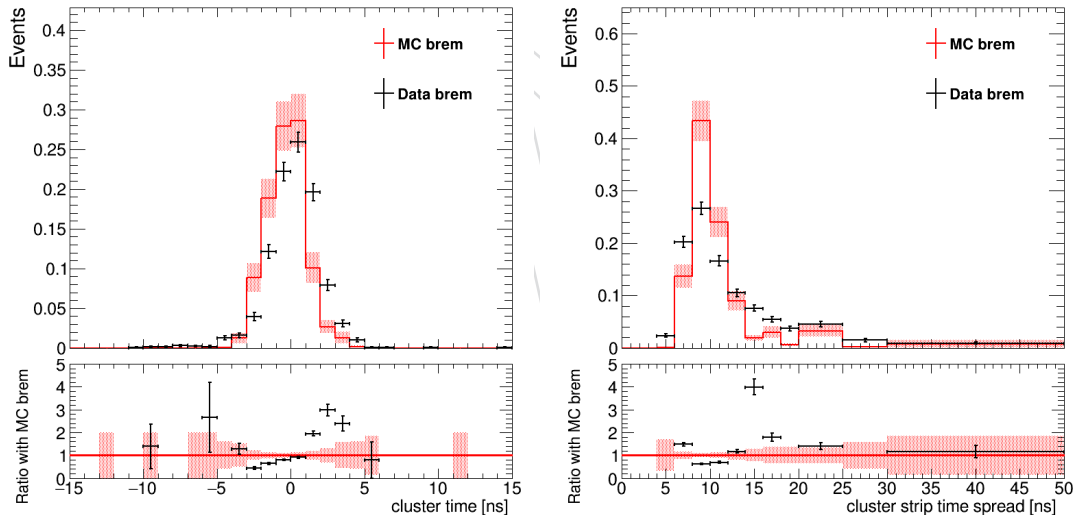


Figure 46: The cluster time(Left) and time spread (Right) distributions for MC and data.

953 7.9 Data Year Comparison

954 Since the MC samples are only available in 2017 condition, the simulation modelling studies are
 955 performed with 2017 condition. In this section, we measure each of the efficiencies presented
 956 in the previous subsections in different data taking years and demonstrate that the change in
 957 conditions has negligible effects on the efficiencies. Therefore, the uncertainties measured with
 958 2017 condition can be used for all 3 years.

959 The cluster efficiency is measured with respect to cluster η , using the nominal parameters
 960 $N_{\text{rechits}} = 130$ and $\Delta R = 0.2$ for the clustering algorithm. Good agreements are observed
 961 among all 3 years, as shown in Fig. 47.

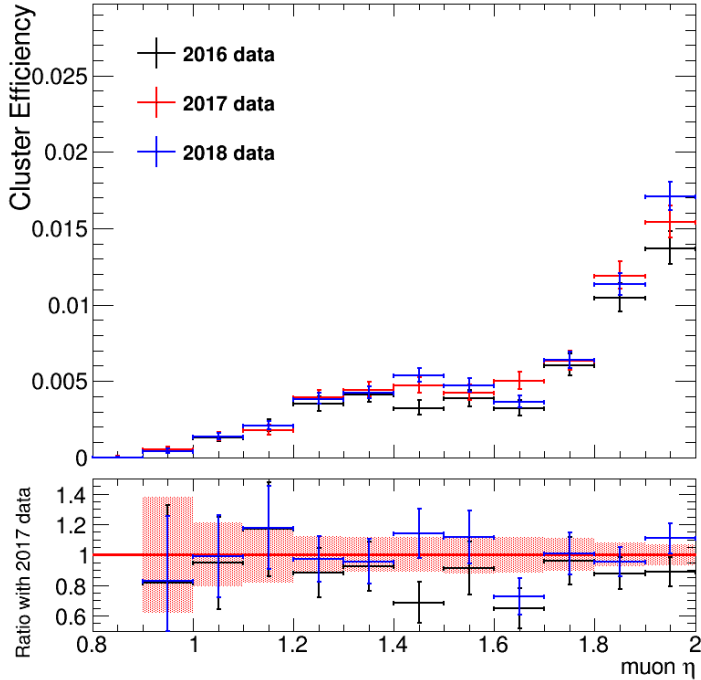


Figure 47: The cluster efficiency with respect to the probe muon η .

962 The cut-based ID efficiencies measured in data from 2016, 2017, and 2018 are shown in Table 29.
 963 The efficiencies agree within the statistical uncertainties. Good agreement between different
 964 years are also observed in the 3 cluster-level variables that are used to define the cut-based ID
 965 and the $N_{rechits}$ distribution, as shown in Fig. 48.

Table 29: Cut-based ID efficiency for different conditions.

Year	cut-based ID efficiency
2016	$65.4\% \pm 1.5\%$
2017	$65.0\% \pm 1.2\%$
2018	$65.5\% \pm 1.0\%$

966 The jet veto and Rechit/Segment veto efficiency are measured with respect to the number of
 967 primary vertices, as shown in Fig. 49. For all 3 uncertainties, we observe good agreement
 968 between all 3 years.

969 The cluster time distribution for all 3 years is shown in Fig. 50. Good agreement is shown
 970 between all 3 years.

971 Finally, the cluster time spread distribution is shown in the left plot of Fig. 51. It's observed
 972 that the distribution is wider in 2017 and 2018. The time spread distributions are shown again
 973 in the right plot of Fig. 51, after a reweighting procedure that reweights the number of pri-
 974 mary vertices distribution for all 3 years to that of 2017 condition. It can be seen that after the
 975 reweighting, the agreement between all 3 years improves significantly. The efficiency of the
 976 time spread cut for all 3 years, after reweighting is also observed to agree within the statistical
 977 uncertainty of the measurement. Therefore, the time spread uncertainty of 2.8% derived from
 978 2017 condition can be applied to all 3 years.

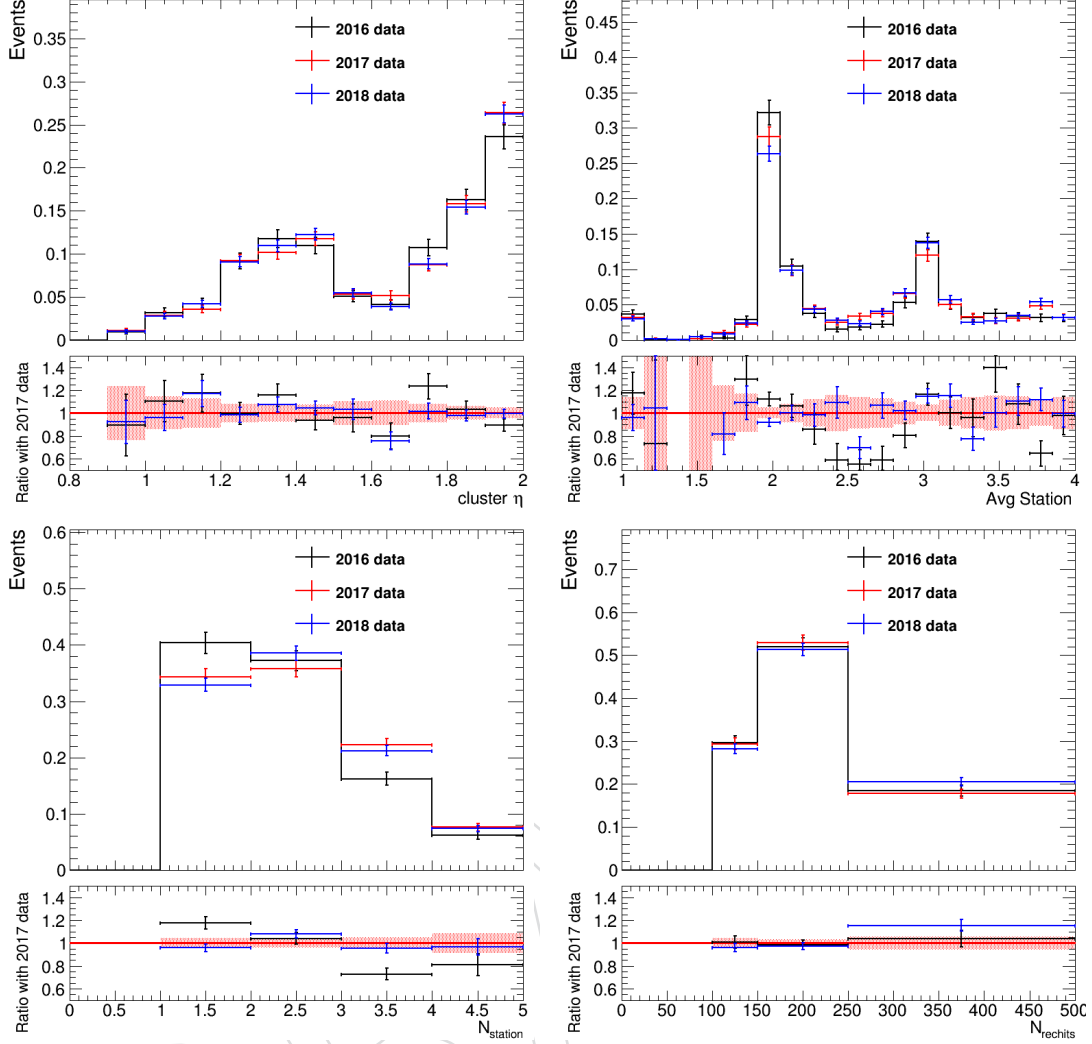


Figure 48: The cluster η (Top Left), average station number (Top Right), N_{stations} (Bottom Left), and N_{rechits} (Bottom Right) distributions in data from all 3 years. The difference in the N_{stations} distribution for different years could be pileup-related.

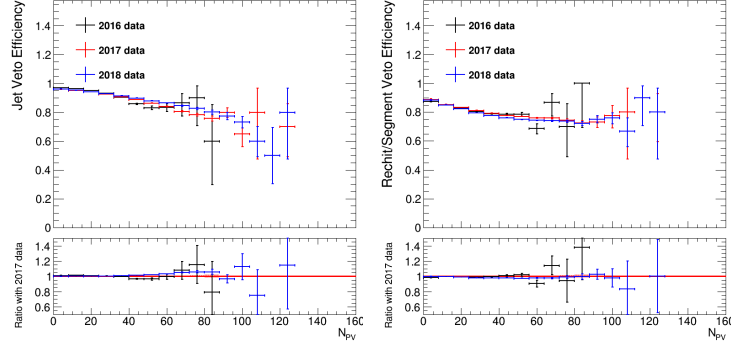


Figure 49: The jet veto (Left) and Rechit/Segment veto (Right) efficiency measured in data from all 3 years.

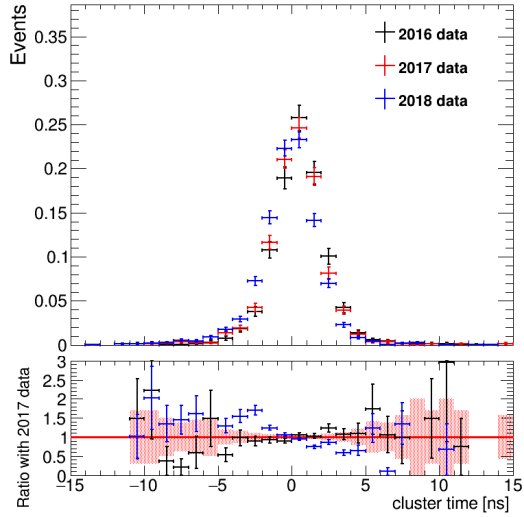


Figure 50: The cluster time distributions in data from all 3 years are shown.

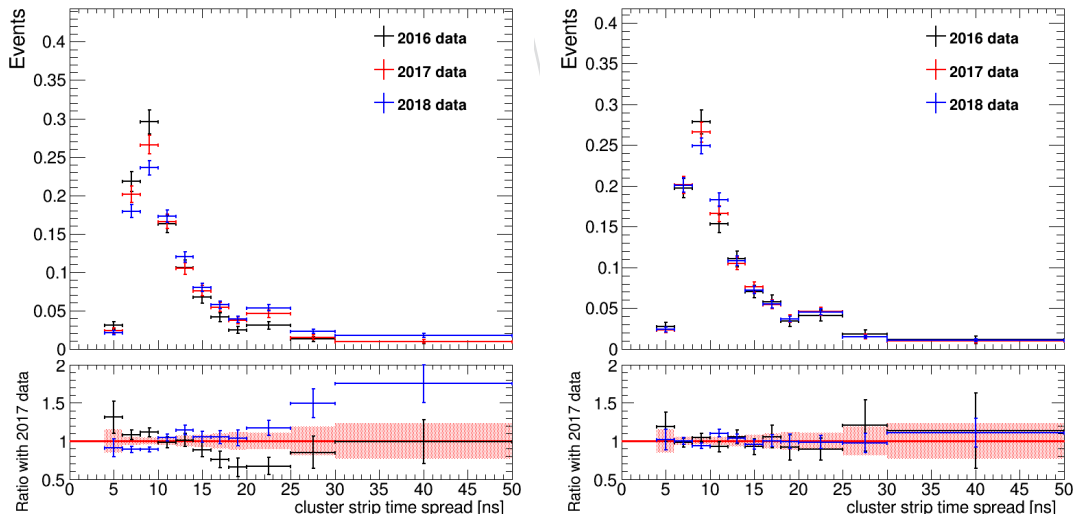


Figure 51: The cluster time spread distributions before (Left) and after (Right) reweighting to the N_{PV} distribution for 2017 are shown.

8 Uncertainties

8.1 Background Uncertainties

As mentioned before in Section 6, since we observed good agreement between the prediction and observed values in both validation regions, we assign no systematic background uncertainty. The background prediction will be dominated by the statistical uncertainty in bin A, B, and C, the background-dominated bins in the ABCD.

8.2 Signal Uncertainties

The systematic uncertainties of the signals in each bin of ABCD plane are summarized in Table 30. The theoretical signal uncertainties in the table corresponds to the uncertainty for the gluon fusion production only. The theoretical signal uncertainties for the other production modes are subdominant, as detailed in the corresponding subsections.

For the gluon fusion production, the uncertainty is dominated by the higgs p_T shape uncertainty, while for the other production modes, the uncertainty is dominated by the CSC cluster simulation modelling uncertainty.

Table 30: Signal systematic uncertainty in each bin of ABCD plane.

Uncertainty	A	B	C	D
Cluster eff	3.5%	3.5%	3.5%	3.5%
Cluster ID	5.1%	5.1%	5.1%	5.1%
Muon veto	4.5%	4.5%	4.5%	4.5%
Jet veto	0.07%	0.07%	0.07%	0.07%
Rechit veto	0.1%	0.1%	0.1%	0.1%
time	0.9%	0.9%	0.9%	0.9%
time spread	2.8%	2.8%	2.8%	2.8%
CSC readout	1%	1%	1%	1%
JES	8.4%	8.3%	4.2%	4.1%
Pileup	0.8%	1.1%	1.1%	1.1%
xsec(ggH)	6.7%(-) 4.6%(+)	6.7%(-) 4.6%(+)	6.7%(-) 4.6%(+)	6.7%(-) 4.6%(+)
PDF+ α_s (ggH)	3.2%	3.2%	3.2%	3.2%
Higgs p_T (ggH)	20.5%(-) 13.3%(+)	20.5%(-) 13.3%(+)	20.5%(-) 13.3%(+)	20.5%(-) 13.3%(+)
Luminosity	1.8%	1.8%	1.8%	1.8%
MC Statistics	7-15%	10-25%	5%	3%

8.2.1 CSC Rechit cluster modelling

This uncertainty includes uncertainties measured from the cluster efficiency, cut-based ID efficiency, jet veto efficiency, Rechit/segment veto efficiency, cluster time, and time spread.

The sum of the 6 uncertainties is on the order of 8% and the detailed measurement procedure of the efficiencies and uncertainties are performed in a muon bremsstrahlung control region, described in Section 7.

8.2.2 CSC Readout

In real data, for the CSC chamber to be readout, it must form a pre-trigger in coincidence with L1Accept. The pre-trigger is generated when there are at least two comparator (i.e., trigger-level) hits at different CSC layers and matching a given pre-defined pattern of hits. The re-

1003 requirement of pre-triggers for readout has been switched off in simulation. This discrepancy
1004 has a few effects on the signal yield prediction.

1005 The clustering algorithm could overestimate the number of CSC Rechits in signal cluster by
1006 including Rechits in chambers with a small number of hits not readout in data. We "simulate"
1007 the CSC readout for signal samples by only counting Rechits if the chamber contains ≥ 6 hits,
1008 and checked that this change has a small ($< 0.1\%$) effect on signal efficiency.

1009 This discrepancy may also lead to an underestimation of the ME1/1 and ME1/2 hit veto ef-
1010 ficiency for signal simulation. We checked the issue by loosening the ME11/12 veto to allow
1011 signal CSC cluster that is matched to ME11/12 hits, but the hits only occupy 1, 2, or 3 layer
1012 in the chambers to pass the selections. The signal gain is 0.7%, 1.3%, and 2.5%, when we al-
1013 low clusters to matched to ME11/12 hits in 1, 2, 3 layers respectively. We assign a 1% signal
1014 systematic uncertainty to account for this effect.

1015 **8.2.3 Pileup reweight**

1016 Ths size of the pileup reweight uncertainty is estimated to be about 1% for all signal models
1017 and are independent across the models. The pileup reweight uncertainty is estimated by vary-
1018 ing the the pp inelastic cross section up and down one standard deviation and measuring the
1019 variation in signal yield.

1020 **8.2.4 Luminosity**

1021 A 1.8% luminosity uncertainty is assigned for all 3 years, following the recommendation from
1022 the Luminosity Physics Object Group[43].

1023 **8.2.5 Jet Energy Scale**

1024 The size of this uncertainty is about 5-8% for all signal models. The jet energy scale uncer-
1025 tainty is assigned based on the official recommendation [34]. This uncertainty affects the trigger
1026 efficiency(MET-based), the efficiency of the MET cut and the leading jet selection. To estimate
1027 the impact of the jet energy scale uncertainty, we vary the p_T of all jets considered for the jet
1028 veto up and down by 1σ , and also propogate the effect to the missing transverse momentum.
1029 The resulting variation in signal yield in the signal region is propogated as the jet energy scale
1030 uncertainty.

1031 **8.2.6 Signal Cross Section**

1032 The theory uncertainty on the overall signal cross section for each production mode is taken
1033 from the LHC Higgs Cross Section working group yellow report 4 [30]. The uncertainty for
1034 ggH, VBF, WH, qqZH, ggZH, and ttH are: 6.7%(-) 4.6%(+), 0.3%(-) 0.4%(+), 0.7%(-) 0.5%(+),
1035 0.6%(-) 0.5%(+), 25.1%(-) 18.9%(+), and 9.2%(-) 5.8%(+), respectively.

1036 **8.2.7 Parton Density Functions and Strong Coupling Constant**

1037 The effect of PDF uncertainty and strong coupling constant uncertainty on the overall signal
1038 yield for each production mode is taken from the LHC Higgs Cross Section working group
1039 yellow report 4 [30]. The uncertainty for ggH, VBF, WH, qqZH, ggZH, and ttH are: 3.2%, 2.1%,
1040 1.9%, 1.9%, 2.4%, and 3.6%, respectively.

1041 8.2.8 Higgs p_T Reweighting for Gluon Fusion Production

1042 The higgs p_T reweight uncertainty is calculated by adjusting the renormalization and factor-
 1043 ization scale by a factor of 0.5 and 2 and re-evaluating the signal region yield with respect
 1044 to the nominal signal yield. The shape of the higgs p_T distribution with different renorma-
 1045 lization and factorization scale is shown in Fig. 52. The uncertainty calculated from the 6
 1046 variations are 6.8% ($\mu_R, \mu_F = (1.0, 2.0)$), 17.0% ($\mu_R, \mu_F = (1.0, 0.5)$), 3.3% ($\mu_R, \mu_F = (2.0, 1.0)$),
 1047 6.8% ($\mu_R, \mu_F = (0.5, 1.0)$), 10.9% ($\mu_R, \mu_F = (2.0, 2.0)$), and 9.2% ($\mu_R, \mu_F = (0.5, 0.5)$). The total un-
 1048 certainty is calculated by summing the variations in quadrature. We measure a 20% downward
 1049 uncertainty by summing the uncertainties from the 3 variations where the scales are adjusted
 1050 by a factor 0.5 and a 13% upward uncertainty by summing the uncertainties from the 3 varia-
 1051 tions where the scales are adjusted by a factor 2.0.

1052 The size of this uncertainty is independent on the signal models. The measured downward
 1053 uncertainty ranges from 13.2% - 13.5% and the upward uncertainty ranges from 20.3% - 21.0%.
 1054 Therefore, the uncertainty calculated from the sum of all signal models is used.

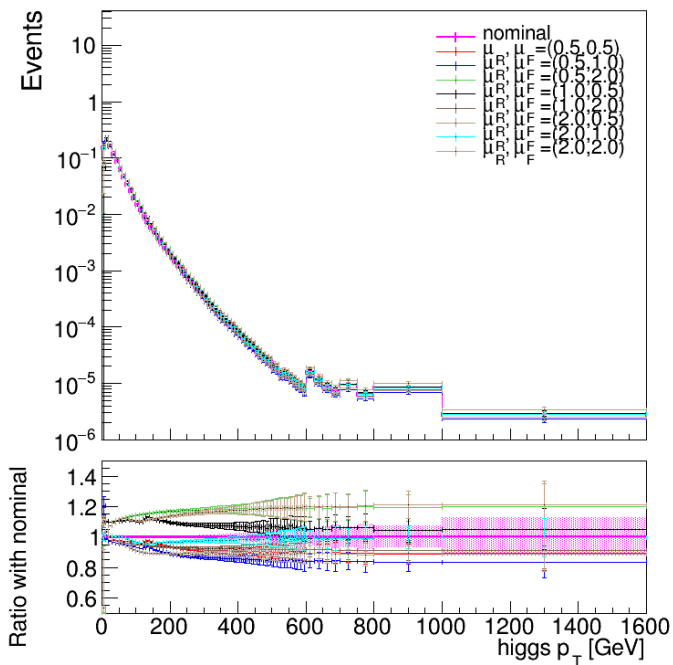


Figure 52: The higgs p_T shape calculated from different renormalization and factorization scale.

1055 8.2.9 Higgs p_T Uncertainty for VBF, VH, and ttH

1056 For the sub-dominant production modes, including VBF, VH, and ttH, the higgs p_T uncertainty
 1057 is calculated by adjusting the renormalization and factorization scale for the sample by a factor
 1058 of 0.5 and 2 and re-evaluating the signal region yield with respect to the nominal signal yield.
 1059 The uncertainty calculated from the 6 variations for all signal model is summed in quadrature,
 1060 resulting in a total uncertainty of a few % in bin D for all production modes. This systematic
 1061 uncertainty is assigned for each production mode independently.

Table 31: Higgs p_T uncertainty in each bin of ABCD plane.

	VBF		WH		qqZH		ggZH		ttH	
	Up	Down	Up	Down	Up	Down	Up	Down	Up	Down
A	2.2%	4.6%	2.6%	7.1%	3.3%	12.5%	12.0%	19.4%	0.7%	1.2%
B	3.2%	15.9%	2.4%	4.0%	1.8%	5.7%	12.3%	19.8%	6.6%	14.8%
C	1.2%	0.7%	0.4%	0.3%	0.6%	1.0%	13.4%	20.8%	1.6%	5.1%
D	1.0%	0.6%	1.8%	5.4%	0.6%	1.7%	13.3%	20.8%	1.0%	2.8%

8.2.10 MC Statistics

The size of this uncertainty depends on the signal model acceptance. The uncertainty is less than 5% in bin C and D for most signal models, and increases to about 10% for a few models with small acceptance. The uncertainty in bin A and bin B is about 7-25%, since there are less signal events in the background enriched regions.

8.3 Impact Plots

The impact plot for one representative signal point is shown in Fig. 53. It can be seen from the plot that the largest contributions come from the two background uncertainties propagated from the two validation regions. They are followed by the dominant signal systematics: higgs p_T shape uncertainty for ggH and the two simulation modeling uncertainties, including the cluster efficiency and cut-based ID efficiency. The result shown here is representative of most signal models explore by this search and is consistent with the expectation of the size of the uncertainty, described in the previous two sub-sections.

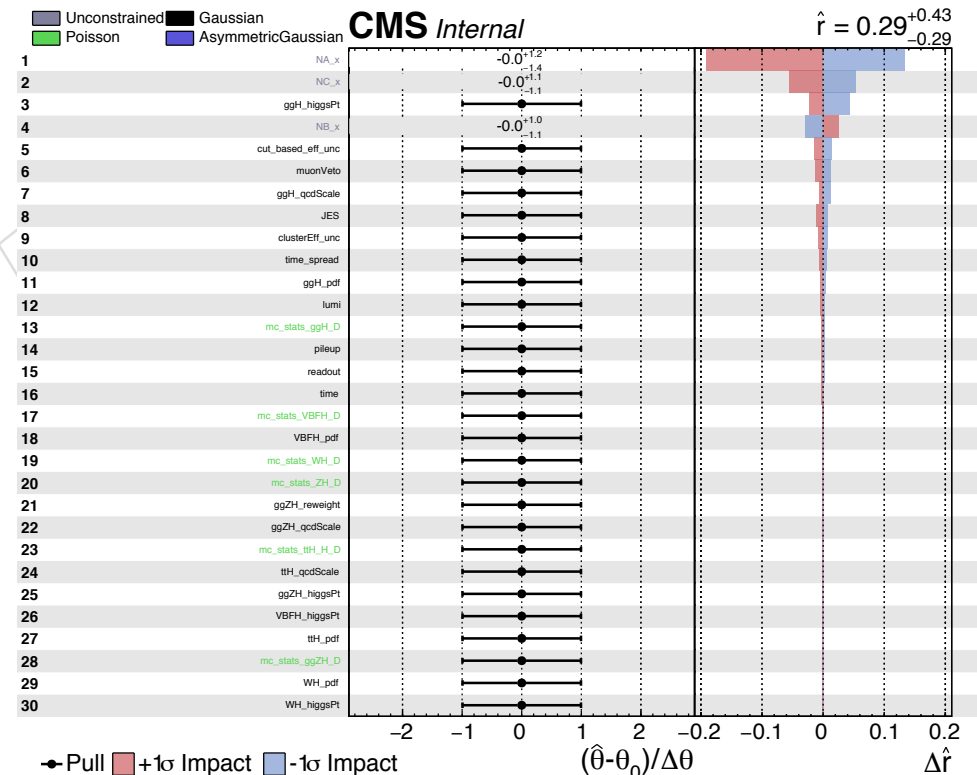


Figure 53: Impact plot for the signal model with LLP mass of 40 GeV, proper lifetime of 1 m, and decaying to 2 b quarks. The signal contribution includes all production modes.

9 Results

We present results of the search in this section.

9.1 Signal Prediction

The expected number of signal events for each production mode, assuming $\text{BR}(\text{H} \rightarrow \text{ss}) = 1\%$ for several LLP masses and proper lifetime $c\tau$ are shown in Table 32. There are more than 20 events for the most sensitive signal points, so it is expected that we are sensitive to exclusion limits at branching ratio below one percent. As shown in Table 32, all the production modes have non-negligible contribution to the total signal prediction. 65% of the signal yield comes from ggH production, 19% from VBF, 7% from WH, 5% from ZH, and 4% from ttH. A 10.5% correction has been applied to the signal prediction, from the discrepancy measured from the jet veto, muon veto, and rechit/segment vetos described in Section 7.

Table 32: Signal Yield in the signal region in binD for different production modes, assuming $\text{BR}(\text{H} \rightarrow \text{ss}) = 1\%$.

ggH				
LLP mass $c\tau$	0.1 m	1 m	10 m	100 m
15 GeV	6.3	21.4	5.1	0.6
40 GeV	0.2	17.4	14.9	1.8
55 GeV	0.0	7.1	18.6	2.8
VBF				
LLP mass $c\tau$	0.1 m	1 m	10 m	100 m
15 GeV	1.9	6.3	1.5	0.1
40 GeV	0.0	5.3	4.4	0.7
55 GeV	0.0	2.2	5.9	0.9
WH				
LLP mass $c\tau$	0.1 m	1 m	10 m	100 m
15 GeV	0.6	2.2	0.5	0.1
40 GeV	0.0	1.7	1.2	0.2
55 GeV	0.0	0.8	1.8	0.2
qZ				
LLP mass $c\tau$	0.1 m	1 m	10 m	100 m
15 GeV	0.3	1.1	0.2	0.0
40 GeV	0.0	1.1	0.8	0.1
55 GeV	0.0	0.5	1.0	0.2
ggZH				
LLP mass $c\tau$	0.1 m	1 m	10 m	100 m
15 GeV	0.1	0.4	0.1	0.0
40 GeV	0.0	0.4	0.3	0.1
55 GeV	0.0	0.1	0.4	0.1
ttH				
LLP mass $c\tau$	0.1 m	1 m	10 m	100 m
15 GeV	0.4	1.5	0.3	0.0
40 GeV	0.0	1.1	0.9	0.1
55 GeV	0.0	0.5	1.2	0.2

1086 **9.2 Signal Contamination**

1087 We have also checked the level of signal contamination in the background-enriched bins A,
 1088 B, and C. The expected number of signal events (including all production modes) in bin A,B
 1089 and C, assuming $\text{BR}(\text{H} \rightarrow \text{ss}) = 1\%$ for several LLP masses and proper lifetime $c\tau$ are shown in
 1090 Table. 33. Assuming the expected BR limits from Fig. 59, the signal contamination in bin A,
 1091 B and C are shown in Table. 34. The signal contamination is small, compared to the expected
 1092 number of predicted background events (See Table. 35).

Table 33: Signal contamination in the signal region in binA, binB and binC, assuming $\text{BR}(\text{H} \rightarrow \text{ss}) = 1\%$.

binA				
LLP mass $c\tau$	0.1 m	1 m	10 m	100 m
15 GeV	0.0	4.3	3.1	0.4
40 GeV	0.0	0.3	1.3	0.2
55 GeV	0.0	0.0	0.2	0.0

binB				
LLP mass $c\tau$	0.1 m	1 m	10 m	100 m
15 GeV	0.0	1.8	1.9	0.4
40 GeV	0.0	0.1	0.4	0.1
55 GeV	0.0	0.0	0.1	0.0

binC				
LLP mass $c\tau$	0.1 m	1 m	10 m	100 m
15 GeV	1.0	8.0	2.3	0.4
40 GeV	0.0	4.4	6.2	0.8
55 GeV	0.0	1.3	7.2	1.3

Table 34: Signal contamination in the signal region in binA, binB and binC, assuming the $\text{BR}(\text{H} \rightarrow \text{ss})$ from the expected limits.

binA				
LLP mass $c\tau$	0.1 m	1 m	10 m	100 m
15 GeV	0.0	0.7	2.6	3.2
40 GeV	0.0	0.1	0.3	0.4
55 GeV	0.0	0.0	0.0	0.1

binB				
LLP mass $c\tau$	0.1 m	1 m	10 m	100 m
15 GeV	0.0	0.3	1.6	3.3
40 GeV	0.0	0.0	0.1	0.2
55 GeV	0.0	0.0	0.0	0.0

binC				
LLP mass $c\tau$	0.1 m	1 m	10 m	100 m
15 GeV	0.5	1.4	2.0	3.4
40 GeV	0.4	0.9	1.5	1.5
55 GeV	0.0	0.6	1.3	1.7

1093 **9.3 Observed Data**

1094 The number of background events predicted from the background-only fit in the signal re-
 1095 gion (in-time region passing the cluster ID) is summarized in Table 35, as well as the observed

1096 yields. With the ABCD method fitted to the observed data, we predict 2.2 ± 1.0 (stat) events
 1097 in the signal-enriched region D, and observe 3 events in the data. We observe no statistically
 1098 significant deviation with respect to the expected number of events.

Table 35: Number of background events in the signal region observed and predicted by the background-only fit using the ABCD method.

	A	B	C	D
Bkg-only fit prediction	4.0 ± 1.9	95.0 ± 9.9	48.0 ± 6.6	2.0 ± 1.0
Observed	3	96	47	3

1099 The observed 2D distributions of $\Delta\phi(\text{cluster}, \text{MET})$ and N_{rechits} is shown in Fig. 54 and the 1D
 distributions of the two variables are shown in Fig. 55.

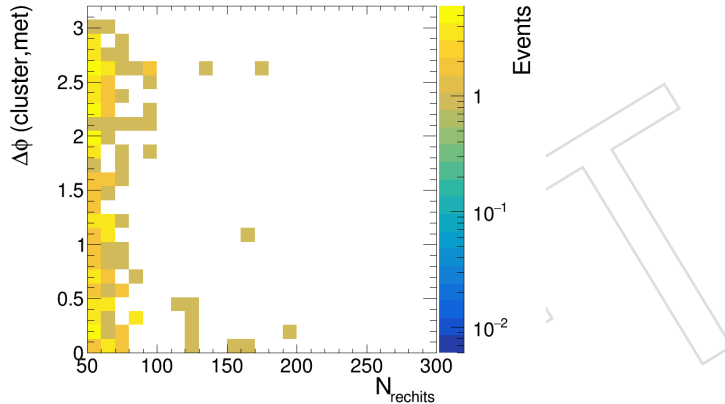


Figure 54: The 2D distribution of $\Delta\phi(\text{cluster}, \text{MET})$ and N_{rechits} is shown.

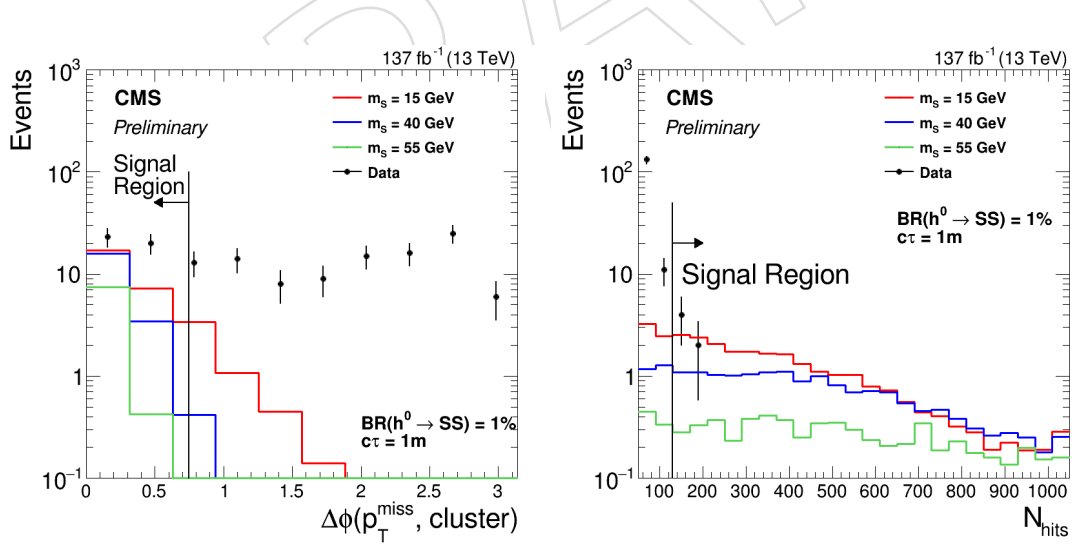


Figure 55: The 1D distributions of $\Delta\phi(\text{cluster}, \text{MET})$ (Left) and N_{rechits} (Right) are shown.

1101 The event display of the 3 events observed in bin D are shown in Fig. 56, Fig. 57, and Fig. 58.

9.4 Expected and Observed Limits

1103 We observe no statistically significant deviation with respect to the expected number of events.
 1104 We set limits on the Higgs boson branching fraction to long-lived scalars, $\text{BR}(H \rightarrow ss)$.

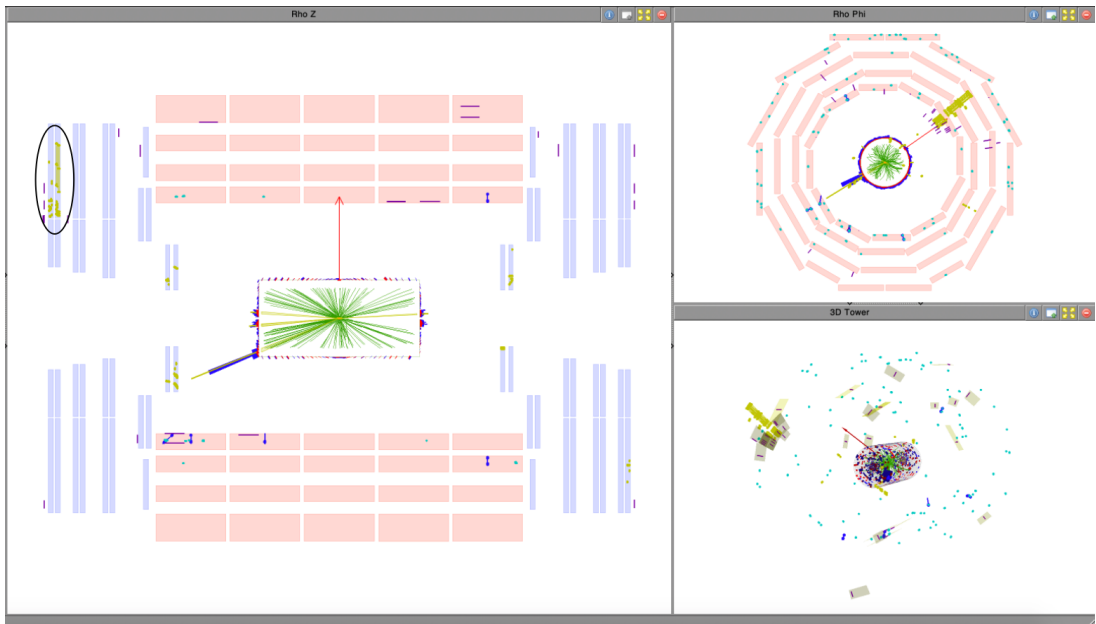


Figure 56: The event display of an observed event in bin D, with run number 317627, lumi section 214, and event number 292396821. The $N_{rechits}$ is 156 and $\Delta\phi(\text{cluster}, \text{MET})$ is 0.01.

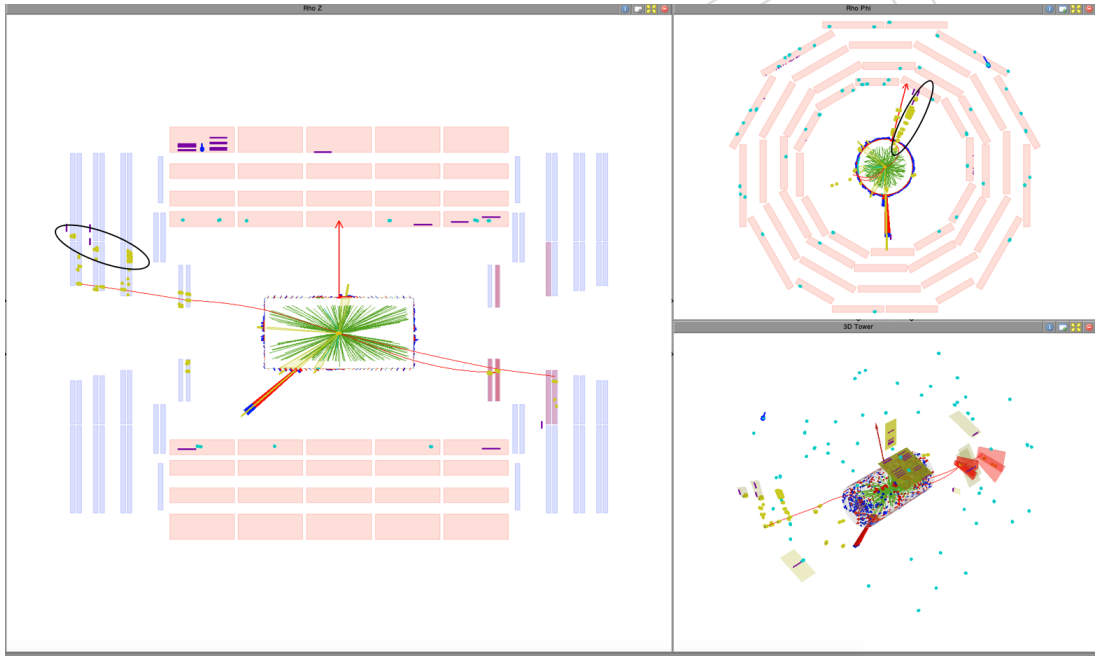


Figure 57: The event display of an observed event in bin D, with run number 324293, lumi section 656, and event number 1224149306. The $N_{rechits}$ is 192 and $\Delta\phi(\text{cluster}, \text{MET})$ is 0.21.

1105 The expected and observed limits are computed based on the background estimation method
 1106 described in Section 6 and performing the maximum likelihood fit expressed in Eq. 5 using
 1107 toys (HybridNew method in the combine tool).

1108 The expected and observed limits on the Higgs decay branching ratio to LLPs is shown in
 1109 Fig. 59, separately for scenarios where each LLP exclusively decays into 2 b quarks, 2 d quarks,
 1110 and 2 τ leptons. The signal contributions of all the available productions are included, including
 1111 ggH, VBF, VH, and ttH.

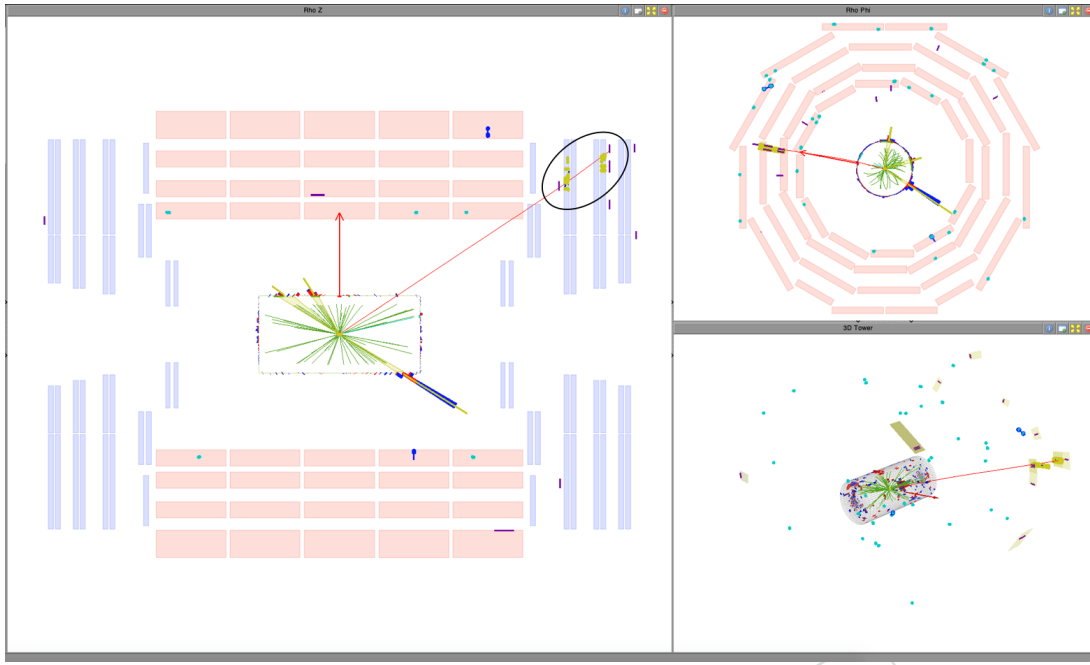


Figure 58: The event display of an observed event in bin D, with run number 275376, lumi section 1901, and event number 2835605820. The N_{rechits} is 169 and $\Delta\phi(\text{cluster}, \text{MET})$ is 0.01. The cluster is matched to a 12 GeV muon, while the muon veto requires a 20 GeV muon.

1112 From Figure 59, we see that the search is approximately independent of the decay modes, as
 1113 the same sensitivity is maintained across different decay modes. The analysis is also sensitive
 1114 to low LLP masses and can be sensitive to LLPs with masses of 7 GeV as well.

1115 We compare the sensitivity of our analysis to the bestpublished limits from ATLAS. Since the
 1116 ATLAS limits assume certain branching ratios of the scalar, we calculate a weighted limit for
 1117 our analysis by reweighting according to the ATLAS branching ratio[44] and substitute the
 1118 $c\bar{c}$ result using our limit. As shown in Fig. 60, the sensitivity of this analysis exceeds the
 1119 sensitivity of the best published ATLAS result for proper lifetime ($c\tau$) above 6, 20, and 40 m, for
 1120 m of 7, 15, and 40 GeV, respectively.

1121 At proper lifetime beyond about 10 m, this analysis outperforms the ATLAS search because the
 1122 ATLAS search selects events with two LLP decays in order to suppress background to negli-
 1123 gible levels, while our search requires only one LLP decay to achieve near zero background.
 1124 The sensitivity of this search also exceeds the sensitivity of the best published ATLAS result
 1125 for proper lifetime below about 0.6 m because of the closer geometric location of the CMS CSC
 1126 muon system to the interaction point compared to the location of the ATLAS muon system.
 1127 For scenarios with large LLP proper lifetime, requiring both LLP to decay within the fiducial
 1128 detector volume significantly limits the acceptance.

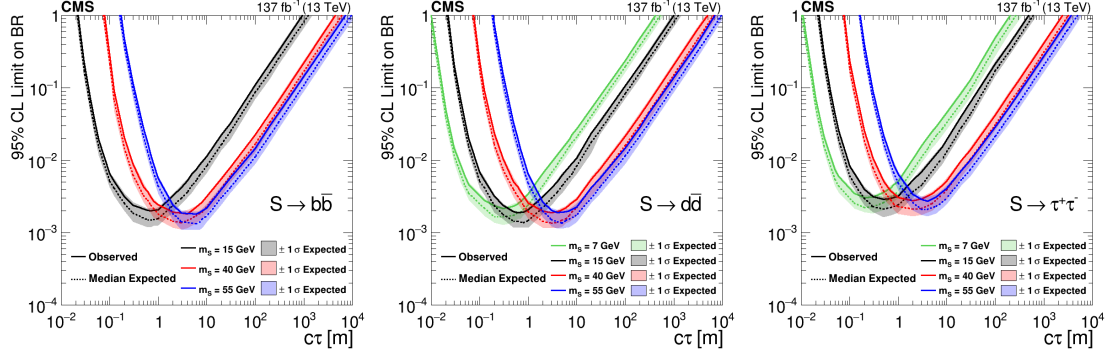


Figure 59: The observed and expected limit for signal predictions that include ggH, VBF, VH, and tH production modes for 4b (Left), 4d (Middle), 4 τ (Right) decay modes are shown. The additional contribution from the sub-dominant production modes increases the signal yield by 54%.

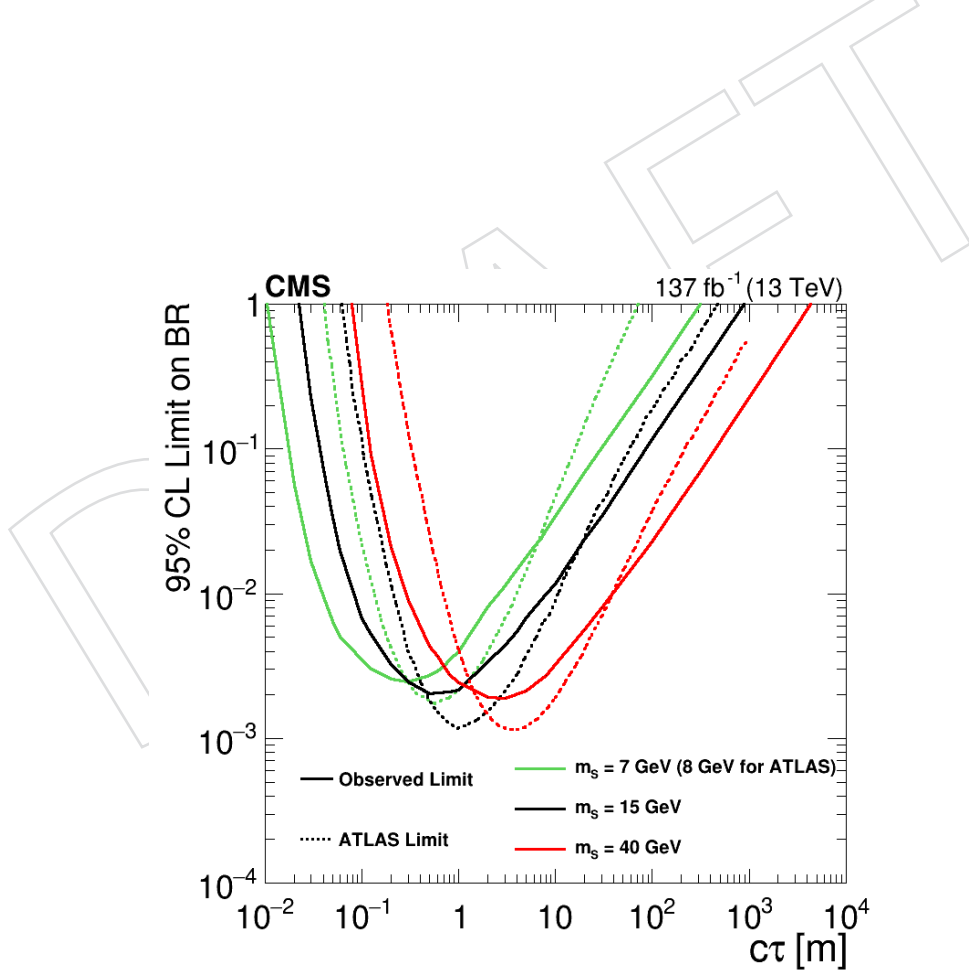


Figure 60: The ATLAS observed limit and the observed limit of this analysis by reweighting according to the branching ratios used by ATLAS.

1129 10 Summary

1130 A search for long-lived particles that decay in the CSC and create showers in the Muon Sys-
1131 tem is performed with full Run2 data, on the pp-collision collected at $\sqrt{s} = 13$ TeV, with an
1132 integrated luminosity of 137 fb^{-1} . Clusters of CSC RecHits with large multiplicity are used
1133 to identify signal events. We use the ABCD method to predict the background in the signal-
1134 enriched region at small values of $\Delta\phi(\text{cluster}, \text{MET})$ and large number of cluster rechits. We
1135 set highly competitive limits on Higgs-mediated production of LLPs decaying to a number of
1136 different hadronic final states at the sub-percent level of Higgs to LLP branching ratio. This
1137 analysis represents the most sensitive search for Higgs-mediated LLP production at the LHC
1138 for proper lifetime ($c\tau$) above 6, 20, and 40 m, for m of 7, 15, and 40 GeV, respectively.

DRAFT

1139 Acknowledgments

1140 References

- 1141 [1] Z. Liu and B. Tweedie, "The fate of long-lived superparticles with hadronic decays after
1142 LHC Run 1", *JHEP* **06** (2015) 042, doi:10.1007/JHEP06(2015)042,
1143 arXiv:1503.05923.
- 1144 [2] G. F. Giudice and A. Romanino, "Split supersymmetry", *Nucl. Phys. B* **699** (2004) 65,
1145 doi:10.1016/j.nuclphysb.2004.08.001, arXiv:hep-ph/0406088. [Erratum:
1146 doi:10.1016/j.nuclphysb.2004.11.048].
- 1147 [3] J. L. Hewett, B. Lillie, M. Masip, and T. G. Rizzo, "Signatures of long-lived gluinos in split
1148 supersymmetry", *JHEP* **09** (2004) 070, doi:10.1088/1126-6708/2004/09/070,
1149 arXiv:hep-ph/0408248.
- 1150 [4] N. Arkani-Hamed, S. Dimopoulos, G. F. Giudice, and A. Romanino, "Aspects of split
1151 supersymmetry", *Nucl. Phys. B* **709** (2005) 3,
1152 doi:10.1016/j.nuclphysb.2004.12.026, arXiv:hep-ph/0409232.
- 1153 [5] P. Gambino, G. F. Giudice, and P. Slavich, "Gluino decays in split supersymmetry", *Nucl.*
1154 *Phys. B* **726** (2005) 35, doi:10.1016/j.nuclphysb.2005.08.011,
1155 arXiv:hep-ph/0506214.
- 1156 [6] A. Arvanitaki, N. Craig, S. Dimopoulos, and G. Villadoro, "Mini-split", *JHEP* **02** (2013)
1157 126, doi:10.1007/JHEP02(2013)126, arXiv:1210.0555.
- 1158 [7] N. Arkani-Hamed et al., "Simply unnatural supersymmetry", (2012).
1159 arXiv:1212.6971.
- 1160 [8] P. Fayet, "Supergauge invariant extension of the Higgs mechanism and a model for the
1161 electron and its neutrino", *Nucl. Phys. B* **90** (1975) 104,
1162 doi:10.1016/0550-3213(75)90636-7.
- 1163 [9] G. R. Farrar and P. Fayet, "Phenomenology of the production, decay, and detection of
1164 new hadronic states associated with supersymmetry", *Phys. Lett. B* **76** (1978) 575,
1165 doi:10.1016/0370-2693(78)90858-4.
- 1166 [10] S. Weinberg, "Supersymmetry at ordinary energies. 1. masses and conservation laws",
1167 *Phys. Rev. D* **26** (1982) 287, doi:10.1103/PhysRevD.26.287.
- 1168 [11] R. Barbier et al., " R -parity violating supersymmetry", *Phys. Rept.* **420** (2005) 1,
1169 doi:10.1016/j.physrep.2005.08.006, arXiv:hep-ph/0406039.
- 1170 [12] G. F. Giudice and R. Rattazzi, "Theories with gauge mediated supersymmetry breaking",
1171 *Phys. Rept.* **322** (1999) 419, doi:10.1016/S0370-1573(99)00042-3,
1172 arXiv:hep-ph/9801271.
- 1173 [13] P. Meade, N. Seiberg, and D. Shih, "General gauge mediation", *Prog. Theor. Phys. Suppl.*
1174 **177** (2009) 143, doi:10.1143/PTPS.177.143, arXiv:0801.3278.
- 1175 [14] M. Buican, P. Meade, N. Seiberg, and D. Shih, "Exploring general gauge mediation",
1176 *JHEP* **03** (2009) 016, doi:10.1088/1126-6708/2009/03/016, arXiv:0812.3668.

- [1177] [15] J. Fan, M. Reece, and J. T. Ruderman, “Stealth supersymmetry”, *JHEP* **11** (2011) 012, doi:10.1007/JHEP11(2011)012, arXiv:1105.5135.
- [1179] [16] J. Fan, M. Reece, and J. T. Ruderman, “A stealth supersymmetry sampler”, *JHEP* **07** (2012) 196, doi:10.1007/JHEP07(2012)196, arXiv:1201.4875.
- [1181] [17] M. J. Strassler and K. M. Zurek, “Echoes of a hidden valley at hadron colliders”, *Phys. Lett. B* **651** (2007) 374, doi:10.1016/j.physletb.2007.06.055, arXiv:hep-ph/0604261.
- [1184] [18] M. J. Strassler and K. M. Zurek, “Discovering the Higgs through highly-displaced vertices”, *Phys. Lett. B* **661** (2008) 263, doi:10.1016/j.physletb.2008.02.008, arXiv:hep-ph/0605193.
- [1187] [19] T. Han, Z. Si, K. M. Zurek, and M. J. Strassler, “Phenomenology of hidden valleys at hadron colliders”, *JHEP* **07** (2008) 008, doi:10.1088/1126-6708/2008/07/008, arXiv:0712.2041.
- [1190] [20] Y. Cui, L. Randall, and B. Shuve, “A WIMPY baryogenesis miracle”, *JHEP* **04** (2012) 075, doi:10.1007/JHEP04(2012)075, arXiv:1112.2704.
- [1192] [21] Y. Cui and R. Sundrum, “Baryogenesis for weakly interacting massive particles”, *Phys. Rev. D* **87** (2013) 116013, doi:10.1103/PhysRevD.87.116013, arXiv:1212.2973.
- [1194] [22] Y. Cui and B. Shuve, “Probing baryogenesis with displaced vertices at the LHC”, *JHEP* **02** (2015) 049, doi:10.1007/JHEP02(2015)049, arXiv:1409.6729.
- [1196] [23] Z. Chacko, H.-S. Goh, and R. Harnik, “Natural electroweak breaking from a mirror symmetry”, *Phys. Rev. Lett.* **96** (2006) 231802, doi:10.1103/PhysRevLett.96.231802, arXiv:hep-ph/0506256.
- [1199] [24] D. Curtin and C. B. Verhaaren, “Discovering uncolored naturalness in exotic Higgs decays”, *JHEP* **12** (2015) 072, doi:10.1007/JHEP12(2015)072, arXiv:1506.06141.
- [1202] [25] H.-C. Cheng, S. Jung, E. Salvioni, and Y. Tsai, “Exotic quarks in twin Higgs models”, *JHEP* **03** (2016) 074, doi:10.1007/JHEP03(2016)074, arXiv:1512.02647.
- [1204] [26] Jingyu Luo, Daniel Marlow, “Search for long-lived particles decaying into displaced jets in 2017+2018 data”, *CMS Physics Analysis Note AN-2019/116* (2019).
- [1206] [27] ATLAS Collaboration, “Search for long-lived particles produced in pp collisions at $\sqrt{s} = 13$ TeV that decay into displaced hadronic jets in the ATLAS muon spectrometer”, *Phys. Rev. D* **99** (2019), no. 5, 052005, doi:10.1103/PhysRevD.99.052005, arXiv:1811.07370.
- [1210] [28] ATLAS Collaboration, “Search for long-lived neutral particles produced in pp collisions at $\sqrt{s} = 13$ TeV decaying into displaced hadronic jets in the ATLAS inner detector and muon spectrometer”, *Phys. Rev. D* **101** (2020), no. 5, 052013, doi:10.1103/PhysRevD.101.052013, arXiv:1911.12575.
- [1214] [29] “Utilities for Accessing Pileup Information for Data”. <https://twiki.cern.ch/twiki/bin/viewauth/CMS/PileupJSONFileforData>.

- 1216 [30] "SM Higgs production cross sections at $\sqrt{s} = 13$ TeV". <https://twiki.cern.ch/twiki/bin/view/LHCPhysics/CERNYellowReportPageAt13TeV>.
- 1217
- 1218 [31] K. Hamilton, P. Nason, E. Re, and G. Zanderighi, "NNLOPS simulation of Higgs boson
1219 production", *JHEP* **10** (2013) 222, doi:10.1007/JHEP10(2013)222,
1220 arXiv:1309.0017.
- 1221 [32] "Baseline muon selections for Run-II".
1222 <https://twiki.cern.ch/twiki/bin/viewauth/CMS/SWGuideMuonIdRun2>.
- 1223 [33] M. Ester, H.-P. Kriegel, J. Sander, and X. Xu, "A density-based algorithm for discovering
1224 clusters in large spatial databases with noise", *Data Mining and Knowledge Discovery*
1225 (1996) 226–231.
- 1226 [34] "Recommended Jet Energy Corrections and Uncertainties for Data and MC".
1227 <https://twiki.cern.ch/twiki/bin/view/CMS/JECDataMC>.
- 1228 [35] "Jet Identification". <https://twiki.cern.ch/twiki/bin/view/CMS/JetID>.
- 1229 [36] CMS Collaboration, "Performance of the CMS muon detector and muon reconstruction
1230 with proton-proton collisions at $\sqrt{s} = 13$ TeV", *JINST* **13** (2018), no. 06, P06015,
1231 doi:10.1088/1748-0221/13/06/P06015, arXiv:1804.04528.
- 1232 [37] CMS Collaboration, "Performance of Electron Reconstruction and Selection with the
1233 CMS Detector in Proton-Proton Collisions at $\sqrt{s} = 8$ TeV", *JINST* **10** (2015), no. 06,
1234 P06005, doi:10.1088/1748-0221/10/06/P06005, arXiv:1502.02701.
- 1235 [38] "Cut-Based Electron Identification Run 2". <https://twiki.cern.ch/twiki/bin/view/CMS/CutBasedElectronIdentificationRun2>.
- 1236
- 1237 [39] "MET Corrections and Uncertainties for Run-II". <https://twiki.cern.ch/twiki/bin/viewauth/CMS/MissingETRun2Corrections>.
- 1238
- 1239 [40] "Official Prescription for calculating corrections and uncertainties on Missing Transverse
1240 Energy (MET)". <https://twiki.cern.ch/twiki/bin/view/CMS/MissingETUncertaintyPrescription>.
- 1241
- 1242 [41] "MET Filter Recommendations for Run II". <https://twiki.cern.ch/twiki/bin/viewauth/CMS/MissingETOptionalFiltersRun2>.
- 1243
- 1244 [42] "CSC Segment Time Reconstruction". <https://github.com/cms-sw/cmssw/blob/master/DataFormats/CSCRecHit/src/CSCSegment.cc#L144-L176>.
- 1245
- 1246 [43] "Luminosity Physics Object Group – Lumi POG".
1247 <https://twiki.cern.ch/twiki/bin/view/CMS/TWikiLUM>.
- 1248
- 1249 [44] "Auxiliary Material for Search for long-lived particles produced in pp collisions at
1250 $\sqrt{s} = 13$ TeV that decay into displaced hadronic jets in the ATLAS muon spectrometer".
1251 <https://atlas.web.cern.ch/Atlas/GROUPS/PHYSICS/PAPERS/EXOT-2017-05/#auxstuff>.
- 1252
- 1253 [45] "Analysis checklist for the pre-approval in the EXO PAG".
1254 <https://twiki.cern.ch/twiki/bin/view/CMS/ExoPreapprovalChecklist>.
- 1255
- 1256 [46] "HEPData record for this analysis".
1257 <https://doi.org/10.17182/hepdata.104408>.

1256 A CSC Rechit Studies

1257 This section details the study performed to validate the use of number of RecHits as a proxy
 1258 to detect the showers created by the LLP decays in the CSC system.

1259 Initially, CSC segments were studied, as they are readily available in AOD datasets. Updates
 1260 to the CSC segment reconstruction for the 2017 and 2018 datasets suppressed the efficiency for
 1261 showering signals. Furthermore, segment reconstruction algorithm is not designed to handle
 1262 showers that have high multiplicity, as it's only designed to reconstruct segments from muons
 1263 that leave only a few tracks. We find that for the segment reconstruction in 2016, as shown
 1264 in the signal event display in Fig. 61, where there are 1100 RecHits, but only 33 segments are
 1265 reconstructed.

1266 Therefore, we used RecHits and performed a study on the saturation of our shower signals for
 1267 the RecHits reconstruction and showed that the RecHits can be used to reflect the number of
 1268 simulated hits from the signal showers and provide much better discrimination power than
 1269 segments.

1270 To be able to study how the simulated hits from the LLPs are reconstructed to RecHits, we
 1271 needed access to collections that are saved in various steps of the production process, including:
 1272 MuonCSCHits(simulated hits/SimHits), MuonCSCStripDigi, MuonCSCWireDigi, and CSCRe-
 1273 cHit2DCollection(RecHits). We ran the step2 reconstruction, which reconstructs the RecHits
 1274 and segments and an ntupler step together on the Digi-Reco step1 samples, which contains
 1275 SimHits and Digits, such that we have access to all the collections mentioned above in a single
 1276 set of ntuples.

1277 We studied the correlation between the number of SimHits and RecHits for events where at
 1278 least 1 LLP decayed in the CSC and observed strong correlation between the two variables up
 1279 to 600 $N_{simhits}$, as shown in Fig. 62. We further observed that it is extremely rare for background
 1280 events to have number of simulated hits to be above 600, as shown in Fig. 63.

1281 Therefore, we use the number of RecHits as a proxy to detect the showering signal with large
 1282 number of SimHits for this analysis.

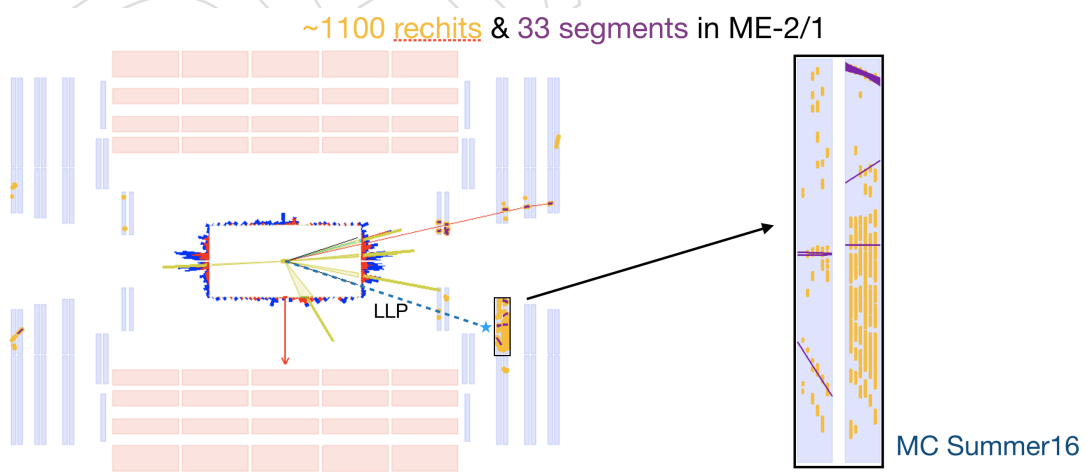


Figure 61: An event display of a signal event. There are 1100 rechits but only 33 segments reconstructed. Rechits provide much better discrimination between signal and background.

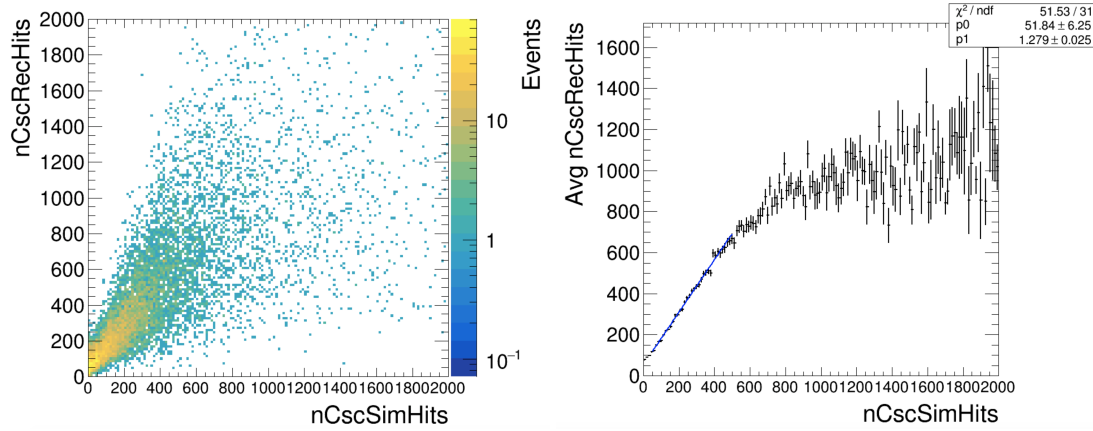


Figure 62: The correlation between the number of Rechits and Simhits (Left) and the profileX of the 2D plot (Right). The number of simulated hits and reconstructed hits are linear up to $N_{\text{simhits}} = 600$.

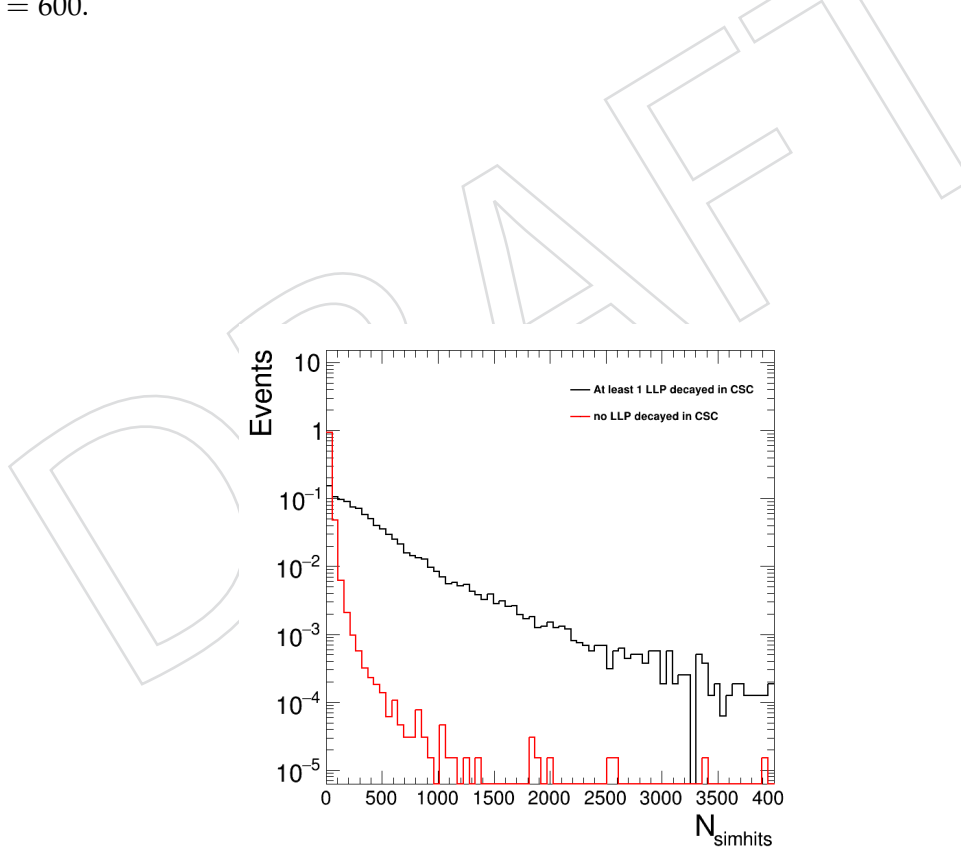


Figure 63: Number of simulated hits per event for events with at least 1 LLP decay in CSC (signal) and for events with LLP decay close to the interaction point (background-like events in the signal sample) is shown.

B Era Comparison

In this section, we show the signal efficiency plots, signal and data cut flow table for different eras. We will demonstrate that the overall signal efficiency is independent of the detector condition in different eras, although certain cuts are dependent on the pileup condition. Furthermore, we show from the data cut flow table, the efficiency of the vetos are similar in different eras.

B.1 Signal Efficiency Plots

In this section, we will demonstrate that the cluster efficiency, efficiency of the signal selections, and the $N_{rechits}$ cut efficiency are independent of the detector condition in different eras.

The cluster efficiency, as defined in subsection 4.1, with respect to the LLP decay position for different conditions are shown in Fig. 64. Good agreement is observed for 2016, 2017, and 2018 condition.

The signal efficiency of the clustering efficiency and all the cluster-level cuts described in Section 5, except for the two selections that define the boundary of the ABCD plane($\Delta\phi(\text{cluster}, \text{MET})$ and $N_{rechits}$), with respect to the LLP decay position is shown in Fig. 65 for different conditions. Good agreement between different years are observed.

The signal efficiency of the cut $N_{rechits} \geq 130$ with respect to clusters passing all the other cluster-level cuts presented in Section 5, except for $\Delta\phi(\text{cluster}, \text{MET}) < 0.75$ is shown in Fig. 66 for different detector conditions. It can be seen from the figure, that the efficiency of this cut is the same for 2016, 2017, and 2018 condition.

B.2 Signal Cut Flow Table

In this section, we present the signal cut flow table for different conditions for LLP mass of 40 GeV, decaying to 2 b quarks. The cut flow tables for run condition in 2016, 2017, and 2018 are shown in Table 36, Table 37, and Table 38. It can be seen from the tables, the jet veto and the rechit vetos are less efficiency in 2017 and 2018, as the number of pileup increases. However, the overall cumulative signal efficiency is independent of the run condition, as we expected from the agreement observed in Section. B.1.

B.3 Data Cut Flow Table for Individual Years

The cut flow tables for data in 2016, 2017, and 2018 are shown in Table 39, Table 40, and Table 41.

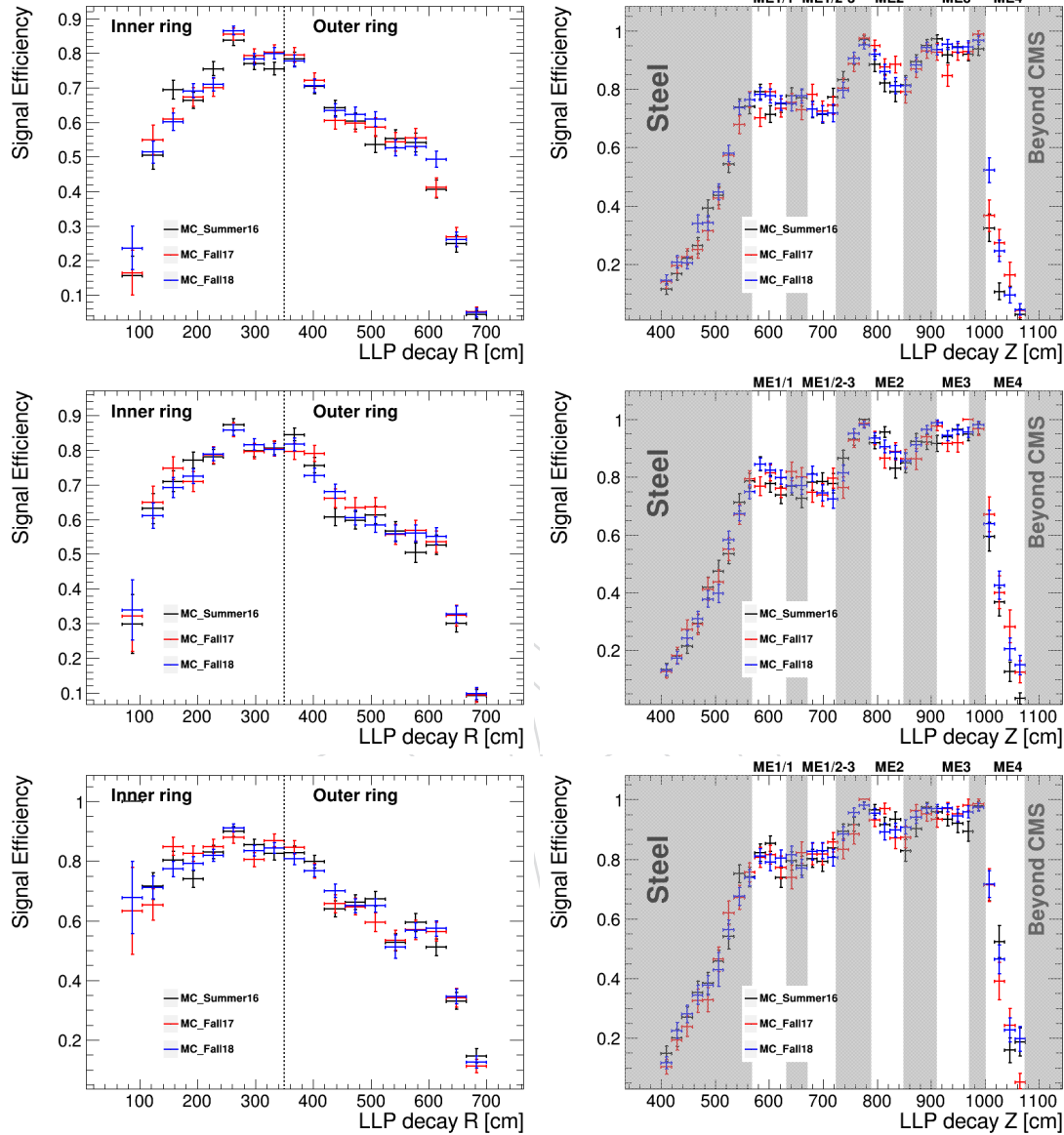


Figure 64: The “clustering efficiency”, defined as the fraction of LLPs in signal events that decay within the CSC geometric acceptance region and produce a successfully reconstructed cluster is shown as a function of the LLP decay position in the radial direction (left) and the Z direction (right). Scenarios with LLP mass of 15 (Top), 40 (Middle), and 55 GeV (Bottom) are shown separately for the different detector conditions. The signal sample for each LLP mass includes the sum of all available lifetimes.

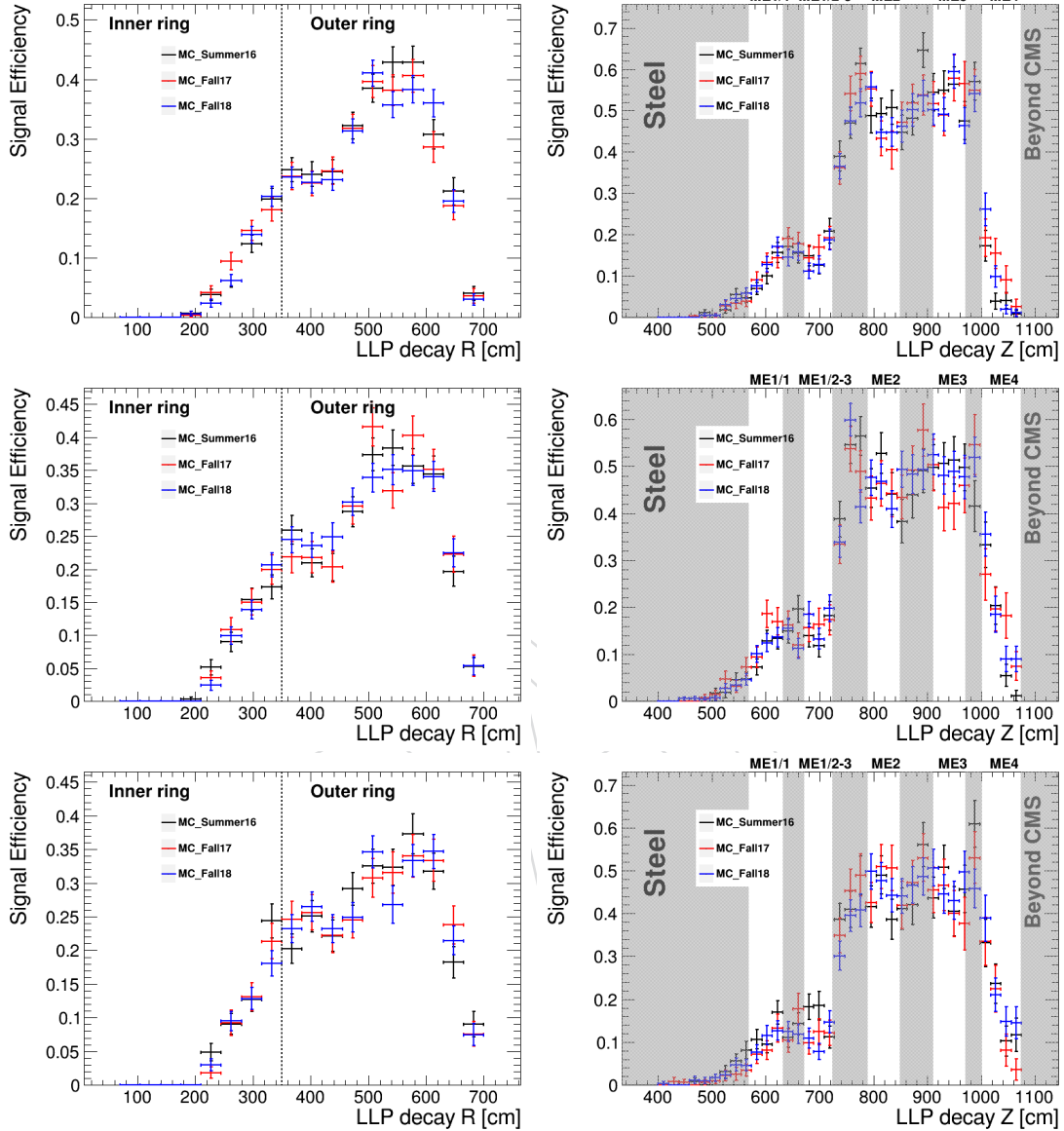


Figure 65: The signal efficiency of the selections with respect to the LLP decay position in the radial direction (Left) and the LLP decay position in the Z direction (Right) is shown. The nominator clusters are required to pass all cluster-level cuts, except for $\Delta\phi(\text{cluster}, \text{MET})$ and N_{rechits} , while the denominator consists of any LLP that decays in the CSC volume. Similar trend is observed for 2016, 2017, and 2018 conditions. The signal sample for each LLP mass includes the sum of all available lifetimes.

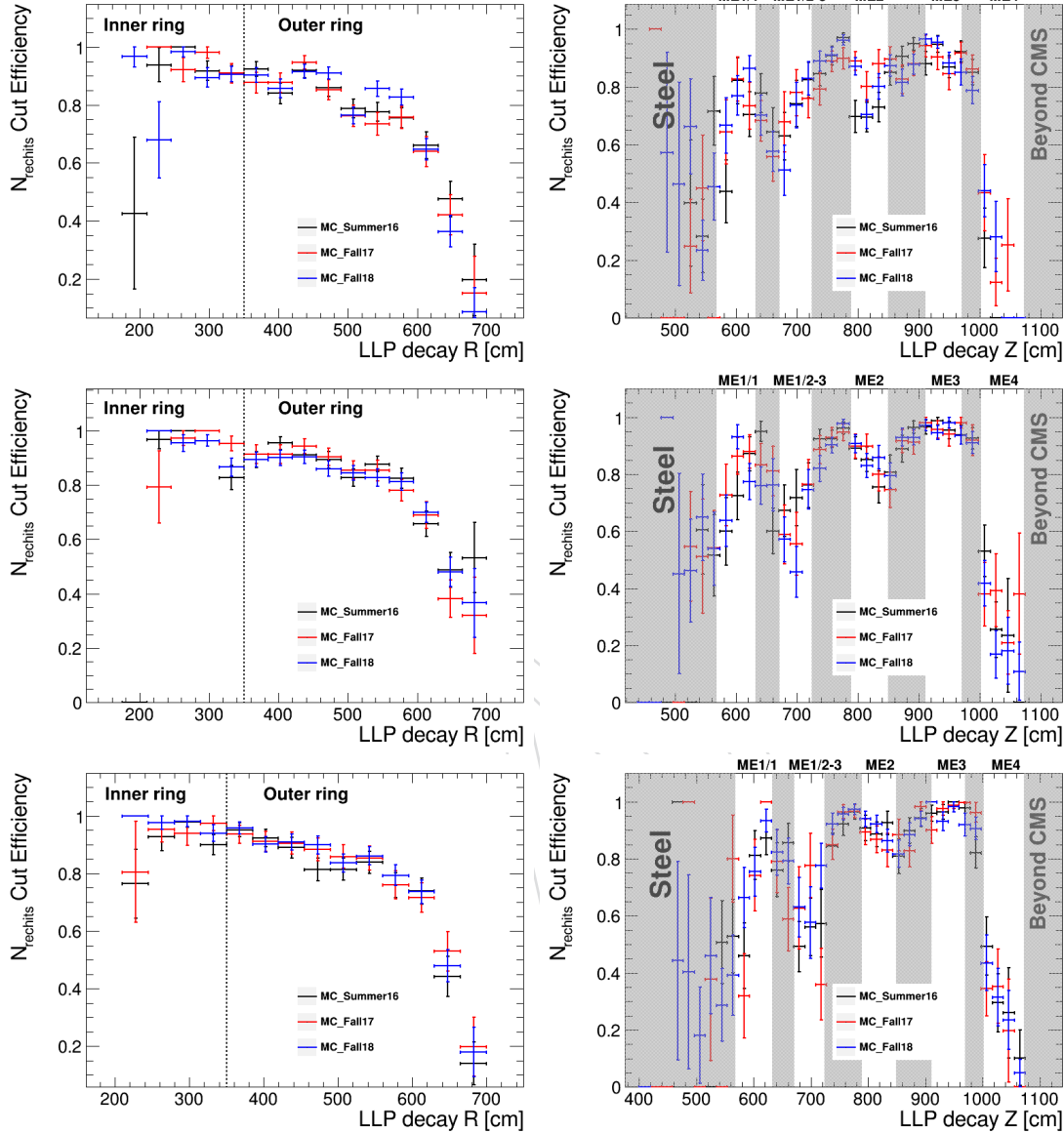


Figure 66: The signal efficiency of the cut $N_{\text{recHits}} \geq 130$ with respect to the LLP decay position in the radial direction (Left) and the LLP decay position in the Z direction (Right) is shown. The denominator clusters are required to pass all cluster-level cuts, except for $\Delta\phi(\text{cluster}, \text{MET})$ and N_{recHits} , satisfying the same set of requirements as the nominator clusters in Fig. 65. Nominator clusters are required to pass the $N_{\text{recHits}} \geq 130$ cut, in addition to the denominator requirements. Similar trend is observed for 2016, 2017, and 2018 conditions. The signal sample for each LLP mass includes the sum of all available lifetimes.

Table 36: Signal Efficiency(%) of each cut for LLP mass 40 GeV and decaying to 2 b quarks in 2016 run condition. (Cumulative Efficiency for all cuts applied after Trigger and MET cut are calculated with respect to events in acceptance and pass the MET and trigger cut and cut efficiency is calculated with respect to the previous cut. Acceptance is defined as when at least one LLP decays inside CSC.)

Selection	$c\tau = 0.1m$		$c\tau = 1m$		$c\tau = 10m$		$c\tau = 100m$	
	cut eff	cumulative eff	cut eff	cumulative eff	cut eff	cumulative eff	cut eff	cumulative eff
Acceptance	0.091	0.091	17.163	17.163	20.235	20.235	3.303	3.303
Trigger and MET cut	8.348	0.008	1.059	0.182	0.781	0.158	0.696	0.023
MET filters	96.00	96.00	95.86	95.86	98.71	98.71	98.67	98.67
$N_{lepton} = 0$	100.00	96.00	99.65	95.52	99.79	98.50	99.56	98.24
$N_{jet} \geq 1$	99.12	95.15	96.51	92.19	94.97	93.54	95.12	93.44
$N_{CSC+DT\ rings} \leq 10$	100.00	95.15	100.00	92.19	100.00	93.54	100.00	93.44
$N_{cluster} \geq 1$	89.83	85.48	73.36	67.63	62.13	58.12	55.55	51.91
muon veto	95.43	81.57	92.99	62.89	92.75	53.90	94.23	48.91
jet veto	62.85	51.27	86.28	54.26	89.55	48.27	90.93	44.48
Time cut	100.00	51.27	100.00	54.26	96.84	46.74	93.61	41.64
ME1/1 veto	47.60	24.40	83.67	45.40	88.98	41.59	86.31	35.94
ME1/2 veto	71.80	17.52	69.38	31.50	70.45	29.30	69.89	25.11
RE1/2 veto	100.00	17.52	96.82	30.50	98.42	28.84	99.96	25.10
MB1 veto	96.75	16.95	94.95	28.96	96.24	27.76	98.12	24.63
RB1 veto	100.00	16.95	96.80	28.03	97.11	26.96	95.61	23.55
η cut	32.22	5.46	80.76	22.64	88.29	23.80	84.66	19.94
time spread cut	100.00	5.46	98.99	22.41	99.09	23.58	96.54	19.25
cut-based ID	89.18	4.87	87.84	19.68	91.33	21.54	89.24	17.18
$\Delta\phi(\text{cluster, MET})$	100.00	4.87	99.08	19.50	97.52	21.00	94.49	16.23
$N_{rechits}$ cut	86.26	4.20	86.69	16.90	82.15	17.25	76.20	12.37

Table 37: Signal Efficiency(%) of each cut for LLP mass 40 GeV and decaying to 2 b quarks in 2017 run condition. (Cumulative Efficiency for all cuts applied after Trigger and MET cut are calculated with respect to events in acceptance and pass the MET and trigger cut and cut efficiency is calculated with respect to the previous cut. Acceptance is defined as when at least one LLP decays inside CSC.)

Selection	$c\tau = 0.1m$		$c\tau = 1m$		$c\tau = 10m$		$c\tau = 100m$	
	cut eff	cumulative eff	cut eff	cumulative eff	cut eff	cumulative eff	cut eff	cumulative eff
Acceptance	0.087	0.087	17.097	17.097	20.319	20.319	3.330	3.330
Trigger and MET cut	7.487	0.007	0.999	0.171	0.698	0.142	0.590	0.020
MET filters	96.85	96.85	96.59	96.59	99.23	99.23	99.39	99.39
$N_{lepton} = 0$	99.57	96.44	99.44	96.05	99.73	98.96	99.75	99.15
$N_{jet} \geq 1$	96.84	93.39	95.23	91.47	94.11	93.14	92.43	91.64
$N_{CSC+DT\ rings} \leq 10$	100.00	93.39	100.00	91.47	100.00	93.14	100.00	91.64
$N_{cluster} \geq 1$	91.31	85.27	73.25	67.00	61.67	57.44	60.11	55.08
muon veto	93.90	80.07	94.41	63.26	94.91	54.51	96.50	53.15
jet veto	63.64	50.95	82.08	51.92	89.30	48.68	88.09	46.82
Time cut	100.00	50.95	99.71	51.77	96.87	47.16	91.57	42.87
ME1/1 veto	47.38	24.14	80.80	41.83	87.54	41.28	85.93	36.84
ME1/2 veto	69.28	16.72	68.73	28.75	73.68	30.41	65.04	23.96
RE1/2 veto	100.00	16.72	96.81	27.84	98.10	29.84	99.93	23.95
MB1 veto	100.00	16.72	95.89	26.69	97.55	29.11	99.15	23.74
RB1 veto	100.00	16.72	95.55	25.50	96.67	28.13	97.78	23.21
η cut	62.76	10.50	82.00	20.91	89.61	25.21	92.88	21.56
time spread cut	92.04	9.66	99.02	20.71	98.97	24.95	98.79	21.30
cut-based ID	62.61	6.05	92.28	19.11	92.40	23.05	87.04	18.54
$\Delta\phi(\text{cluster, MET})$	100.00	6.05	100.00	19.11	95.87	22.10	96.98	17.98
$N_{rechits}$ cut	100.00	6.05	87.83	16.78	80.98	17.90	77.63	13.96

Table 38: Signal Efficiency(%) of each cut for LLP mass 40 GeV and decaying to 2 b quarks in 2018 run condition. (Cumulative Efficiency for all cuts applied after Trigger and MET cut are calculated with respect to events in acceptance and pass the MET and trigger cut and cut efficiency is calculated with respect to the previous cut. Acceptance is defined as when at least one LLP decays inside CSC.)

Selection	$c\tau = 0.1m$		$c\tau = 1m$		$c\tau = 10m$		$c\tau = 100m$	
	cut eff	cumulative eff	cut eff	cumulative eff	cut eff	cumulative eff	cut eff	cumulative eff
Acceptance	0.087	0.087	17.065	17.065	20.389	20.389	3.327	3.327
Trigger and MET cut	8.716	0.008	0.990	0.169	0.690	0.141	0.655	0.022
MET filters	99.34	99.34	97.70	97.70	99.59	99.59	100.00	100.00
$N_{lepton} = 0$	99.70	99.04	99.50	97.21	99.78	99.37	99.62	99.62
$N_{jet} \geq 1$	96.96	96.04	95.23	92.57	94.83	94.23	94.71	94.35
$N_{CSC+DT \text{ rings}} \leq 10$	100.00	96.04	100.00	92.57	100.00	94.23	100.00	94.35
$N_{cluster} \geq 1$	91.87	88.23	73.88	68.39	61.91	58.34	57.70	54.44
muon veto	96.01	84.71	94.44	64.58	94.88	55.35	93.55	50.92
jet veto	54.63	46.28	80.98	52.30	86.49	47.88	85.84	43.71
Time cut	100.00	46.28	99.79	52.19	96.47	46.19	92.52	40.45
ME1/1 veto	45.54	21.07	81.04	42.30	87.43	40.38	85.21	34.47
ME1/2 veto	61.96	13.06	69.75	29.50	70.64	28.53	76.91	26.51
RE1/2 veto	100.00	13.06	97.64	28.81	98.13	27.99	97.81	25.93
MB1 veto	97.17	12.69	92.98	26.78	95.73	26.80	94.16	24.41
RB1 veto	100.00	12.69	96.27	25.78	97.55	26.14	96.18	23.48
η cut	31.28	3.97	85.60	22.07	91.08	23.81	93.33	21.91
time spread cut	100.00	3.97	98.99	21.85	99.22	23.62	96.79	21.21
cut-based ID	59.23	2.35	88.91	19.43	93.69	22.13	88.16	18.70
$\Delta\phi(\text{cluster, MET})$	100.00	2.35	99.19	19.27	95.68	21.18	96.01	17.95
$N_{rechits}$ cut	100.00	2.35	88.67	17.09	77.38	16.39	82.43	14.80

Table 39: Efficiency(%) of each cut for 2016 data.

Selection	cut eff	cumulative eff	Number of events
MET filters	89.79	89.79	2168274
$N_{lepton} = 0$	87.30	78.38	1892923
$N_{jet} \geq 1$	94.71	74.23	1792717
$N_{CSC+DT \text{ rings}} \leq 10$	100.00	74.23	1792682
$N_{cluster} \geq 1$	5.06	3.75	90639
muon veto	56.49	2.12	51202
jet veto	51.01	1.08	26118
Time cut	29.98	0.32	7830
ME1/1 veto	15.94	0.052	1248
ME1/2 veto	42.55	0.022	531
RE1/2 veto	99.25	0.022	527
MB1 veto	97.15	0.021	512
RB1 veto	99.41	0.021	509
η cut	18.07	0.004	92
time spread cut	73.91	0.003	68
cut-based ID	35.29	0.001	24
$\Delta\phi(\text{cluster, MET})$	41.67	0.0004	10
$N_{rechits}$ cut	10.00	0.00004	1

Table 40: Efficiency(%) of each cut for 2017 data.

Selection	cut eff	cumulative eff	Number of events
MET filters	90.34	90.34	3120841
$N_{lepton} = 0$	89.86	81.18	2804332
$N_{jet} \geq 1$	78.92	64.07	2213129
$N_{CSC+DT \text{ rings}} \leq 10$	100.00	64.06	2213119
$N_{cluster} \geq 1$	6.06	3.88	134078
muon veto	67.10	2.60	89960
jet veto	53.70	1.40	48307
Time cut	28.06	0.39	13556
ME1/1 veto	12.67	0.050	1718
ME1/2 veto	45.98	0.023	790
RE1/2 veto	99.37	0.023	785
MB1 veto	98.09	0.022	770
RB1 veto	99.74	0.022	768
η cut	20.31	0.005	156
time spread cut	80.77	0.004	126
cut-based ID	30.16	0.001	38
$\Delta\phi(\text{cluster}, \text{MET})$	44.74	0.0005	17
$N_{rechits}$ cut	0.00	0.00000	0

Table 41: Efficiency(%) of each cut for 2018 data.

Selection	cut eff	cumulative eff	Number of events
MET filters	94.40	94.40	7797428
$N_{lepton} = 0$	93.11	87.90	7260297
$N_{jet} \geq 1$	77.88	68.46	5654426
$N_{CSC+DT \text{ rings}} \leq 10$	100.00	68.46	5654426
$N_{cluster} \geq 1$	9.71	6.65	549071
muon veto	61.21	4.07	336088
jet veto	44.96	1.83	151117
Time cut	25.50	0.47	38532
ME1/1 veto	10.99	0.051	4235
ME1/2 veto	46.49	0.024	1969
RE1/2 veto	99.19	0.024	1953
MB1 veto	98.41	0.023	1922
RB1 veto	99.74	0.023	1917
η cut	22.22	0.005	426
time spread cut	71.60	0.004	305
cut-based ID	28.52	0.001	87
$\Delta\phi(\text{cluster}, \text{MET})$	26.44	0.0003	23
$N_{rechits}$ cut	8.70	0.00002	2

1312 C Issues in Run2 Data Taking

1313 C.1 L1 EE Pre-firing

1314 In 2016 and 2017, the ECAL endcap was pre-firing at L1, resulting in inefficiencies in the data
 1315 taking. As a result, we follow the recommended procedure to check if this analysis is af-
 1316 fected by the pre-firing issue. Following the recommended procedure to check in the EXO Pre-
 1317 Approval checklist[45], we check in MC signal samples (2016 and 2017 condition) the change
 1318 in shape and cut efficiency of $N_{rechits}$ and $\Delta\phi(\text{cluster}, \text{MET})$ by removing events with jets with
 1319 $p_T > 100 \text{ GeV}$ and $2.25 < |\eta| < 3.0$. As the analysis uses mostly the CSC system, we do not
 1320 expect and do not observe any significant change from this issue.

1321 The change in signal efficiency of $N_{rechits} \geq 130$ is shown in Table. 42 and the change in cut
 1322 efficiency of $\Delta\phi(\text{cluster}, \text{MET}) < 0.75$ is shown in Table. 43. For both variables, we observe that
 1323 the change in signal efficiency is at most 1% for all signal points. Furthermore, we observed no
 1324 significant changes in shape for both variables. The shape of $N_{rechits}$ and $\Delta\phi(\text{cluster}, \text{MET})$ for
 1325 signal samples with LLP mass of 15 GeV are shown in Fig. 67 and Fig. 68 as an example.

1326 Since the change in signal efficiency is at most 1%, no additional corrections are needed to
 1327 mitigate the issue.

Table 42: Change in $N_{rechits}$ cut Efficiency

	$c\tau = 0.1\text{m}$	$c\tau = 1\text{m}$	$c\tau = 10\text{m}$	$c\tau = 100\text{m}$
15 GeV	0.05%	0.03%	1.16%	0.78%
40 GeV	1.06%	0.22%	0.62%	2.20%
55 GeV	\	0.02%	0.21%	1.15%

Table 43: Change in $\Delta\phi(\text{cluster}, \text{MET})$ cut Efficiency

	$c\tau = 0.1\text{m}$	$c\tau = 1\text{m}$	$c\tau = 10\text{m}$	$c\tau = 100\text{m}$
15 GeV	0.0%	0.14%	0.04%	0.48%
40 GeV	0.0%	0.06%	0.18%	0.67%
55 GeV	\	0.0%	0.0%	0.0%

1328 C.2 HEM15/16 Failure

1329 Starting from run 3109077 (toward the end of 2018B) until the end of 2018 run, two modules
 1330 of the ECAL endcap, HEM15 and HEM16 were effectively off, due to power interruptions.
 1331 The affected region is $-3.0 < \eta < -1.3$ and $-1.57 < \phi < -0.87$. To estimate the impact of this
 1332 issue on the signal yield prediction, we remove all jets that fall in the problematic region, and
 1333 recompute the predicted signal yield in bin D of the ABCD plane using signal simulations in
 1334 2018 condition. The variation in the signal prediction is 3% for all signal models, thus the
 1335 impact on the total signal yield is less than 1%, given the luminosity ratio of the problematic
 1336 period and the entire Run2 period.

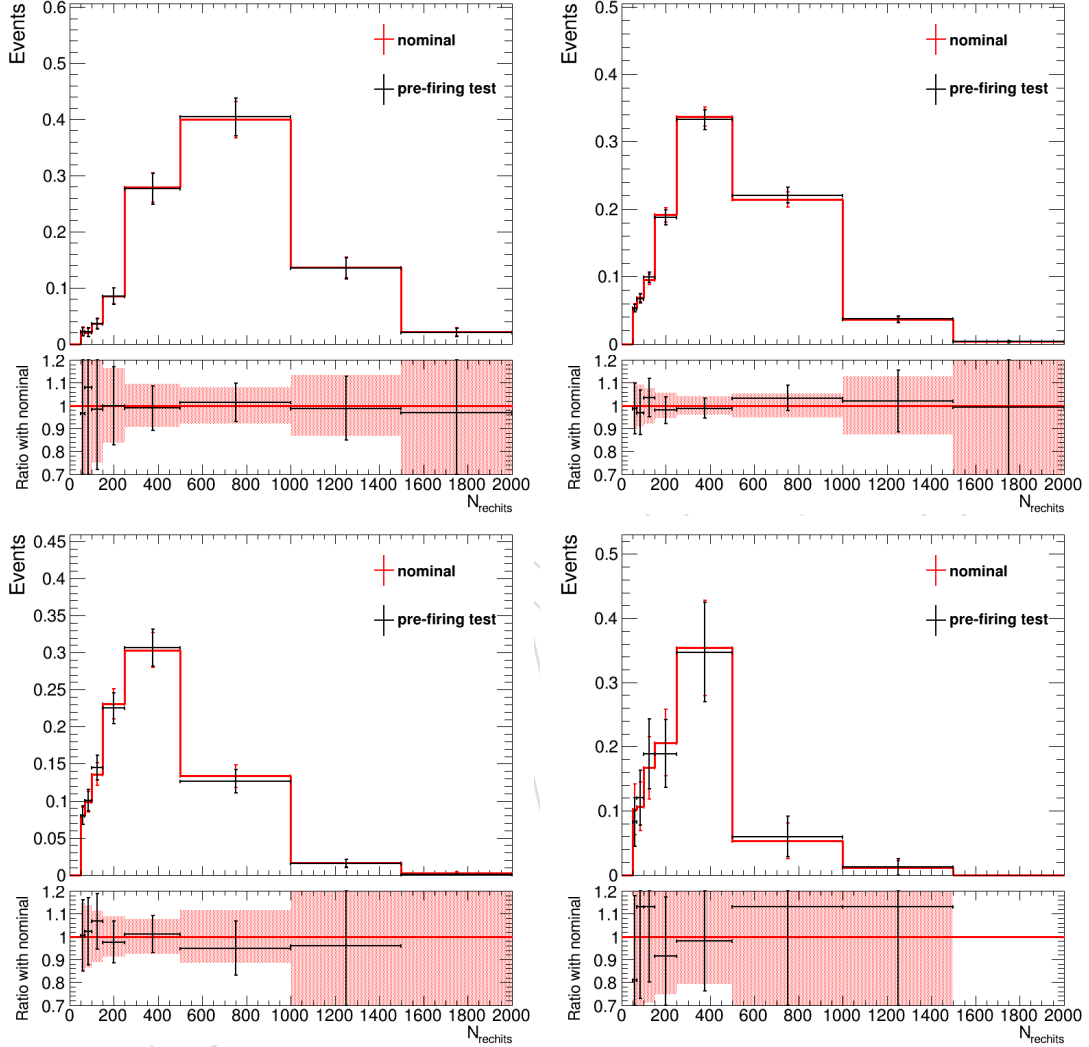


Figure 67: The normalized N_{rechits} distributions for MC signal samples with LLP mass of 15 GeV and proper life time of 0.1 m (Top Left), 1 m (Top Right), 10 m (Bottom Left), 100m (Bottom Right) is shown. The shape of with nominal selection and with event removal that have jets in the problematic region is shown. No significant change is observed between the two shapes.

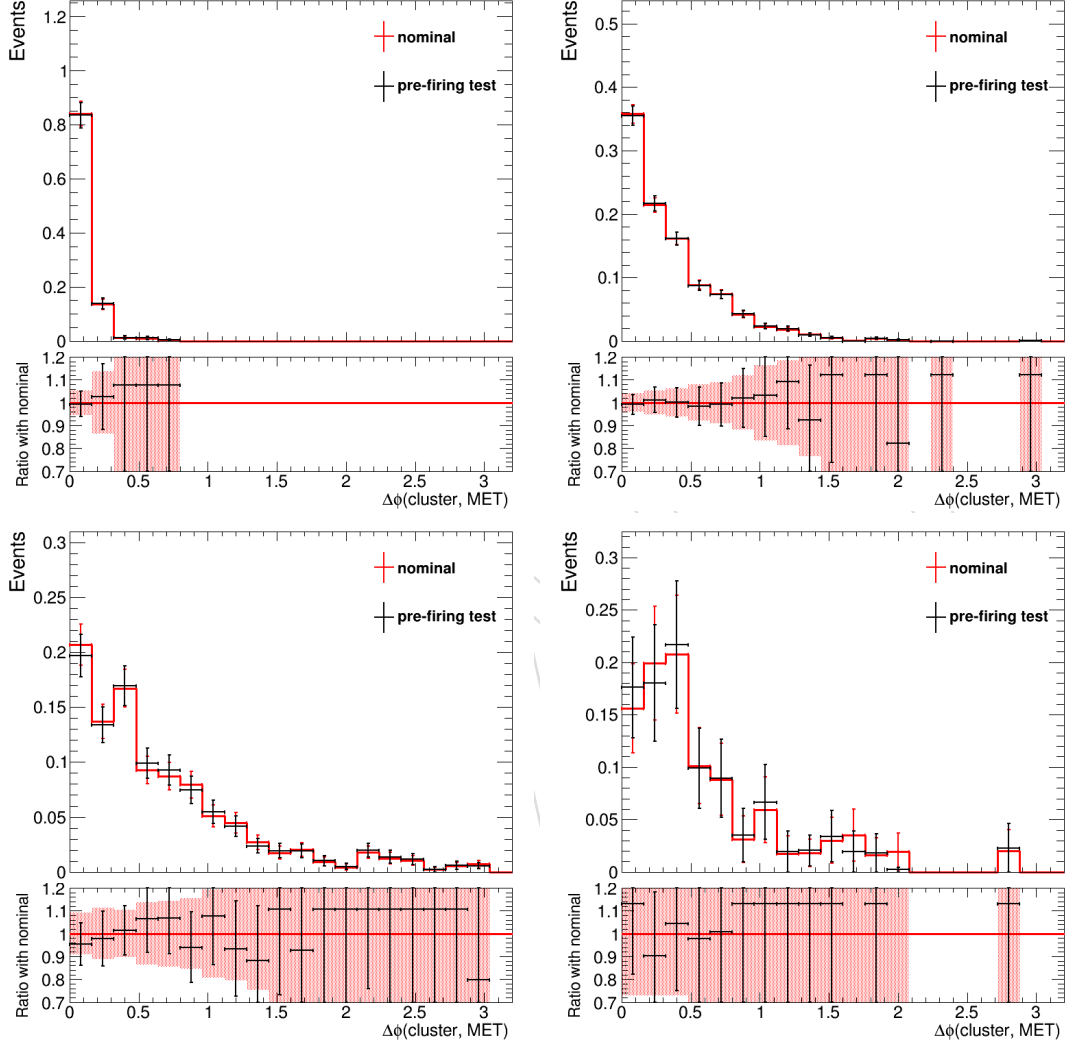


Figure 68: The normalized $\Delta\phi(\text{cluster}, \text{MET})$ distributions for MC signal samples with LLP mass of 15 GeV and proper life time of 0.1 m (Top Left), 1 m (Top Right), 10 m (Bottom Left), 100m (Bottom Right) is shown. The shape of with nominal selection and with event removal that have jets in the problematic region is shown. No significant change is observed between the two shapes.

D Signal Cut Flow Table for 4 d and 4 τ Decay Modes

The signal efficiency of all the selections applied is shown for the gluon-fusion production mode and 4d decay mode, for LLP mass 7, 15, 40, and 55 GeV in Table 44, Table 45, 46, and 47, respectively.

The signal efficiency of all the selections applied is shown for the gluon-fusion production mode and 4 τ decay mode, for LLP mass 7, 15, 40, and 55 GeV in Table 48, Table 49, 50, and 51, respectively.

Table 44: Signal Efficiency(%) of each cut for LLP mass 7 GeV and decaying to 4 d quarks. (Cumulative Efficiency for all cuts applied after Trigger and MET cut are calculated with respect to events in acceptance and pass the MET and trigger cut and cut efficiency is calculated with respect to the previous cut. Acceptance is defined as when at least one LLP decays inside CSC.)

Selection	$c\tau = 0.1m$		$c\tau = 1m$		$c\tau = 10m$		$c\tau = 100m$	
	cut eff	cumulative eff	cut eff	cumulative eff	cut eff	cumulative eff	cut eff	cumulative eff
Acceptance	10.672	10.672	23.376	23.376	4.523	4.523	0.495	0.495
Trigger and MET cut	1.248	0.133	0.849	0.199	0.971	0.044	1.034	0.005
MET filters	96.24	96.24	98.55	98.55	99.19	99.19	99.73	99.73
$N_{lepton} = 0$	99.51	95.77	99.55	98.11	99.56	98.75	99.51	99.24
$N_{jet} \geq 1$	95.64	91.60	94.99	93.19	95.25	94.06	95.29	94.56
$N_{CSC+DT\ rings} \leq 10$	100.00	91.60	100.00	93.19	100.00	94.06	100.00	94.56
$N_{cluster} \geq 1$	73.89	67.68	54.93	51.19	45.63	42.92	46.63	44.09
muon veto	92.15	62.37	93.79	48.01	93.24	40.02	92.26	40.68
jet veto	87.21	54.39	87.30	41.91	87.40	34.97	88.33	35.93
Time cut	100.00	54.39	99.79	41.82	99.74	34.88	99.40	35.72
ME1/1 veto	83.05	45.17	88.95	37.20	89.42	31.19	86.90	31.04
ME1/2 veto	67.47	30.48	73.11	27.20	74.80	23.33	65.78	20.42
RE1/2 veto	97.07	29.59	98.06	26.67	98.45	22.97	97.39	19.88
MB1 veto	93.20	27.57	95.08	25.36	93.89	21.56	95.35	18.96
RB1 veto	96.43	26.59	97.06	24.61	97.10	20.94	97.20	18.43
η cut	84.58	22.49	88.87	21.87	87.15	18.25	84.87	15.64
time spread cut	99.23	22.31	98.98	21.65	99.25	18.11	97.79	15.29
cut-based ID	88.96	19.85	90.32	19.55	87.58	15.86	97.74	14.95
$\Delta\phi(\text{cluster, MET})$	99.22	19.69	79.01	15.45	62.18	9.86	58.27	8.71
$N_{rechits}$ cut	90.06	17.74	80.43	12.42	77.47	7.64	80.89	7.05

Table 45: Signal Efficiency(%) of each cut for LLP mass 15 GeV and decaying to 4 d quarks. (Cumulative Efficiency for all cuts applied after Trigger and MET cut are calculated with respect to events in acceptance and pass the MET and trigger cut and cut efficiency is calculated with respect to the previous cut. Acceptance is defined as when at least one LLP decays inside CSC.)

Selection	$c\tau = 0.1m$		$c\tau = 1m$		$c\tau = 10m$		$c\tau = 100m$	
	cut eff	cumulative eff	cut eff	cumulative eff	cut eff	cumulative eff	cut eff	cumulative eff
Acceptance	2.690	2.690	27.539	27.539	9.006	9.006	1.080	1.080
Trigger and MET cut	2.354	0.063	0.830	0.229	0.926	0.083	0.951	0.010
MET filters	97.06	97.06	98.28	98.28	99.20	99.20	99.81	99.81
$N_{lepton} = 0$	99.65	96.72	99.56	97.84	99.77	98.98	99.63	99.44
$N_{jet} \geq 1$	96.22	93.07	95.34	93.29	94.58	93.62	95.31	94.77
$N_{CSC+DT \text{ rings}} \leq 10$	100.00	93.07	100.00	93.29	100.00	93.62	100.00	94.77
$N_{cluster} \geq 1$	80.34	74.77	63.51	59.25	51.87	48.56	49.11	46.54
muon veto	93.66	70.03	93.83	55.60	94.52	45.90	92.59	43.09
jet veto	85.96	60.19	87.13	48.44	87.74	40.27	90.96	39.19
Time cut	99.64	59.97	99.89	48.39	97.68	39.34	94.46	37.02
ME1/1 veto	76.03	45.60	87.43	42.30	88.14	34.67	91.10	33.73
ME1/2 veto	64.74	29.52	71.03	30.05	72.04	24.98	77.16	26.02
RE1/2 veto	97.54	28.79	97.70	29.36	98.62	24.63	98.22	25.56
MB1 veto	93.22	26.84	94.99	27.89	95.78	23.59	95.26	24.35
RB1 veto	97.88	26.27	96.51	26.91	98.03	23.13	98.56	24.00
η cut	77.66	20.40	89.03	23.96	89.77	20.76	91.15	21.87
time spread cut	99.11	20.22	99.17	23.76	98.90	20.53	98.05	21.45
cut-based ID	84.01	16.99	91.18	21.67	92.13	18.92	89.21	19.13
$\Delta\phi(\text{cluster}, \text{MET})$	100.00	16.99	87.87	19.04	70.36	13.31	60.06	11.49
$N_{rechits}$ cut	92.29	15.68	83.54	15.90	78.28	10.42	77.10	8.86

Table 46: Signal Efficiency(%) of each cut for LLP mass 40 GeV and decaying to 4 d quarks. (Cumulative Efficiency for all cuts applied after Trigger and MET cut are calculated with respect to events in acceptance and pass the MET and trigger cut and cut efficiency is calculated with respect to the previous cut. Acceptance is defined as when at least one LLP decays inside CSC.)

Selection	$c\tau = 0.1m$		$c\tau = 1m$		$c\tau = 10m$		$c\tau = 100m$	
	cut eff	cumulative eff	cut eff	cumulative eff	cut eff	cumulative eff	cut eff	cumulative eff
Acceptance	0.088	0.088	17.081	17.081	20.383	20.383	3.321	3.321
Trigger and MET cut	7.846	0.007	0.967	0.165	0.706	0.144	0.660	0.022
MET filters	99.02	99.02	96.68	96.68	99.04	99.04	99.72	99.72
$N_{lepton} = 0$	99.82	98.84	99.64	96.34	99.81	98.85	99.96	99.68
$N_{jet} \geq 1$	97.48	96.36	95.61	92.11	94.50	93.42	95.46	95.15
$N_{CSC+DT \text{ rings}} \leq 10$	100.00	96.36	100.00	92.11	100.00	93.42	100.00	95.15
$N_{cluster} \geq 1$	91.21	87.89	73.72	67.90	62.70	58.57	59.88	56.97
muon veto	92.83	81.59	94.80	64.37	94.76	55.51	93.88	53.49
jet veto	60.67	49.50	83.14	53.52	88.46	49.10	89.48	47.86
Time cut	99.58	49.29	99.84	53.44	96.08	47.18	91.73	43.90
ME1/1 veto	52.85	26.05	81.56	43.58	86.48	40.80	89.07	39.10
ME1/2 veto	70.63	18.40	67.05	29.23	71.68	29.24	70.91	27.73
RE1/2 veto	97.51	17.94	98.12	28.68	97.71	28.57	96.78	26.83
MB1 veto	95.69	17.17	94.52	27.11	96.24	27.50	96.62	25.93
RB1 veto	100.00	17.17	96.05	26.04	97.25	26.74	98.28	25.48
η cut	47.67	8.18	83.52	21.75	90.53	24.21	89.14	22.71
time spread cut	100.00	8.18	99.13	21.56	99.17	24.01	99.17	22.53
cut-based ID	58.08	4.75	87.45	18.85	92.18	22.13	92.84	20.91
$\Delta\phi(\text{cluster}, \text{MET})$	100.00	4.75	99.39	18.73	95.52	21.14	96.20	20.12
$N_{rechits}$ cut	99.84	4.74	87.76	16.44	80.62	17.04	78.92	15.88

Table 47: Signal Efficiency(%) of each cut for LLP mass 55 GeV and decaying to 4 d quarks. $c\tau = 0.1$ m is not shown for 55 GeV, because the acceptance is on the order of 10^{-5} , so there are no events left after all selections are applied. (Cumulative Efficiency for all cuts applied after Trigger and MET cut are calculated with respect to events in acceptance and pass the MET and trigger cut and cut efficiency is calculated with respect to the previous cut. Acceptance is defined as when at least one LLP decays inside CSC.)

Selection	$c\tau = 1m$		$c\tau = 10m$		$c\tau = 100m$	
	cut eff	cumulative eff	cut eff	cumulative eff	cut eff	cumulative eff
Acceptance	8.350	8.350	23.899	23.899	5.275	5.275
Trigger and MET cut	1.332	0.111	0.641	0.153	0.440	0.023
MET filters	96.19	96.19	99.37	99.37	99.54	99.54
$N_{lepton} = 0$	99.58	95.78	99.65	99.02	99.67	99.21
$N_{jet} \geq 1$	96.04	91.98	94.34	93.41	94.24	93.50
$N_{CSC+DT \text{ rings}} \leq 10$	100.00	91.98	100.00	93.41	100.00	93.50
$N_{cluster} \geq 1$	77.43	71.23	67.86	63.39	63.28	59.17
muon veto	93.39	66.52	93.98	59.58	93.04	55.05
jet veto	69.65	46.33	89.42	53.27	87.90	48.39
Time cut	99.84	46.25	99.70	53.12	98.77	47.80
ME1/1 veto	70.40	32.56	87.02	46.22	89.71	42.88
ME1/2 veto	62.87	20.47	70.38	32.53	73.52	31.53
RE1/2 veto	97.42	19.94	98.36	32.00	97.18	30.64
MB1 veto	93.83	18.71	95.30	30.49	97.11	29.75
RB1 veto	97.50	18.24	96.47	29.42	97.56	29.02
η cut	69.46	12.67	90.54	26.63	92.93	26.97
time spread cut	99.19	12.57	98.92	26.35	99.06	26.72
cut-based ID	80.15	10.07	92.72	24.43	91.50	24.45
$\Delta\phi(\text{cluster, MET})$	100.00	10.07	99.97	24.42	100.00	24.45
$N_{rechits}$ cut	89.43	9.01	81.34	19.86	84.69	20.70

Table 48: Signal Efficiency(%) of each cut for LLP mass 7 GeV and decaying to 4τ leptons. (Cumulative Efficiency for all cuts applied after Trigger and MET cut are calculated with respect to events in acceptance and pass the MET and trigger cut and cut efficiency is calculated with respect to the previous cut. Acceptance is defined as when at least one LLP decays inside CSC.)

Selection	$c\tau = 0.1m$		$c\tau = 1m$		$c\tau = 10m$		$c\tau = 100m$	
	cut eff	cumulative eff	cut eff	cumulative eff	cut eff	cumulative eff	cut eff	cumulative eff
Acceptance	10.659	10.659	23.360	23.360	4.520	4.520	0.498	0.498
Trigger and MET cut	1.615	0.172	0.882	0.206	0.959	0.043	0.896	0.004
MET filters	95.55	95.55	98.84	98.84	99.28	99.28	99.35	99.35
$N_{lepton} = 0$	98.13	93.77	99.46	98.31	99.34	98.63	99.71	99.06
$N_{jet} \geq 1$	95.68	89.72	94.78	93.18	94.13	92.84	95.78	94.89
$N_{CSC+DT\ rings} \leq 10$	100.00	89.72	100.00	93.18	100.00	92.84	100.00	94.89
$N_{cluster} \geq 1$	55.41	49.71	38.17	35.57	31.74	29.46	33.22	31.53
muon veto	89.64	44.56	92.27	32.82	93.41	27.52	98.97	31.20
jet veto	86.28	38.44	86.90	28.52	88.03	24.23	87.81	27.40
Time cut	99.76	38.35	99.45	28.36	99.70	24.16	98.74	27.05
ME1/1 veto	84.71	32.49	88.85	25.20	87.94	21.24	94.16	25.47
ME1/2 veto	71.03	23.08	76.71	19.33	77.27	16.42	75.47	19.22
RE1/2 veto	97.34	22.46	97.93	18.93	98.47	16.16	98.58	18.95
MB1 veto	93.93	21.10	95.05	17.99	95.85	15.49	90.66	17.18
RB1 veto	97.05	20.48	97.28	17.50	97.89	15.17	97.43	16.74
η cut	82.66	16.93	87.87	15.38	87.60	13.29	81.34	13.61
time spread cut	98.86	16.73	99.04	15.23	100.00	13.29	100.00	13.61
cut-based ID	85.33	14.28	89.06	13.57	84.97	11.29	72.01	9.80
$\Delta\phi(\text{cluster}, \text{MET})$	99.09	14.15	81.68	11.08	68.01	7.68	63.09	6.19
$N_{rechits}$ cut	78.40	11.09	67.36	7.46	63.01	4.84	73.08	4.52

Table 49: Signal Efficiency(%) of each cut for LLP mass 15 GeV and decaying to 4τ leptons. (Cumulative Efficiency for all cuts applied after Trigger and MET cut are calculated with respect to events in acceptance and pass the MET and trigger cut and cut efficiency is calculated with respect to the previous cut. Acceptance is defined as when at least one LLP decays inside CSC.)

Selection	$c\tau = 0.1m$		$c\tau = 1m$		$c\tau = 10m$		$c\tau = 100m$	
	cut eff	cumulative eff	cut eff	cumulative eff	cut eff	cumulative eff	cut eff	cumulative eff
Acceptance	2.688	2.688	27.518	27.518	8.997	8.997	1.084	1.084
Trigger and MET cut	3.235	0.087	0.887	0.244	0.924	0.083	0.937	0.010
MET filters	95.67	95.67	98.19	98.19	99.27	99.27	99.52	99.52
$N_{lepton} = 0$	97.58	93.35	99.22	97.43	99.59	98.86	99.90	99.41
$N_{jet} \geq 1$	95.61	89.26	95.25	92.80	94.42	93.35	93.88	93.33
$N_{CSC+DT\ rings} \leq 10$	100.00	89.26	100.00	92.80	100.00	93.35	100.00	93.33
$N_{cluster} \geq 1$	61.22	54.65	44.04	40.87	32.04	29.90	26.59	24.81
muon veto	90.20	49.29	92.50	37.80	92.96	27.80	94.03	23.33
jet veto	86.55	42.66	87.90	33.23	86.68	24.10	85.15	19.87
Time cut	99.75	42.55	99.61	33.10	98.56	23.75	97.67	19.40
ME1/1 veto	78.63	33.46	88.11	29.17	88.13	20.93	92.09	17.87
ME1/2 veto	68.54	22.94	74.50	21.73	77.94	16.31	80.02	14.30
RE1/2 veto	97.45	22.35	98.11	21.32	98.20	16.02	100.00	14.30
MB1 veto	94.55	21.13	94.50	20.14	95.07	15.23	95.23	13.62
RB1 veto	97.37	20.58	97.41	19.62	97.15	14.80	96.53	13.14
η cut	75.46	15.53	86.74	17.02	88.47	13.09	93.74	12.32
time spread cut	98.65	15.32	98.93	16.84	99.48	13.02	100.00	12.32
cut-based ID	79.63	12.20	87.87	14.79	89.47	11.65	89.53	11.03
$\Delta\phi(\text{cluster}, \text{MET})$	100.00	12.20	89.19	13.19	71.52	8.33	69.71	7.69
$N_{rechits}$ cut	80.52	9.82	70.00	9.24	68.80	5.73	51.20	3.94

Table 50: Signal Efficiency(%) of each cut for LLP mass 40 GeV and decaying to 4 τ leptons. (Cumulative Efficiency for all cuts applied after Trigger and MET cut are calculated with respect to events in acceptance and pass the MET and trigger cut and cut efficiency is calculated with respect to the previous cut. Acceptance is defined as when at least one LLP decays inside CSC.)

Selection	$c\tau = 0.1m$		$c\tau = 1m$		$c\tau = 10m$		$c\tau = 100m$	
	cut eff	cumulative eff	cut eff	cumulative eff	cut eff	cumulative eff	cut eff	cumulative eff
Acceptance	0.088	0.088	17.088	17.088	20.388	20.388	3.329	3.329
Trigger and MET cut	12.156	0.011	1.290	0.220	0.756	0.154	0.646	0.021
MET filters	93.89	93.89	96.41	96.41	99.32	99.32	99.73	99.73
$N_{lepton} = 0$	94.41	88.65	98.94	95.39	99.55	98.87	99.72	99.45
$N_{jet} \geq 1$	97.32	86.27	95.24	90.85	94.25	93.19	95.40	94.88
$N_{CSC+DT\ rings} \leq 10$	100.00	86.27	100.00	90.85	100.00	93.19	100.00	94.88
$N_{cluster} \geq 1$	61.63	53.17	52.32	47.53	39.32	36.64	34.22	32.47
muon veto	89.19	47.42	93.47	44.43	94.81	34.74	94.24	30.60
jet veto	60.15	28.52	84.55	37.57	89.15	30.97	89.94	27.52
Time cut	98.37	28.06	99.62	37.42	97.52	30.20	95.82	26.37
ME1/1 veto	58.86	16.52	86.20	32.26	89.62	27.07	87.49	23.07
ME1/2 veto	67.41	11.13	69.97	22.57	75.90	20.54	74.46	17.18
RE1/2 veto	100.00	11.13	97.62	22.03	97.66	20.06	96.12	16.51
MB1 veto	98.78	11.00	94.05	20.72	95.10	19.08	95.78	15.82
RB1 veto	98.40	10.82	96.83	20.07	97.70	18.64	96.75	15.30
η cut	51.91	5.62	82.27	16.51	89.55	16.69	91.27	13.97
time spread cut	93.45	5.25	98.69	16.29	98.54	16.45	97.90	13.67
cut-based ID	59.27	3.11	86.42	14.08	87.95	14.47	87.68	11.99
$\Delta\phi(\text{cluster, MET})$	100.00	3.11	99.60	14.02	96.61	13.98	97.00	11.63
$N_{rechits}$ cut	79.77	2.48	74.76	10.48	66.46	9.29	67.39	7.84

Table 51: Signal Efficiency(%) of each cut for LLP mass 55 GeV and decaying to 4τ leptons. (Cumulative Efficiency for all cuts applied after Trigger and MET cut are calculated with respect to events in acceptance and pass the MET and trigger cut and cut efficiency is calculated with respect to the previous cut. Acceptance is defined as when at least one LLP decays inside CSC.)

Selection	$c\tau = 1m$		$c\tau = 10m$		$c\tau = 100m$	
	cut eff	cumulative eff	cut eff	cumulative eff	cut eff	cumulative eff
Acceptance	8.374	8.374	23.915	23.915	5.271	5.271
Trigger and MET cut	2.165	0.181	0.693	0.166	0.441	0.023
MET filters	95.02	95.02	98.74	98.74	99.29	99.29
$N_{lepton} = 0$	98.37	93.48	99.70	98.45	99.90	99.19
$N_{jet} \geq 1$	95.72	89.48	94.38	92.92	94.85	94.08
$N_{CSC+DT \text{ rings}} \leq 10$	100.00	89.48	100.00	92.92	100.00	94.08
$N_{cluster} \geq 1$	54.68	48.93	43.74	40.64	40.61	38.20
muon veto	90.71	44.39	93.69	38.08	94.51	36.10
jet veto	67.73	30.06	87.63	33.37	92.47	33.38
Time cut	99.65	29.95	99.59	33.23	100.00	33.38
ME1/1 veto	77.27	23.15	89.46	29.73	87.48	29.20
ME1/2 veto	65.75	15.22	73.36	21.81	75.98	22.19
RE1/2 veto	96.62	14.70	98.04	21.38	96.35	21.38
MB1 veto	90.87	13.36	95.16	20.35	97.90	20.93
RB1 veto	97.55	13.03	96.83	19.70	97.50	20.40
η cut	74.90	9.76	89.12	17.56	88.94	18.15
time spread cut	98.57	9.62	98.93	17.37	99.66	18.08
cut-based ID	79.83	7.68	89.96	15.63	92.76	16.77
$\Delta\phi(\text{cluster, MET})$	100.00	7.68	99.87	15.61	99.67	16.72
$N_{rechits}$ cut	78.21	6.01	69.00	10.77	63.77	10.66

1344 E Cluster-Level BDT

1345 We present an alternative BDT selection for the cluster-level identification. As discussed for
 1346 the cut-based cluster identification selection, the majority of the remaining background are due
 1347 to pileup. Since the pileup contribution from in-time and out-of-time are expected to have the
 1348 same shape, the early out-of-time (time < -12.5 ns) clusters in data is used as background for
 1349 training, while the clusters that are matched to gen-level LLP that decay in the CSC system
 1350 from signal MC samples are used as the signal.

1351 The same set of 3 cluster-level variables, the cluster η position, average station number, and
 1352 $N_{stations}$ are used for the BDT training. The distributions of signal and background of the BDT
 training variables are shown in Fig. 69. For this BDT, 80% of the events are used for training,

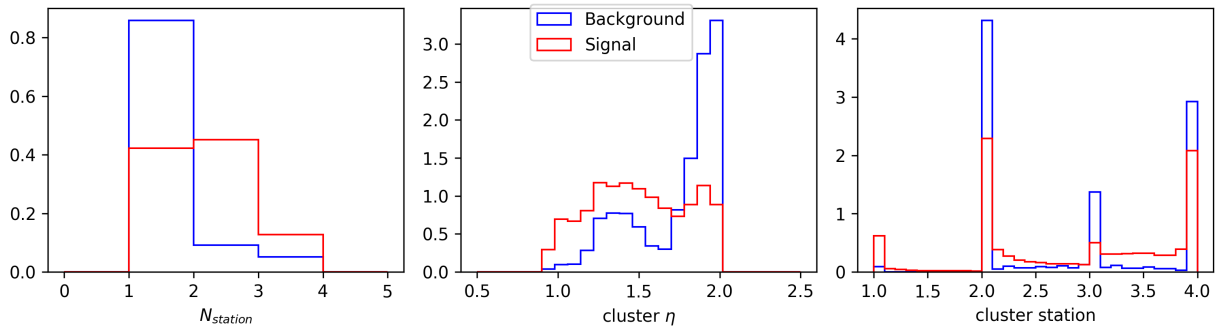


Figure 69: The distribution of the sum of all signal samples and background are shown.

1353 while 20% used for testing. The BDT response distributions for signal and background are
 1354 shown in Fig. 70. The ROC curve is shown in Fig. 71, where the ROC curve for both the sum
 1355 of all signal samples and the individual signal samples are shown. It can be seen from Fig. 71,
 1356 that the ROC curve for different signal models are similar. The signal with $m_x = 55$ GeV and
 1357 $c\tau = 0.1$ m is not shown, because the acceptance for this particular point is so small that zero
 1358 events pass the selections for the signal region.

1360 At the same signal efficiency of 82% as the cut-based ID, the background rejection from the
 1361 BDT is 4, corresponding to a 30% improvement in background rejection with respect to the
 1362 cut-based ID.

1363 E.1 BDT Validation

1364 This section details the study performed to validate the use of the BDT cluster ID by training
 1365 a separate BDT with to discriminate between clusters produced by muon bremsstrahlung and
 1366 clusters produced by background (pileup), using data for both. This separate BDT is then
 1367 evaluated on clusters from muon bremsstrahlung from simulation to confirm that the response
 1368 of the BDT is comparable for data and for MC.

1370 The event and cluster-level selections used for clusters produced from muon bremsstrahlung
 1371 for both data and MC are the same as the selection criteria described in Section 7. For clus-
 1372 ters produced from background(pileup), no event-level requirements are implemented and the
 1373 clusters are selected with the same set of selections in Table 26, except the time cut is changed
 1374 to time < -12.5 ns. This sample of early OOT clusters, is the same as the selections used for the
 1375 background selections used for the optimization in the cut-based cluster ID and the BDT.

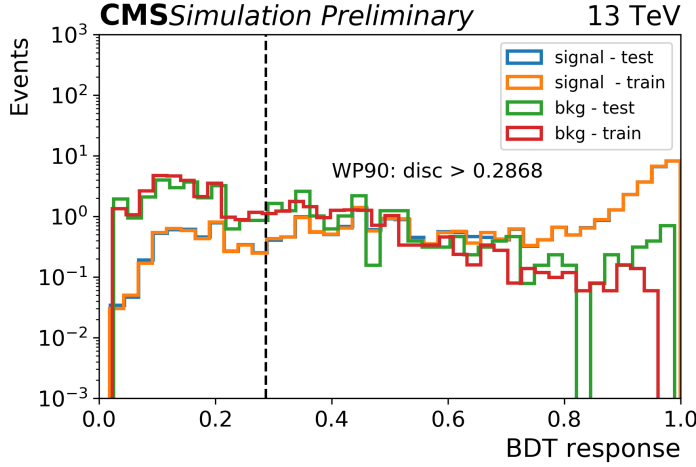


Figure 70: Distribution of BDT response for signal and background.

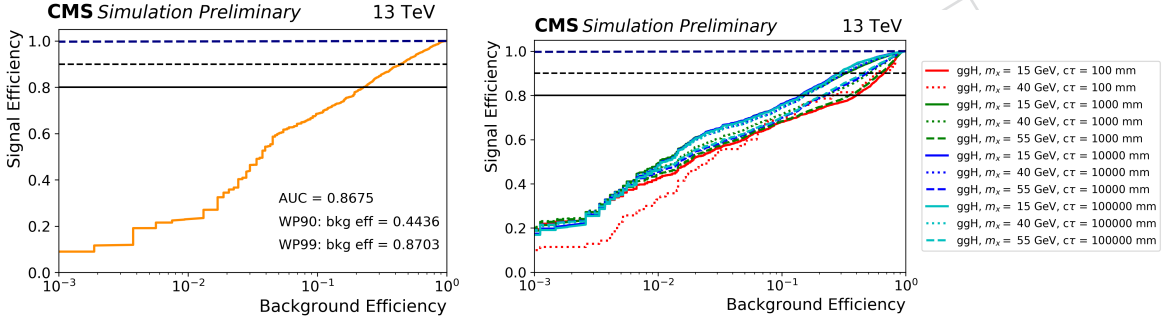


Figure 71: The ROC curve for the sum of all signal samples against background (Left) and the ROC curve for each signal sample against background(Right).

1376 The BDT is trained with the same set of 3 cluster-level variables used in the cut-based ID,
 1377 described in 5.1.1. The 3 variables are: the cluster η position, average station number, and
 1378 N_{stations} . The distributions of muon bremsstrahlung induced clusters in data (signal for BDT)
 1379 and OOT pileup (background for BDT) of the 3 BDT training variables are shown in Fig. 72.
 1380 The BDT is trained with 50 % of the events and evaluated with the other 50 %. To assure
 1381 that there is no overlap in the datasets for training and for testing, all events with even event
 1382 numbers are used for training and all events with odd event numbers are used for testing. The
 1383 BDT response distributions for signal and background are shown in Fig. 75. The ROC curve is
 1384 shown in Fig. 73.

1385 We choose a background efficiency of 20% and evaluate the BDT efficiency for muon brem-
 1386 strahlung clusters for both data and MC. We measured an efficiency of 66.2% for MC and an
 1387 efficiency of 67.3% for data. With this we confirmed that the simulation models the muon
 1388 bremsstrahlung and clustering well and can be distinguished from OOT pileup clusters.

1389 A 90% working point is chosen for the BDT, and we measure the BDT efficiencies in the muon
 1390 brem control region for the chosen working point. The efficiencies for data and simulations
 1391 in different mass bins are summarized in Table 52. Similarly, a few percent differences are
 1392 observed in each mass bin.

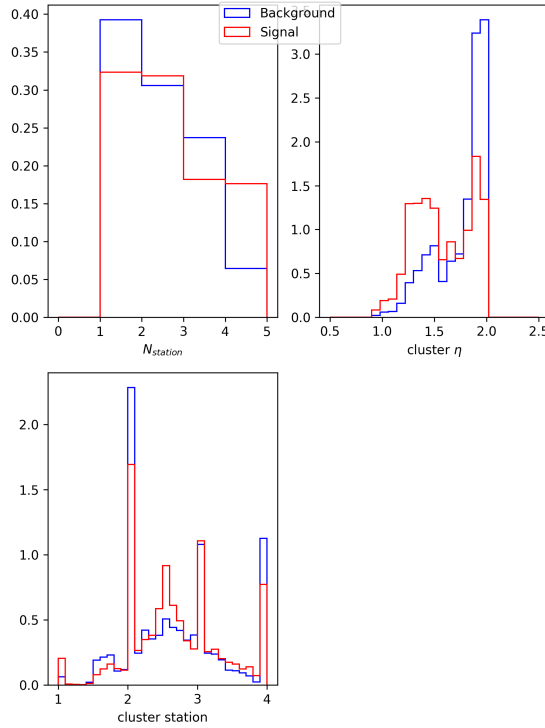


Figure 72: The distribution of the input features for signal and background are shown.

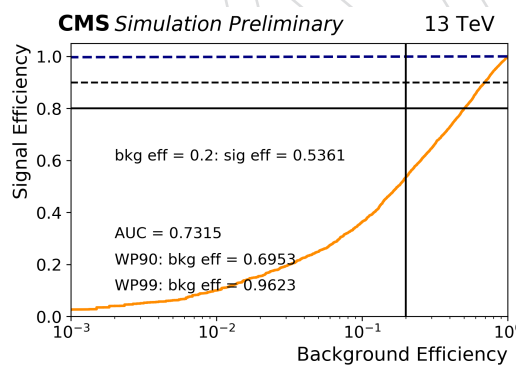


Figure 73: The ROC curve for the signal data sample against out of time background is shown.

Table 52: BDT efficiency in each mass bin.

Mass bin	Data	MC	% difference
(50, 120)	0.850	0.831	2.34%
(120, 200)	0.840	0.817	2.88%
(200, 400)	0.843	0.821	2.75%
(400, 800)	0.850	0.837	1.58%
(50, 800)	0.847	0.825	2.67%

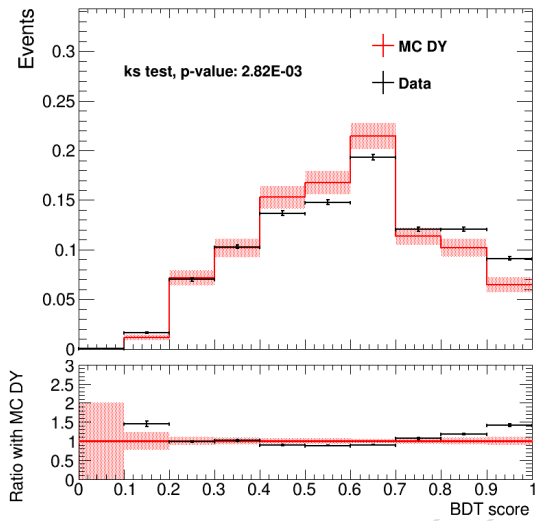


Figure 74: The BDT output for signal in data and MC is shown.

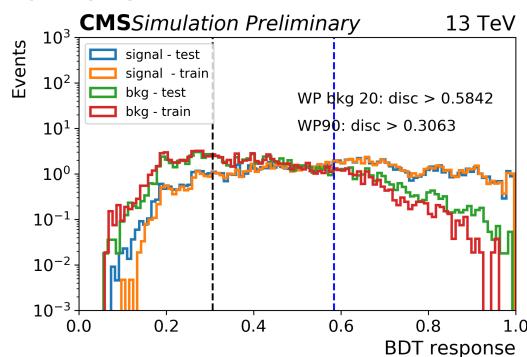


Figure 75: Distribution of BDT response for signal and background.

1393 F Supplementary Material

1394 This section documents the signal efficiency parameterization that we publish as supplementary material for reinterpretation. The result of this study is published in the HEPData record
 1395 of this analysis [46].

1396 We release parameterizations for both cluster efficiency that includes all cluster-level selections
 1397 (excluding jet veto, time, and $\Delta\phi$ cut) and the cut-based ID efficiency per LLP. We demonstrate
 1398 that a simple parameterization in gen-level hadronic energy, EM Energy, and LLP decay position
 1399 is sufficient to reproduce full-sim signal efficiencies for LLPs to within 35% and 20% in the
 1400 geometric acceptance region A and B, as defined below, respectively. The study is validated
 1401 with LLPs with mass between 7-55 GeV, lifetime between 0.1 m - 100 m, and decay mode $d\bar{d}$
 1402 and $\tau^-\tau^+$.

1403 The electromagnetic and hadronic energy of the LLP is calculated by first matching status 1
 1404 gen-level particles to the LLP if the particle production vertex is within 0.1m from the LLP
 1405 decay vertex. If the particle is matched to both LLPs, then its assigned to the closer LLP. The
 1406 energy of the matched gen-level particle is assigned as EM energy if the particle is a neutral
 1407 pion, electron, or photon. The energy of the matched particle is ignored if it's a neutrino or
 1408 muon, as they don't produce showers in the muon system. All other particles are assigned as
 1409 hadronic energy.

1410 The parametrization efficiency is derived from the 4τ sample listed in Table 2, since τ decays
 1411 both leptonically and hadronically.

1412 We categorize the LLP decay location into 2 regions, as shown in Fig. 76. These 2 regions have
 1413 qualitatively different behavior. Within each region, they have quantitatively similar behavior.
 1414 Region A is defined as $391 \text{ cm} < R < 695.5 \text{ cm}$ and $400 \text{ cm} < |Z| < 671 \text{ cm}$. Region B is defined
 1415 as $671 \text{ cm} < |Z| < 1100 \text{ cm}$ and $R < 695.5 \text{ cm}$ and $|\eta| < 2$.

1416 The fraction of LLPs that decay in each region are dependent on the LLP mass and $c\tau$. However,
 1417 the signal efficiency in A is much lower than that in B, so more than 90% of clusters passing all
 1418 selections are from LLPs that decay in region B.

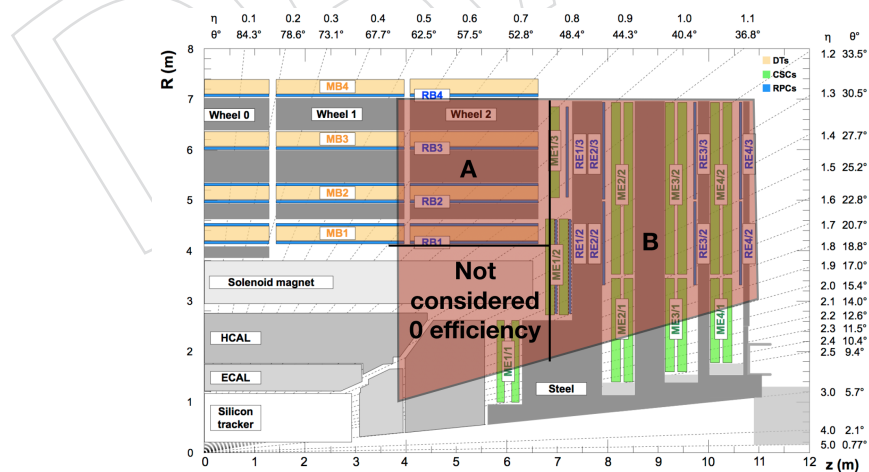


Figure 76: The geometric acceptance region considered for LLP decay in the endcap is shaded in red. Region A and B are shown. The rest of the acceptance region are not considered, since the signal efficiency is almost zero (<0.5%), due to shielding and the vetos.

1420 F.1 Cluster Efficiency

1421 We estimate the cluster efficiency in the 2 decay regions separately in bins of hadronic and EM
 1422 energy, as shown in Fig. 77. The cluster efficiency is defined by the cluster reconstruction ef-
 1423 ficiency multiplied by the signal efficiency of the cluster-level selections, including the muon
 1424 veto, segment/rechit vetos, time spread cut, and $N_{rechits} > 130$. The cluster efficiency parame-
 1425 terization does not include the jet veto, time, and $\Delta\phi$ cut, since these cuts are model dependent.
 1426 The efficiency is calculated per LLP.

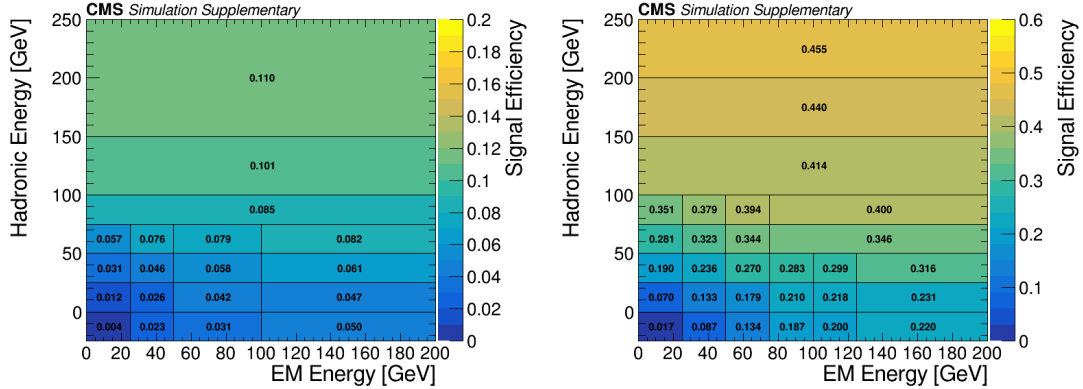


Figure 77: The cluster efficiency in bins of hadronic and EM energy in region A (Left) and B (Right). The cluster efficiency is evaluated using the sum of all mass and $c\tau$ models available from the 4τ sample. The first hadronic energy bins correspond to LLPs that decayed leptonically with 0 hadronic energy. The statistical uncertainty for each bin is documented in Additional Figure 7 of the HEPData record of this analysis [46].

1427 We have checked that the parametrization is independent of LLP mass (7-55 GeV) and lifetime
 1428 (0.1m-100m) using the signal sample where the LLP decays to 2τ . Since the EM fraction for the
 1429 same decay mode remains the same, to better visualize the trend, the cluster efficiency with
 1430 respect to the LLP energy is shown for different LLP masses and lifetimes, in Fig. 78 and Fig. 79
 1431 respectively. No dependence on LLP mass(7-55 GeV) and lifetime(0.1m-100m) are observed.

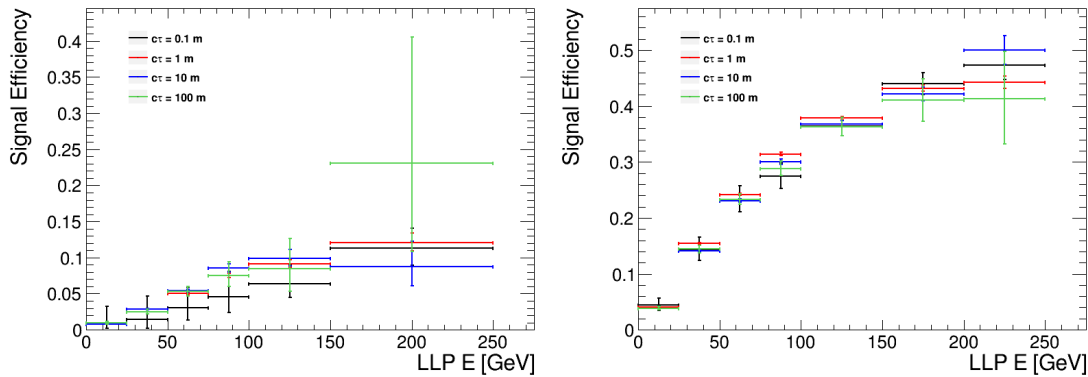


Figure 78: The cluster efficiency with respect to LLP energy in region A (Left) and B (Right) for a 15 GeV LLP and different LLP lifetimes.

1432 We also check for independence of the LLP decay mode by checking the cluster efficiency in
 1433 bins of hadronic and EM energy for the 4d sample, as shown in Fig. 80. The parametrization
 1434 shown in Fig. 80 are in good agreement with the parametrization derived from the 4τ sample,

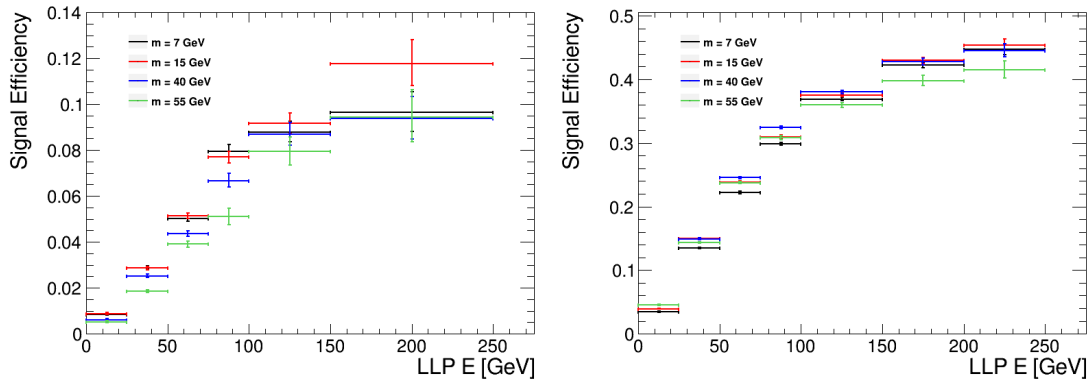


Figure 79: The cluster efficiency with respect to LLP energy in region A (Left) and B (Right) for different LLP masses. The different LLP mass samples consists of the sum of all available lifetimes ranging from 0.1 to 100 m.

1435 shown in Fig. 77, except in the first hadronic energy bin, where the LLP decays fully leptonically.

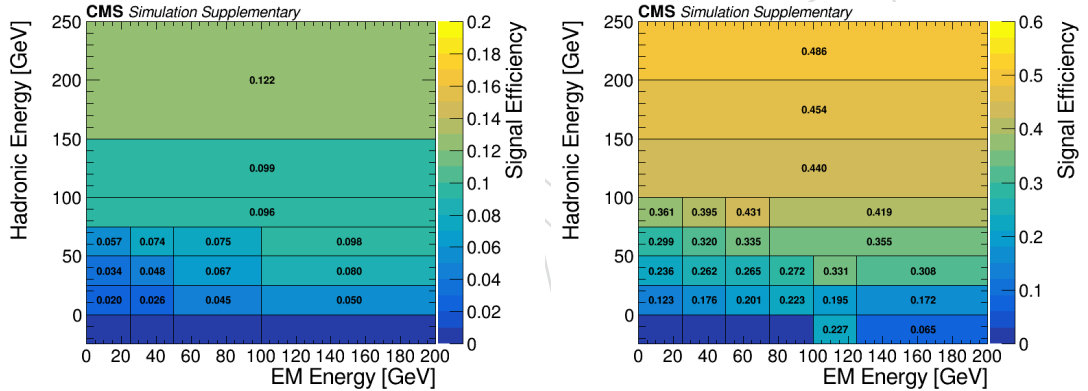


Figure 80: The cluster efficiency estimated from LLP decaying to dd in bins of hadronic and EM energy in region A (Left) and B (Right). The first hadronic energy bins correspond to LLPs that decayed leptonically with 0 hadronic energy. The sample includes the sum of all available mass (7- 55 GeV) and ctau (0.1-100m) points.

1436

1437 Furthermore, we validated the signal yield prediction against the full-sim prediction for models
 1438 with varying LLP mass between 7-55 GeV, lifetime between 0.1 m - 100 m, and decay mode $\bar{d}d$
 1439 and $\tau^-\tau^+$, using the parameterization shown in Fig. 77. The ratio between the parameterized
 1440 prediction and the full simulation prediction is shown in Table 53 and Table 54 for region A and
 1441 B, respectively. We observed the parametrized signal yield for all models considered agrees
 1442 with the full-sim prediction to within 35% and 20% for region A and B respectively.

1443 F.2 Cut-Based ID Efficiency

1444 We parametrize the cut-based ID efficiency with respect to clusters that pass the cluster-level
 1445 selections (nominator in the cluster efficiency parametrization). As described in Section 5.1.1,
 1446 the cluster ID requirement applies different η cuts depending on the $N_{station}$ and average station
 1447 number of the cluster.

1448 Since the entire region A has lower η than the η cuts, all clusters in region A pass the cut-based

Table 53: Ratio between parameterized prediction and full-simulation prediction for LLP decaying to $\tau^-\tau^+$ and $d\bar{d}$. The empty points are due to lack of statistics in the signal region.

$\tau^-\tau^+$				
LLP mass $c\tau$	0.1 m	1 m	10 m	100 m
7 GeV	1.15 ± 0.08	0.90 ± 0.02	0.93 ± 0.05	0.89 ± 0.14
15 GeV	1.09 ± 0.22	0.92 ± 0.02	0.90 ± 0.03	0.96 ± 0.11
40 GeV	1.44 ± 1.17	1.14 ± 0.06	1.04 ± 0.03	0.96 ± 0.07
55 GeV	/	1.33 ± 0.13	1.27 ± 0.04	1.27 ± 0.08
$d\bar{d}$				
LLP mass $c\tau$	0.1 m	1 m	10 m	100 m
7 GeV	1.14 ± 0.19	0.95 ± 0.05	0.82 ± 0.10	0.97 ± 0.35
15 GeV	/	0.96 ± 0.07	0.81 ± 0.08	0.83 ± 0.24
40 GeV	/	1.07 ± 0.21	1.05 ± 0.12	0.87 ± 0.22
55 GeV	/	/	0.97 ± 0.14	1.16 ± 0.31

Table 54: Ratio between parameterized prediction and full-simulation prediction for LLP decaying to $\tau^-\tau^+$ and $d\bar{d}$. The empty points for 40 and 55 GeV are due to lack of statistics in the signal region.

$\tau^-\tau^+$				
LLP mass $c\tau$	0.1 m	1 m	10 m	100 m
7 GeV	0.97 ± 0.01	1.05 ± 0.01	1.09 ± 0.02	1.10 ± 0.06
15 GeV	0.97 ± 0.04	0.97 ± 0.01	1.04 ± 0.01	1.06 ± 0.04
40 GeV	1.23 ± 0.39	0.93 ± 0.01	0.97 ± 0.01	1.01 ± 0.02
55 GeV	0.94 ± 0.71	0.99 ± 0.02	0.99 ± 0.01	1.05 ± 0.02
$d\bar{d}$				
LLP mass $c\tau$	0.1 m	1 m	10 m	100 m
7 GeV	0.95 ± 0.04	1.01 ± 0.02	1.01 ± 0.04	1.05 ± 0.12
15 GeV	0.97 ± 0.15	0.94 ± 0.02	0.97 ± 0.03	1.01 ± 0.10
40 GeV	/	0.91 ± 0.04	0.87 ± 0.03	0.82 ± 0.06
55 GeV	/	0.95 ± 0.09	0.82 ± 0.03	0.81 ± 0.06

- 1449 ID. Therefore, we focus on the parameterization of cut-based ID efficiency in region B only.
 1450 To parametrize the efficiency of the cut-based ID, we need two steps. We need a parametriza-
 1451 tion of the efficiency of $N_{station} > 1$ requirement and a transfer function that takes gen-level
 1452 LLP decay position to RECO-level cluster average station (only for clusters with $N_{station} = 1$)
 1453 The efficiency of $N_{station} > 1$ can be well parameterized using just the gen-level hadronic energy
 1454 in the region B, as shown in Fig. 81. The efficiency is independent of the LLP EM energy. We
 1455 have checked that the parameterization is independent of LLP mass (7-55 GeV), lifetime (0.1 m
 1456 - 100 m), and decay mode($d\bar{d}$ and $\tau^-\tau^+$) within region B, as shown in Fig. 82.

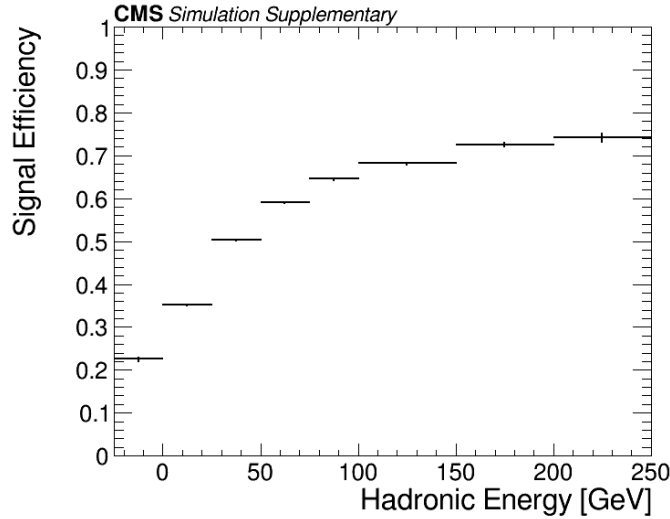


Figure 81: The efficiency of $N_{station} > 1$ requirement with respect to hadronic energy in region B. The first hadronic energy bin corresponds to LLPs that decayed leptonically with 0 hadronic energy.

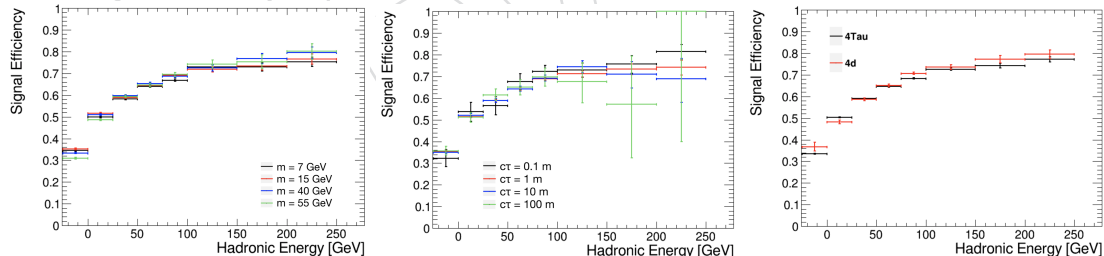


Figure 82: The efficiency of $N_{station} > 1$ requirement in region B, comparing different LLP masses (Left), lifetimes (Center), and decay modes (Right). The different mass samples in left plot consists of the sum of all available $c\tau$ points (0.1-100 m). The different $c\tau$ samples in the center plot assumes an LLP mass of 15 GeV. The different decay mode samples in the right plot consists of all available mass (7-55 GeV) and $c\tau$ (0.1-100 m) points available. The first hadronic energy bin corresponds to LLPs that decayed leptonically with 0 hadronic energy. No dependence on LLP mass observed.

1457 The average station transfer function is implemented with a simple mapping between the LLP
 1458 decay position and the average station number. We define the cluster station to be the station
 1459 subsequent to the LLP decay position. For example, if the LLP decays between station 2 and
 1460 3, the average station will be station 3. We will provide the average station function and an
 1461 implementation of cut-based ID as an Additional Resources in HEPData. The code snippet of
 1462 the two functions is shown below.

```

1463 import numpy as np
1464 import math
1465 # given array of LLP decay position Z, R in cm,
1466 # output the avgStation prediction
1467
1468 def AvgStation(Z, R): # distances in cm
1469     station = np.copy(Z)
1470     station[np.abs(Z)<632] = 1
1471     station[np.logical_and(np.abs(Z)<724, np.abs(R)>275)] = 1
1472     station[np.logical_and(station>1, np.abs(Z)<850)] = 2
1473     station[np.logical_and(np.abs(Z)>=850,np.abs(Z)<970)] = 3
1474     station[np.abs(Z)>=970] = 4
1475     return station
1476
1477
1478 # given array of LLP decay position Z, R in cm,
1479 # output the LLP decay region, a string of 'a', 'b' or 'NA'
1480
1481 def region (Z, R, eta_list): # distances in cm
1482     region_list = []
1483     for z, r, eta in (Z, R, eta_list):
1484         if r > 391 and r < 695.5 and abs(z) > 400 and abs(z) < 671:
1485             region_list.append('a')
1486         elif abs(z) > 671 and abs(z) < 1100 and r < 695.5 and abs(eta) < 2:
1487             region_list.append('b')
1488         else:
1489             region_list.append('NA')
1490     return np.array(region_list)
1491
1492
1493 #input: list of LLP decay position in Z, R, LLP hadronic energy, LLP eta,
1494 #and a histogram of NStation>1 efficiency wrt to LLP hadronic energy
1495 #input type: z, r, hadE, eta are numpy arrays and eff_hist is TH1F
1496 #output: list of probability that the event passes cut-based ID
1497
1498 def cut_based_id(z, r, hadE, eta, eff_hist_a, eff_hist_b):
1499     avgStation = AvgStation(z, r)
1500     regions = region(z, r, eta)
1501     eff_hist = {'a': eff_hist_a, 'b': eff_hist_b}
1502     eta_cut = np.copy(avgStation)
1503     eta_cut[eta_cut==1] = 1.8 #implicitly 1.1
1504     eta_cut[eta_cut==2] = 1.6
1505     eta_cut[eta_cut==3] = 1.6

```

```

1506 eta_cut[eta_cut==4] = 1.8
1507 weight = []
1508 for j in range(len(hadE)):
1509     if regions[j] == 'NA':
1510         weight.append(0.0)
1511     else:
1512         x = eff_hist[regions[j]].GetXaxis().FindFixBin(hadE[j])
1513         weight.append(eff_hist.GetBinContent(x))
1514 weight = np.array(weight)
1515
1516 #apply eta<1.9 if NStation>1, else apply different eta cut as defined above
1517 weight = weight*(np.abs(eta)<1.9)+(1-weight)*(np.abs(eta)<eta_cut)
1518 weight[regions[j]=='NA'] = 0.0
1519 return weight
1520

```

1521 With the $N_{station} > 1$ efficiency parameterization and transfer function in place, we validated
 1522 the signal yield prediction against the full-sim prediction for models with varying LLP mass
 1523 between 7-55 GeV, lifetime between 0.1 m - 100 m, and decay mode $d\bar{d}$ and $\tau^-\tau^+$. The ratio
 1524 between the parameterized prediction and the full simulation prediction for decay region B is
 1525 shown in Table 55. We observed the parameterized signal yield matches the full-sim prediction
 1526 to within 10% for all models considered.

Table 55: Ratio between parameterized prediction and full-simulation prediction for LLP decaying to $\tau^-\tau^+$ and $d\bar{d}$. The empty points for 40 and 55 GeV are due to lack of statistics in the signal region.

LLP mass $c\tau$	$\tau^-\tau^+$			
	0.1 m	1 m	10 m	100 m
7 GeV	0.97 ± 0.02	0.97 ± 0.01	0.96 ± 0.02	0.95 ± 0.06
15 GeV	0.98 ± 0.05	0.96 ± 0.01	0.96 ± 0.01	0.95 ± 0.04
40 GeV	1.04 ± 0.44	0.95 ± 0.01	0.96 ± 0.01	0.97 ± 0.02
55 GeV	/	0.96 ± 0.02	0.98 ± 0.01	0.97 ± 0.02

LLP mass $c\tau$	$d\bar{d}$			
	0.1 m	1 m	10 m	100 m
7 GeV	0.99 ± 0.04	0.97 ± 0.02	0.98 ± 0.04	0.98 ± 0.12
15 GeV	0.98 ± 0.18	0.97 ± 0.02	0.97 ± 0.03	1.02 ± 0.10
40 GeV	/	0.98 ± 0.05	0.97 ± 0.03	0.99 ± 0.07
55 GeV	/	0.93 ± 0.10	0.98 ± 0.04	0.97 ± 0.07